Energy & Environmental Science

Accepted Manuscript

This article can be cited before page numbers have been issued, to do this please use: H. Li, Y. Zhou and A. Petrozza, *Energy Environ. Sci.*, 2026, DOI: 10.1039/D5EE07642K.

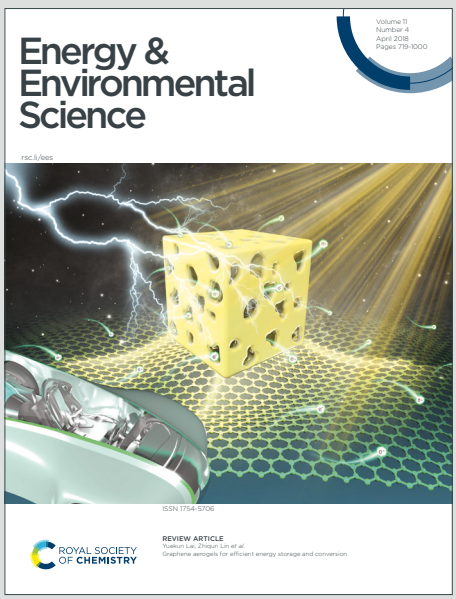

ROYAL SOCIETY OF CHEMISTRY

rsc.li/ees

View Article Online
DOI: 10.1039/D5EE07042K

The rapid progress of perovskite solar cells (PSCs) has pushed their efficiency to levels competitive with crystalline silicon, bringing commercial deployment within reach. The p-i-n inverted device structure has been pivotal in achieving record efficiencies in PSCs, both in single-junction and tandem architectures. The unprecedented achievement of PCE has been largely driven by innovations in charge transport materials (CTMs) and refined interface engineering. However, a critical stability bottleneck persists at the perovskite/CTM interface. Contacts with CTMs reshapes the defect landscape of perovskites, and the competition between charge extraction and trap formation at this interface ultimately dictates the devices longevity. Moreover, the chemically reactive perovskite surface is vulnerable to any intrinsic instability or degradation of the CTMs themselves, further accelerating interfacial breakdown. This review examines degradation mechanisms in inverted PSCs from an interfacial standpoint. It first outlines the intrinsic instabilities of pristine interfacial materials, then discusses interface-induced degradation in perovskites, including chemically driven degradation, defect and phase impurities, ion accumulation and migration, and mechanical delamination. Mitigation strategies, such as controllable surface construction, multi-layer interface, and stable transport layer design are discussed, alongside future research directions to enable durable inverted PSCs for real-world applications.

Stability of Inverted Perovskite Solar Cells: a focus on interface phenomena

Hui Li,[a*] Yang Zhou,[b] Annamaria Petrozza[a*]

[a]Center for Nano Science and Technology, Istituto Italiano di Tecnologia, via Rubattino 81, 20134 Milano, Italy

[b]Wuhan National Laboratory for Optoelectronics, Huazhong University of Science and Technology, Luoyu Road 1037, 430074 Wuhan, Hubei, China

*Corresponding authors. E-mail: hui.li@iit.it, annamaria.petrozza@iit.it

View Article Online
DOI: 10.1039/D5EE07642K

Abstract

The so-called inverted perovskite solar cells (PSCs), with a p-i-n device architecture have recently outperformed the traditional n-i-p counterparts in terms of record power conversion efficiency (PCE). The design of their interfaces has emerged as the key driver of PCE improvements. Said this, it has been soon very clear that it was also a critical point in defying the device stability. This review provides a comprehensive overview of degradation mechanisms especially related to interface phenomena and with a special focus on the role of defects. Beginning with an analysis of the intrinsic instability issues of pristine interfacial materials, it will move to the interface-induced instability in perovskite absorber, including chemically driven degradation, defect and phase impurities, ion accumulation and migration, and mechanical delamination. Eventually, it is offered an updated review of approaches to mitigate the instability caused by interfaces limitations, including controllable surface construction, multi-layer interface, and stable transport layer design. Future research directions are proposed to guide the development of durable inverted PSCs toward real-world applications.

Keywords: Interface, p-i-n structure, Degradation pathways, Long-term stability, ISOS protocol

Introduction

Metal halide perovskites have emerged as a groundbreaking class of light-absorbing materials for next generation photovoltaic technologies. These solution-processable materials combine exceptional optoelectronic properties with widely tunable bandgap, making them uniquely suited for both single-junction and tandem cell configurations. Notably, recent advances in perovskite solar cells (PSCs) featuring an inverted p-i-n structure have surpassed the performance of conventional n-i-p predecessor, leading to the realization of the most efficient perovskite-based devices to date.[1, 2] Current certified PCEs based on p-i-n architecture have achieved remarkable milestones: 27% for inverted single-junction PSCs, 34.9% for perovskite-silicon tandems, and 31.6% for all-perovskite tandems.[3, 4]

Over the past several years, the unprecedented achievement of PCE has been largely driven by innovations in charge transport materials (CTM) and refined interface engineering strategies **(Figure 1 and Table S1)**. Also, thanks to innovations in CTMs and interface engineering, the stability of single-junction and tandem solar cells (TSCs) based on inverted structure has greatly improved. It is clear that on one side there has been the need of developing ad hoc aging protocols which were taking into account the nature of such emerging class of semiconductors,[5] on the other side, the refinement of such protocols calls for a clear understanding of the photo-chemical and optoelectronics processing happening at the material and device level.

Perovskite surfaces are rich in defects, which often serve as initiation sites for instabilities such as halide migration and photochemical reactions under external stimuli. Consequently, when CTMs form contact with perovskite absorbers, they alter their defect landscape. Their ability to facilitate charge extraction over defect trapping significantly influences the overall device stability. Moreover, perovskites are susceptible to chemical invasion, meaning the chemical properties and potential degradation of CTMs can substantially accelerate perovskite decomposition. These considerations underscore the critical importance of not only elucidating the intrinsic stability of interfacial materials but also clarifying their impact on the long-term durability of the perovskite absorber. A comprehensive understanding of the challenges encountered by interfacial layers across devices with different bandgaps provides a foundation for targeted solutions, thereby enabling further optimization of device stability.

This review offers an analysis of degradation mechanisms from an interfacial perspective within inverted PSCs. It

is organized into three sections. The first one examines intrinsic instabilities originating from interfacial materials, as well as interface-amplified degradation processes in the perovskite absorber. Specifically, it addresses the intrinsic instability of transport layers under thermal and illumination stress, the nature of the degradation products they generate, and the subsequent impact of these products on the stability of the perovskite absorber. It further discusses how the interactions between functional groups in interfacial layers and the perovskite absorber modulate defect activity and stability. In addition, it considers the decomposition products of perovskites and their influence on the stability and performance of transport layers. The role of energy-level alignment and interface-mediated charge extraction in determining perovskite stability is analyzed. The second section discusses recent advances in interfacial engineering strategies designed to enhance the stability of inverted PSCs under ISOS testing protocols, providing an up-to-date overview of methods to mitigate interface-related degradation. The final section outlines future research directions toward achieving stable and commercially viable operation of inverted PSCs.

View Article Online
DOI: 10.1039/D5EE07642K

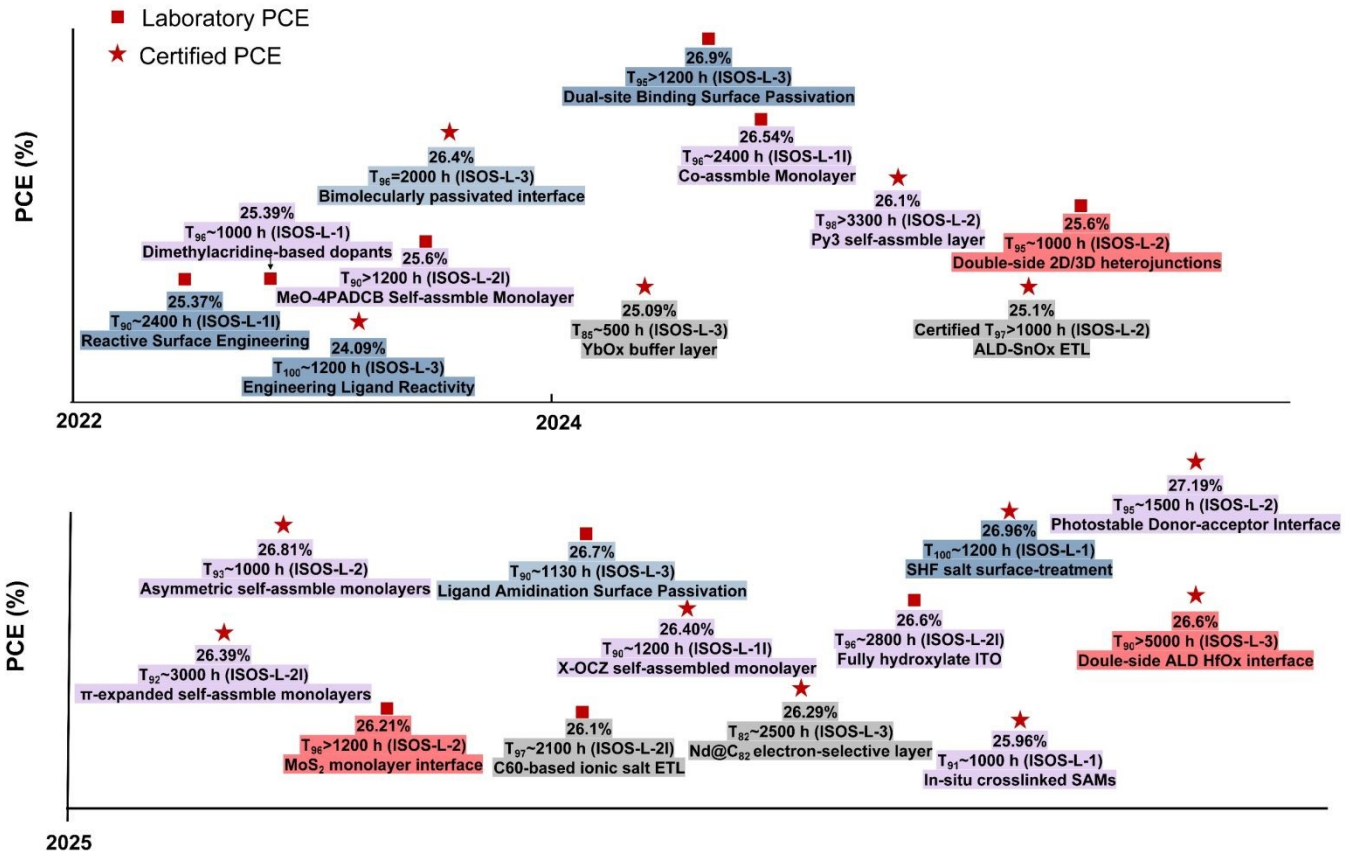

Figure 1. Notable efficiency and operational stability progress of inverted single-junction PSCs. Blue labels represent controllable surface reconstruction.[6-11] Red labels represent constructing robust multi-layered interface.[12-14] Purple labels represent rational design of self-assembled monolayers (SAMs).[15-24] Grey labels represent engineering stable electron transport layers (ETLs).[25-28]

2. Interface Dictated Stability in Inverted PSCs: Advantages and Challenges

2.1 Intrinsic Instability of Charge Transport Layers (CTLs)

The relatively slower advancement of p-i-n perovskite solar cells (PSCs) compared to n-i-p devices has historically been attributed to the limitations of conventional hole-transporting layers (HTLs), such as NiO_x and poly[bis(4-phenyl)(2,3,6-trimethylphenyl)amine] (PTAA). These materials often exhibit suboptimal electrical properties and poor energy level alignment with perovskite absorbers. However, the emergence of self-assembled monolayers (SAMs) as HTLs has reversed this trend. On the other hand, the development of electron extraction layers has been relatively limited to C_{60} and its derivatives, notably [6,6]-Phenyl-C61-butyric acid methyl ester (PCBM), pushing towards the modification of the perovskite surface itself. In this section, we provide a comprehensive overview of the most commonly used CTLs and surface modifiers (**Figure 2**), along with a detailed examination of the challenges related to their intrinsic material stability.

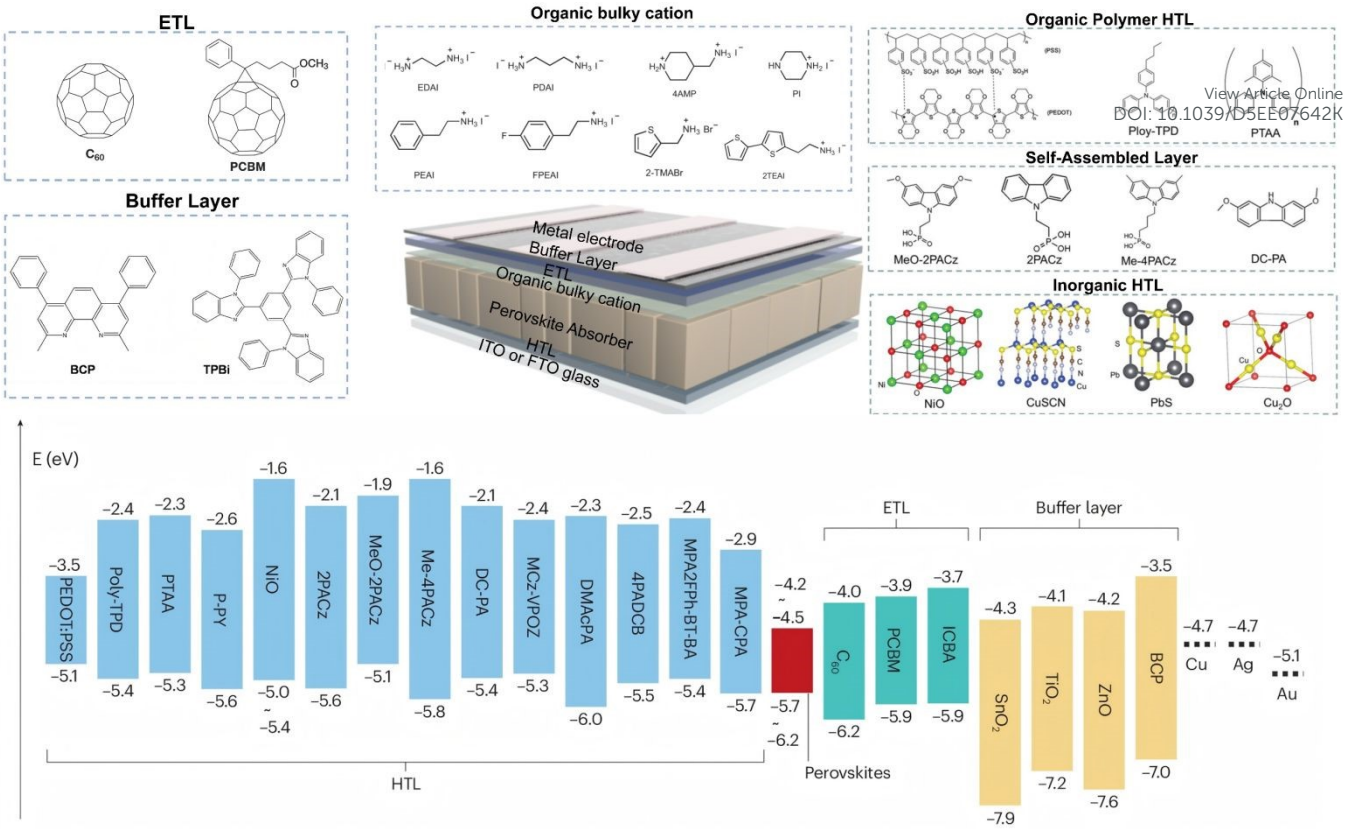

Figure 2. Schematic configuration, corresponding materials and energy-level diagram of functional layers.[29, 30] Copyright 2022 and 2024, Nature Publishing Group.

2.1.1 Polymer Hole Transport Layers

Conductive polymers, such as poly(3,4-ethylenedioxythiophene): polystyrene sulfonate (PEDOT:PSS), PTAA and its derivatives, are widely used HTLs in inverted PSCs owing to their compatibility with low-temperature solution processing and their tunable electrical properties through molecular design.[31]

(1) PEDOT:PSS

Attributed to its excellent optical transmittance, straightforward processing, and extensive prior application in organic photovoltaic systems, PEDOT:PSS has historically been the first HTL used in inverted Pb-based PSCs.[32, 33] By far, PEDOT:PSS becomes the preferred HTL for Sn- and Sn-Pb based inverted PSCs due to its favorable energy-level alignment with these perovskites. PEDOT:PSS consists of two ionically bound components: conductive PEDOT and insulating PSS. The electronic properties of PEDOT are heavily dependent on PSS for charge stabilization and aqueous processability.[33] However, the acidic sulfonate groups in the PSS component can corrode the underlying indium tin oxide (ITO) electrode, leading to the increased series resistance and degraded electrical contact.[34, 35] Additionally, its strong tendency to absorb moisture from the environment accelerates the perovskite decomposition. These factors also constitute one of the underlying reasons for the limited stability observed in Sn- and Sn-Pb based devices. Leveraging PEDOT:PSS as HTL, Sn- and Sn-Pb based inverted PSCs have achieved the record certified PCE of 16.65%[36] and 24.13%[37], respectively. Nonetheless, compared with Pb-based PSCs, the operational stability of Sn- and Sn-Pb counterparts remain unsatisfactory.[38, 39] Current research is advancing along two complementary strategies: (i) optimizing PEDOT:PSS to alleviate its intrinsic defects and achieve better energy-level alignment for efficient hole extraction[40-45], (ii) developing acid-free, hydrophobic, and optically transparent alternative hole contacts for improved long-term device stability[46-51].

(2) PTAA and its derivatives

Later, owing to its high conductivity and chemical stability, PTAA and its derivatives emerged as the widely used polymer HTLs in inverted Pb-based PSCs, which eliminates drawbacks brought by PEDOT:PSS. In the early development of PTAA, doping with hydrophilic molecules such as F4TCNQ was commonly employed to enhance its

electrical conductivity. However, the incorporation of F4TCNQ has been shown to adversely affect device stability due to its hygroscopic nature. Gradually, dopant-free PTAA has emerged as a promising alternative for fabricating more stable inverted PSCs. Benefiting from the ultra-smooth surface of commercial ITO substrates, it is feasible to deposit an ultra-thin layer of undoped PTAA without compromising film uniformity. Through synergistic surface modification, particularly the introduction of a porous Al_2O_3 insulating interlayer that minimizes interfacial contact and passivate the interface, dopant-free PTAA-based inverted PSCs deliver a champion PCE above 25.5% (24.7% certified) and maintain over 98% of the initial efficiency after 1,000 hours of maximum power point tracking (MPPT) under 1-sun illumination (~35-40 °C).[52]

Nevertheless, due to its intrinsic hydrophobicity and low surface energy, PTAA exhibits poor interfacial wettability with perovskite precursor solutions. This interfacial incompatibility often results in non-uniform perovskite film formation, promoting the emergence of morphological defects and voids.[53, 54] Moreover, PTAA features a relatively shallow highest occupied molecular orbital (HOMO) level, which compromises energetic alignment with a broad range of perovskite compositions. Additionally, the absence of intrinsic passivating groups in PTAA hinders its ability to suppress interfacial trap states and defect-induced ion migration, both of which contribute to long-term degradation pathways in PSCs.[30] To tackle these challenges, molecular engineering of PTAA has been explored, such as removing alkyl groups and adding pyridine rings as multifunctional anchors, or changing the pyridine linkage sites.[55, 56] These modifications help create deeper HOMO levels for better energy alignment with the perovskite, and improves interface properties and surface wettability, enabling the formation of high-quality perovskite/HTL interface, thus improving the device stability.

2.1.2 Self-assembled Monolayers

Self-assembled monolayers (SAMs) based hole selective layers were initially introduced in PSCs quite some time ago[57, 58]; however, their application has garnered renewed attention following the development of a series of carbazole-derived molecules functionalized with phosphonic acid anchoring groups (e.g. 2PACz, Me-2PACz, Me-4PACz, and 4PADCB). The integration of these SAMs, either as a replacement for or in conjunction with traditional materials such as poly(triarylamine) (PTAA) and NiO_x, catalyzed a boost advancement in the performance of inverted PSCs, with the PCE now exceeding 27%, underscoring their transformative role.[7, 59-61]

A typical SAM consists of three fundamental components: an anchoring moiety, a molecular spacer (linker), and a terminal functional group **(Figure 3A),** each play a distinct role in interacting with the metal oxide (MO), adjacent molecules, and the perovskite layer. These interactions collectively determine the chemical and structural stability of the HTL/perovskite interface. (1) The anchoring moiety, often a Brønsted-Lowry acid such as phosphonic acid (PA, -$PO(OH)_2$), enable the attachment to MO surfaces via coordination bonding (P-O-M) and surface reactions.[62] The binding strength of the SAM/MO interaction is determined by the inherent chemical characteristics of the SAM's anchoring groups and the MO surface.[63, 64] (2) The linker, commonly composed of alkyl chains or conjugated aromatic units, provides spatial separation and molecular flexibility, ensuring the formation of a well-ordered monolayer.[65, 66] (3) The terminal group imparts the SAM with specific interfacial functionalities, tuning key parameters such as surface energy, electronic alignment, and charge transport dynamics at the interface.[67] The linker and terminal groups govern π-π interactions between SAM molecules, which are essential for molecular ordering, anchoring robustness, and surface uniformity.

Although the monolayer architecture of SAMs allows for ideal interfacial contact, it also makes them susceptible to degradation or desorption, especially under light and thermal stress **(Figure 3B)**. Understanding the stability issues of SAMs requires examining their formation process. Tethering aggregation and growth (T-BAG) method is widely used to prepare phosphonic acid (PA)-based SAMs on transparent conductive oxide (TCO) substrates.[68-70] The process typically involves three steps: (1) deposition of a thin PA layer on the MO surface, where weak secondary interactions (e.g., hydrogen bonding or van der Waals forces) form a physisorbed layer;[71, 72] (2) thermal annealing, which promotes dehydrative condensation between hydroxyl groups on the TCO surface and PAs to form covalent P-O-M bonds; and (3) rinsing to remove physisorbed species, leaving a chemically anchored monolayer.[73] Given this formation pathway, the instability of SAMs can arise from molecular-scale structural and interfacial evolution. Based on their molecular

View Article Online
DOI: 10.1039/D5EE07642K

structures and interfacial interactions, these instability mechanisms can be categorized into three levels. (i) Within the SAM layer, molecular chemical denaturation and packing disorder threaten structural integrity.[74-76] PA molecules may form hydrogen bonds through P-OH or P=O groups with neighboring molecules or surface hydroxyl groups. These weak interactions can lead to desorption during washing or under light and thermal stress. Moreover, since SAMs are molecularly thin interfacial layers with thickness typically at the nanometer scale, even slight variations in molecular orientation, deprotonation degree, or intermolecular interactions can significantly alter interfacial dipoles and charge-transport characteristics. Insufficient molecular packing or non-uniform surface coverage lead to the variations in wettability toward the perovskite precursor solution, directly influencing crystallization dynamics during perovskite deposition, and amplifying device-to-device variability. These subtle structural and surface-energy fluctuations not only reduce long-term stability but also magnify interfacial heterogeneity during device operation. (ii) At the SAM/MO interface, anchoring is governed by surface-limited chemical bonding, primarily through P-O-M bonds.[21, 22, 77] Consequently, long-term stability strongly depends on the integrity of these interfacial bonds. External stresses, such as thermal stress, electric fields, or mechanical strain, can weaken or break these bonds, leading to partial SAM desorption. Stable SAM formation thus requires maximizing covalent bonding while minimizing weak physisorption.[78] To increase the availability of reactive sites, strategies such as introducing multiple anchoring groups in SAMs and/or optimizing MO substrate treatments have been employed to enhance interfacial exposure and improve anchoring efficiency. (iii) At the SAM/PVK interface, weakened interactions between terminal groups and perovskite under operational stress can reduce passivation and interfacial contact, accelerating perovskite degradation.[79, 80] Additionally, mismatched band-alignment at the SAM/PVK interface greatly influences interfacial extraction, accelerating interface reactions and electric field-induced ion migration during device operation.[81] Thus, electronic and chemical instability become strongly coupled, leading to progressive evolution of the HTL/perovskite interface in inverted PSCs and making degradation pathways more intricate and less predictable.

These pronounced interfacial sensitivities are further amplified during the transition from laboratory-scale fabrication to large-area processing.[82] As device dimensions increase, even slight variations in molecular coverage or anchoring density can propagate into significant performance inhomogeneity. Although SAMs perform well in small-area devices, commonly used methods such as spin-coating and dip-coating often fail to ensure uniform, and high-quality coverage over large surfaces. For large-area perovskite modules, monolithic interconnection (P1-P2-P3 laser scribing) is used to reduce series resistance and maintain a high fill factor.[83] During P1 scribing, parts of the glass substrate are exposed. When hydrophobic SAMs such as Me-4PACz are deposited, the wettability difference between glass and ITO can lead to non-uniform perovskite coating. This often results in pinholes and electrical shunts between sub-cells, degrading module performance (**Figure 3C**).[49] Therefore, developing scalable deposition techniques such as co-assembled monolayer by additives that enable homogeneous and defect-less SAM formation is essential for advancing toward industrial-scale module fabrication.[82, 84]

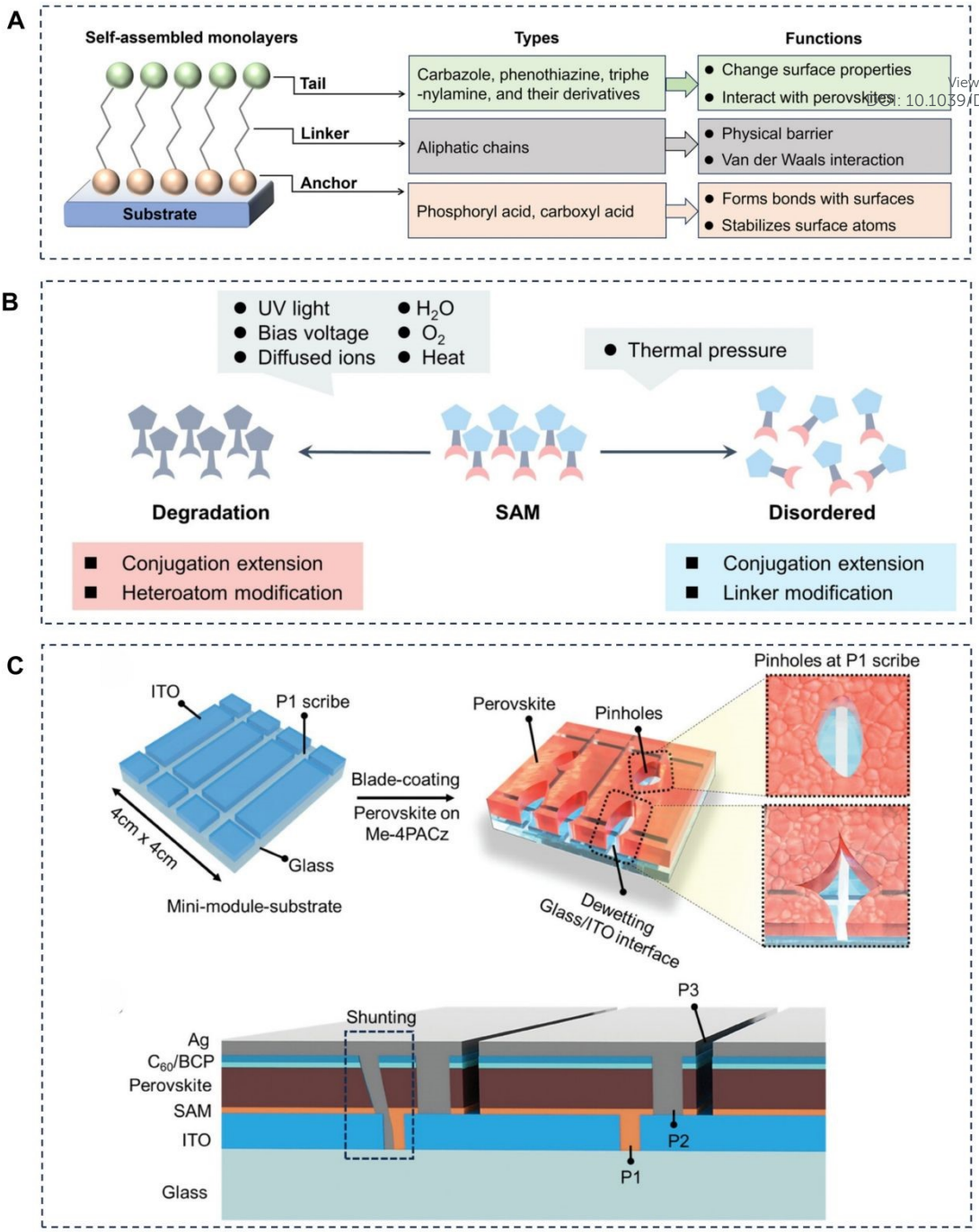

Figure 3. (A) Schematic illustration of the structure, types, and functions of SAMs.[85] Copyright 2019, Wiley-VCH. (B) The illustration of the failure of the inner layer of the SAM under external pressure and the corresponding molecular design.[74] Copyright 2023, Wiley-VCH. (C) Schematic highlighting the module design and coating challenges on Me-4PACz at P1 scribe areas, and potential device shunting due to pinholes on perovskite film.[82] Copyright 2024, Wiley-VCH.

2.1.3 Inorganic Hole Transport Layers

Compared to organic HTLs, inorganic HTLs offer superior intrinsic stability against heat and moisture. A variety of p-type inorganic semiconductors have been investigated in inverted PSCs, including antimony-doped tin oxide (ATO), NiO_x, and a range of copper-based compounds such as copper oxide (CuO_x), and copper thiocyanate (CuSCN). NiO_x has attracted significant attention as a low-cost, highly transparent HTL with a suitable work function. However, the complex chemical properties of NiO_x raise concerns regarding the long-term stability of devices. NiO_x exhibits photocatalytic activity and can be oxidized to Ni_2O_3 under light and oxygen exposure.[86, 87] Moreover, NiO_x based devices have shown degradation under electrical bias and thermal stress (e.g., aging at 85°C in N_2).[88, 89] The NiO_x/perovskite interface often suffers from chemical reactions between high-valence $Ni^{\geq 3+}$ ions and perovskite precursors, leading to

serious interfacial recombination and material degradation (a detailed discussion is provided in section 2.2.1). Additionally, the energy levels of NiO_x are highly sensitive to its preparation method and conditions, while lattice mismatch with the perovskite can further introduce interfacial defects and compromise device stability. Therefore, rational surface engineering of NiO_x HTL is critical for enabling stable inverted PSCs.

View Article Online
DOI: 10.1039/D5EE07642K

2.1.4 Electron Transport Layers

In inverted PSCs, ETLs must have suitable energy-level alignment for efficient electron extraction, high conductivity and mobility for scalable fabrication, chemical and thermal stability to protect the perovskite, and excellent optical transparency, commonly achieved using fullerene derivatives, n-type conjugated polymers, or n-type metal oxides.[30] Fullerene-based ETLs, including C_{60}, PCBM, and derivatives like C_{60}-bis, ICBA, and CMC, are widely used in high-performance inverted PSCs due to their high electron mobility and low-temperature processability. They can be applied singly, in bilayers (e.g., PCBM/C_{60}), or as blends (e.g., CMC + ICBA) to optimize highest occupied molecular orbital (LUMO) alignment with the perovskite.[90, 91] Beyond charge transport, fullerene ETLs also enhance stability, partly via the "scavenging effect".[92, 93]

While fullerenes, have been integral to high-performance inverted PSCs, emerging challenges, such as energetic disorder, mechanical fragility, and high cost, are increasingly recognized as barriers to continued progress.[94-99] However, high-quality C_{60} films are typically obtainable only via thermal evaporation, due to C_{60}'s poor solubility in most solvents stemming from the lack of solubilizing functional groups on its carbon cage.[100] In contrast, PCBM fabricated by solution-processing is prone to thermal- or/and light-induced dimerization on perovskite surface, which reduces the uniformity of PCBM layers and diminishes its charge transport capability.[101-103] Unlike very thin SAMs, PCBM needs thicker films—tens of nanometers—making it harder to form uniform layers. While this is less problematic for small lab-scale devices (< 0.1 cm^2), it becomes a major issue when scaling up.[104]

To further optimize interfacial energetics, a buffer layer, commonly bathocuproine (BCP), is typically introduced between the fullerene and the top electrode. However, BCP suffers from poor thermal stability under the 85°C specified by the ISOS protocol, which limit the outdoor stability.[28, 105] These drawbacks have prompted a shift toward exploring alternative, non-fullerene ETL materials, such as atomic-layer-deposition (ALD) SnO_2[106], Zn-doped SnO_2 (ZTO)[107], and organometallic complexes[108]. Inorganic metal oxides (e,g., SnO_2) onto perovskite films are gaining momentum, eliminating the need for fullerene-based interlayers (which will be discussed in section 3.5).

2.2 Interface-Amplified Instability Mechanisms in Perovskite Absorber

2.2.1 Chemically Driven Decomposition

Chemically driven decomposition encompasses: (i) the activation of detrimental defect sites at the interface between the perovskite absorber and the CTLs; (ii) the subsequent generation of secondary species, such as molecular iodine (I_2), further exacerbating instability by chemical reactions and irreversible structural degradation.

(1) PEDOT:PSS/Narrow-bandgap (NBG) Perovskite Interface

Poly(3,4-ethylenedioxythiophene):poly(styrene sulfonate) (PEDOT:PSS) is the most widely used HTL in Sn- and Sn-Pb based NBG single-junction and tandem devices, owing to its relatively shallow valence band, which enables favorable energy level alignment with Sn-Pb perovskites and facilitates efficient hole extraction, thereby delivering some of the highest reported efficiencies in this field.[109-113] However, PEDOT:PSS is notorious for deteriorating NBG PSCs under external stimuli. A major drawback of PEDOT:PSS is the acidity of its polystyrene sulfonate (PSS) units, which act as dopants to enhance PEDOT's conductivity.

On the one hand, due to its low acid dissociation constant (pK_a), the sulfonic acid (-SO_3H) group in PSS units can undergo a neutralization reaction with SnF_2, an indispensable basic additive which is a necessary for preparing the high quality NBG perovskite film to retard the repaid crystallization through neutralization reaction (-SO_3H + SnF_2 →-SO_3^-…Sn^{2+} + HF).[43] The interfacial reaction can alter the interface's chemical properties and accelerate the degradation of NBG PSCs (**Figure 4A).** On the other hand, amines iodide (AI) which diffuses from the breakdown of perovskite absorber into PEDOT:PSS could react with PSS through the reaction of 4AI + 4PSSH + O_2 → 4PSS$^-A^+$ + $2H_2O$ + $2I_2$.[114] This process leads to the deactivation of PSS and subsequent de-doping of PEDOT:PSS, greatly influencing the hole extraction and interface stability. Meanwhile, the local interfacial chemical environment critically amplifies these I_2-

View Article Online
DOI: 10.1039/D5EE07642K

mediated degradation pathways. Further evolution of the formed I_2 is identified as a major culprit behind degradation of Sn- and Sn-Pb based perovskites. Once generated, I_2 participates in multiple parasitic reactions that destabilize the lattice. First, I_2 easily reacts with organic cations (e.g., methylammonium) within Sn-containing perovskites by hydrogen bonding, further promoting the formation of corrosive triiodide (I_3^-) species, AI_3 byproducts (**Figure 4B**).[114, 115] In parallel, I^- of perovskite acts as a Lewis base while I_2 behave as a Lewis acid, resulting in a homogeneous reaction ($I^- + I_2 \leftrightharpoons I_3^-$). The generation of I_3^- intermediates promotes further I_2 volatilization which happen mainly at the surface under both inert and ambient conditions (**Figure 4C**).[116] More critically, I_2 acts as a strong oxidizing agent, converting lattice Sn^{2+} and forming SnI_4 (e.g., $2APb_{0.5}Sn_{0.5}I_3 + I_2 \rightarrow 2AI + PbI_2 + SnI_4$). This reaction not only disrupts the perovskite framework but also regenerates reactive iodine species, establishing a self-sustaining, I_2-driven redox cycle that accelerates absorber decomposition.[115, 117] Overall, I_2 functions both as a reactive intermediate and a catalytic oxidant, making its formation and accumulation central to the intrinsic instability of Sn-containing perovskites. When replacing HTL featuring the carboxyl (-COOH) group with a higher pK_a, such as poly[3-(4-carboxybutyl)thiophene-2,5-diyl] (P3CT), these reaction at the HTL/perovskite interface was greatly suppressed, which endowed the all-perovskite TSCs with T_{97} operational lifetime (time required for the device efficiency to drop to 97% of its initial value) exceeding 1,000 hours.[118]

(2) NiO_x/Perovskite Interface

NiO_x/perovskite interface suffers from a detrimental redox reaction between Ni^{3+} and I^- of perovskite absorber ($2Ni^{\geq 3+} + 2I^- \rightarrow 2Ni^{\geq 2+} + I_2$), which triggers the severe interfacial degradation and impedes charge carrier collection.[65] Inevitably, the consumption of I^- induces the further formation of iodide vacancies (V_I)[119, 120], which can intensify halide migration under illumination and electrical bias, causing hysteresis and further material degradation. I_2 as a product of such a redox reaction, is highly reactive and can initiate multiple degradation pathways of perovskite.

First, I_2 can react with I^- to form the triple halide ion (I_3^-, $I_2 + I^- \leftrightharpoons I_3^-$), and in the chemical environment of MA^+ or FA^+, such a species is liquid and at room and higher temperature ($I_3^- + CH(NH_2)_2^+ \rightarrow NH_3\uparrow + HCN\uparrow + HI_3$, $I_3^- + CH_3NH_3^+ \rightarrow CH_3NH_2\uparrow + HI_3$).[121] Such triple halide melt is corrosive to perovskite and induces the voids formation in the perovskite film. Second, I_3^- lowers the deprotonation energy barrier for organic cations (MA^+ and FA^+), facilitating the loss of MA and FA and thus the easier decomposition of perovskite (**Figure 4D**).[122] The formation of PbI_2 is commonly accompanied by the loss of organic cations. It has been reported that defects in PbI_2 can capture charge carriers generated within itself, or capture holes from the perovskite, to further produce I_2 and metallic lead (Pb^0) ($PbI_2 \rightarrow Pb^0 + I_2\uparrow$).[123, 124] Under illumination, I_3^- participates in photochemical reactions that generate corrosive iodine radicals through a cascade process ($I_3^- + hv \longrightarrow I^{\cdot} + I_2^{\cdot -}$). These radicals further exacerbate the decomposition of the perovskite lattice and trigger a chain reaction that compromises stability of various perovskite systems.

Meanwhile, I_2 triggers the phase transition from the active α-phase of $FAPbI_3$ perovskite to the non-photoactive δ-phase.[125] Elevated temperatures can further accelerate this process by promoting I_2 volatilization, ultimately leading to the irreversible perovskite degradation. In lead-based mixed halide perovskites, as shown in **Figure 4E**, our group demonstrate that photogenerated I_2 reacts with bromide ions (Br^-) to form trihalide ions I_2Br^- ($I^{\delta-}$+$I^{\delta+}$-$Br^{\delta-}$), from which the negatively charged iodide ($I^{\delta-}$) can then exchange with another lattice Br^-, resulting in the formation of an iodine-rich phase ($Br^- + I_2 \leftrightharpoons I_2Br^-$ (1), $I_2Br^- + Br^- \leftrightharpoons IBr_2^- + I^-$ (2))[68]. For NBG perovskite, the interfacial instability becomes even more pronounced, as the high-valence Ni^{3+} species not only react with I^- ions but also oxidize Sn^{2+} to Sn^{4+}, thereby imposing a significant barrier to the direct replacement of PEDOT:PSS with NiO_x as the HTL in Sn-containing systems. In our group, we have further demonstrated that the photo-instabilities in perovskites originate from the light-induced creation and annihilation of iodide-related defects, which act as carrier trap states.[126] These competing processes, photoluminescence intensity enhancement (PLIE, $I_i^+/I_i^- \cdots V_I^+ + e^- \rightarrow I_i^0/I_i^- \cdots V_I^+ \rightarrow I_i^0$ + Pristine material) and photoluminescence intensity degradation (PLID, $I_i^+/I_i^- + e^- \rightarrow I_i^0/I_i^- + h^+ \rightarrow 2I_i^0 \rightarrow I_2$) (**Figure 4F**), are governed by the dynamic formation of surface-coordinated I_2. The stabilization of I_2 at surfaces or grain boundaries serves as the key trigger for the harmful PLID. Once surface-bound I_2 accumulates, the resulting iodine imbalance between surface and bulk drives a series of compensatory redox and ionic redistribution reactions that regenerate the bulk I_i^+/I_i^- defect population. This feedback loop accelerates structural decomposition and deteriorates both film and device stability.

$Ni^{\geq 3+}$ defect sites also show Brønsted acid-base character and can deprotonate organic ammoniums during the film formation, leading to the loss of A-site cations as amine gases from the perovskite ($APbI_3 + Ni^{\geq 3+}O_x \rightarrow Ni^{\geq 2+}O_xH + PbI_2 + A(g) + 1/2I_2$) (**Figure 4G**).[69] This will leads to the remaining Pb^{2+} and halide ions to transform PbI_xBr_{3-x} at the NiO_x/perovskite interface, which is photo unstable and also serve as a barrier to charge extraction, thereby limiting the open-circuit voltage (V_{oc}) and long-term stability of the devices. By a non-destructive, fabrication-compatible, and universally effective technique, Hou et al. uncovered that all perovskite/metal oxide interfaces undergo similar deprotonation processes of organic ammoniums (e.g., FA^+) albeit to different extents, which lead to the formation of interfacial defects and degradation sites (such as PbI_2, Pb^0, **Figure 4H**).[127]

View Article Online
DOI: 10.1039/D5EE07642K

(3) Perovskite/Ammonium based Ions Passivation Layer Interface

State-of-the-art inverted PSCs utilize organic ammonium ligands (e.g., phenylethylammonium, ethylenediamine) to passivate surface defects and suppress nonradiative recombination at the perovskite/ETL interface. These ammonium cations, along with the tunable chemical functionalities of the ligands, can either form a thin molecular passivation layer on the perovskite surface or promote the formation of a low-dimensional (LD, typically two-dimensional, 2D) perovskite capping layer atop the underlying three-dimensional (3D) perovskite.[10, 128-130] Phenylethylammonium (PEA^+) based cationic species, including derivatives such as 4-(trifluoromethyl)phenethylammonium (CF_3PEA^+), 4-fluorophenethylammonium ($FPEA^+$), typically induce the formation of a low-dimensional (2D or quasi-2D) perovskite capping layer on the surface of the 3D absorber. The resulting 2D overlayer enhances stability by increasing the activation energy for halide ion migration, thereby creating a more compact lattice framework.[131, 132] Diammonium cations such as ethylenediammonium (EDA^{2+}) and 1,3-propanediammonium (PDA^{2+}) can form bifunctional interfacial linkages that generate interfacial dipoles and effectively passivate surface defects.[113, 133-135] By reducing trap-assisted recombination and facilitating charge extraction at the perovskite/C_{60} interface, these passivators mitigate charge accumulation and electric-field-driven ion migration, contributing to improved operational stability. Critically, the conformality of the passivation layer or LD capping layer directly influences device efficiency by modulating interfacial band alignment and charge extraction, as well as operational stability by suppressing ion migration and limiting moisture ingress.

However, the persistence of these benefits depends on the chemical stability of the passivators, and the durability of the passivating efficacies. The durability of the passivation efficiency, whether achieved through LD phase formation or interfacial dipole engineering, is governed by the resistance of the organic cations to deprotonation, thermal stress, and chemical evolution under operating conditions. Notably, cations with relatively low acid dissociation constants (pK_a), insufficient steric hindrance, high chemical reactivity, or weak interfacial binding, such as n-butylammonium (n-BA^+) and phenylethylammonium (PEA^+), may undergo deprotonation or structural rearrangement at elevated temperatures.[136-138] This process leads to the formation of volatile amines and halide species. The generated amines can further undergo transamination reactions with the perovskite lattice, accelerating surface degradation.[139] This deprotonation not only compromises the passivation functionality but also introduces additional vacancy defects on the perovskite surface during extended operation. Consequently, even the most efficient PSCs (with PCEs ≥ 25%) often suffer from limited operational stability. For instance, under MPPT at 85°C and 50% relative humidity (RH) (ISOS-L-3 protocol), the T_{80} lifetime typically plateaus at around 500 hours.[11]

One illustrative example is the widely used phenylethylammonium (PEA^+) cation, which, despite its passivation benefits, has been shown to markedly impair the photothermal stability of FA-based perovskites, regardless of the incorporation method.[140] The impact of PEA^+ on intrinsic stability of FACs-based perovskite was evidenced by the perovskite morphology and crystallinity evolution after light soaking at 85°C for different durations (**Figure 4I**). The underlying mechanism involves the low pK_a, PEA^+ easily react with FA^+ ions through the deprotonation of PEA^+ to neutral PEA^0 followed by a rapid condensation reaction between PEA^0 and FA^+ to form (phenethylamino)methaniminium ($PEAMA^+$) ($PEA^+ \leftrightharpoons PEA^0 + H^+$ (1), $PEA^0 + FA^+ \rightarrow PEAMA^+ + NH_3\uparrow$ (2)) **(Figure 4J)**, which render PEA^+-based 2D perovskites transferring from lower-n 2D phases to higher-n 2D phases (n = 3) after annealing at 120°C for 130 hours. Additionally, this generates ammonia, which causes damage to perovskite interfaces and grain boundaries, severely limiting the high-temperature photostability of devices. By contrast, butanimidamidinium

(BAD$^+$) and deprotonated propanediimidamide (PDI^{2+}) exhibit higher pK_a values than typical ammonium cations, indicating greater resistance to deprotonation and improved interfacial stability.[11] Despite recent advances, suppressing the deprotonation of organic A-site cations remains a key challenge. Rational molecular design focused on enhancing acid-base stability and structural robustness is essential for achieving durable large-cation interfaces in inverted PSCs.

View Article Online
DOI: 10.1039/D5EE07642K

(4) Reactions at the Perovskite/ETL/Electrode Interface

Fullerene-based ETLs (e.g. PCBM, C_{60}) are particularly susceptible to degradation due to their inherently porous structure, which facilitates the intercalation of halide ions, especially iodide ion (I^-).[141] At the perovskite-fullerene interface, the halide anion-fullerene π interactions can lead to the highly conductive n-doped fullerene, which can enhance the electron transport and contributes to the improved device performance while also reducing hysteresis.[68, 142] However, the I^- ion can diffuse through the fullerene-based ETL and then accumulate at the metal electrode surface.[143] The I^- ion readily react with metal electrodes, causing the irreversible device degradation, especially under light and thermal stress. This degradation is often observed indicated by a yellow color change resulting from the reaction between I^- ions and silver ($2Ag + I_2 \rightarrow 2AgI$). Even more inert metals like gold (Au) can corrode when exposed to polyiodide melts (MAI-nI_2) formed by volatile I_2 and MAI from the perovskite layer.[144]

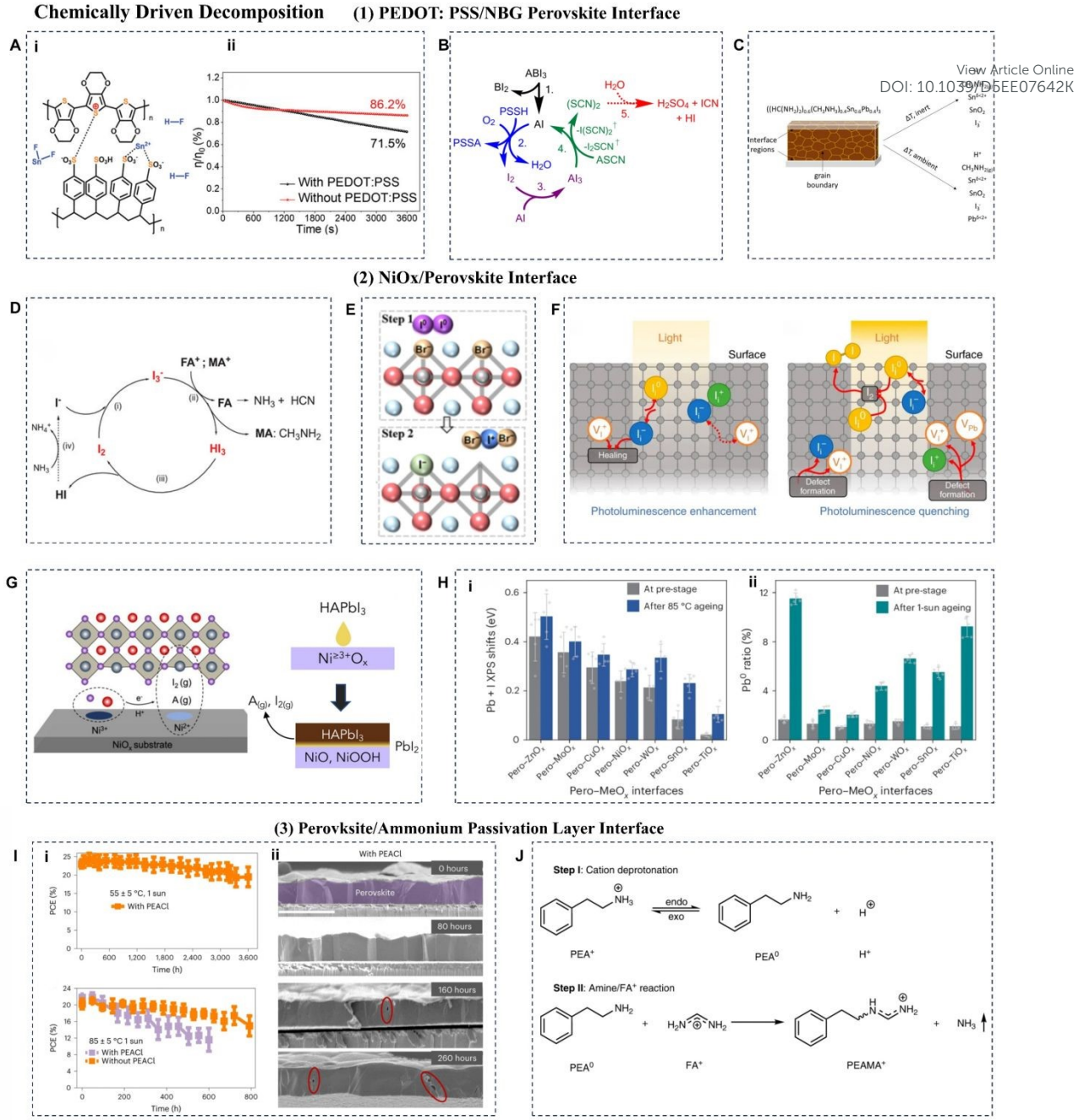

Figure 4. Chemically Driven Decomposition. (A) (Ai) Possible side reaction products at PEDOT:PSS/perovskite interface. (Aii) Photo-stability of the Sn-Pb PSCs with and without PEDOT:PSS.[43] Copyright 2023, Wiley-VCH. (B) Reaction scheme for the interfacial chemistry occurring between PEDOT:PSS and perovskite.[114] Copyright 2025, Royal Society of Chemistry. (C) Schematic of proposed chemical degradation mechanism in perovskite surface, including interfacial regions between the PAL and charge collective layers as well as grain boundaries.[116] Copyright 2020, American Chemical Society. (D) The catalytic effect of I_2 on the decomposition of MA^+ or FA^+.[122] Copyright 2023, Wiley-VCH. (E) I_2 induces I-rich phase formation and halide segregation[145]. Copyright 2023, Wiley-VCH. (F) Photoluminescence enhancement and quenching mechanisms.[126] Copyright 2019, Nature Publishing Group. (G) Schematic of NiO_x/perovskite interface reaction.[146, 147] Copyright 2020 and 2025, Cell Press. (H) (Hi) The correlation between interface fracture energy and interface proton transfer interaction intensity. (Hii) Zn K-edge XANES spectra of ZnO_x in the Pero-ZnO_x interface at the pre-stage of PSCs.[127] Copyright 2025, Nature Publishing Group. (I) (Ii) PCE of encapsulate devices with PEACl as a function of measurement time (top) under ~55 °C and (bottom) ~85 °C 1-sun illumination at open circuit conditions in N_2. (Iii) Cross-sectional SEM images of PSCs prepared with PEACl after stability measurement under ~85 °C 1-sun illumination at open circuit conditions in N_2. (J) Reaction scheme of PEA^+ with FA^+.[138] Copyright 2023, Nature Publishing Group.

2.2.2 Detrimental Point Defects and Phase Impurities

(1) Interface Defects

The detrimental defects within PSCs are mostly accumulated at the interface between the charge transport layers and the perovskite layer.[148-151] The grain surface charge trap densities of the polycrystalline films have been found to be one to two orders of magnitude higher than those in the grain bulk.[152] At the atomic level, the perovskite surfaces can host three types of intrinsic defects: interstitials, anti-site defects, and vacancies.[153] Unlike bulk defects that typically form shallow traps, surface defects, characterized by low formation energies due to varied terminations and undercoordinated sites, tend to create deep traps. The trappings of charge carriers at these defects under external stimuli such as light and bias can initiate chemical reactions and degradation of the interface, which is highly detrimental to the long-term operational stability of the devices.

Iodide interstitials (I_i^+ and I_i^-) represent one of the most fatal and active defects which deteriorate device stability. As shown in **Figure 5A**, I_i^- undergoes a rapid trap-filling process by capturing holes to form neutral iodide ($I_i^- + h^+ \rightarrow I_i^0$). I_i^0 typically combines with an adjacent I^- to form a I_2^- species.[126, 154, 155] I_i^+ exists in the form of the trimer I_3^-, which can capture electrons to form I_i^0.[126] Subsequently, two I_i^0 centers can recombine to form an I_2 molecule ($2I_i^0 \rightarrow I_2$), which not only initiates a several chain reactions within the perovskite as mentioned above, but also reacts with charge transport layers. Li et al. found that HTL can capture photogenerated I_2 from the adjacent perovskite in the form of $[HTL]^+/I_3^-$ or $[HTL]^+/I^-$, by transferring electrons to I_2 from the HOMO of the HTL. This leads to the degradation of the HTL/perovskite interface in inverted PSCs. Huang et al. demonstrated that reverse-bias can promote the reaction between iodide interstitials (I_i^-) and injected holes (trap-filling process, $I_i^- + h^+ \rightarrow I_i^0$) at the perovskite/$C_{60}$ interface. I_i^0 would be further oxidized to I_i^+ followed by the valence band (VB) oxidation with the injected holes ($VB + h^+ \rightarrow h^+@VB$, $h^+@VB + I_i^0 \rightarrow I_i^+$), resulting in the I_i^+ accumulation of starting from the perovskite/C_{60} interface. (**Figure 5B**).[156] A more recent study by their group also elucidated that the UV light can cause the degradation of PTAA/perovskite interface by preferentially inducing the formation of I_i^+.[157] As shown in **Figure 5C**, UV radiation can disrupt primary chemical bonds within PTAA and perovskites, as well as weaken the secondary bonding at the ITO/PTAA/perovskite interface. This process accelerates I^- migration to generate a higher concentration of I_i^+, which promotes excess hole accumulation and thus facilitates A-site cation migration and phase segregation at the HTL/perovskite interface.

Sn-based perovskites are primarily limited by both the facile oxidation of Sn^{2+} to Sn^{4+} and iodide chemistry. Snaith's group demonstrated that the dominant degradation mode in Sn-Pb PSCs under combined heat and light stress (ISOS-L-2) changes with different hole transport materials, which is attributed to variations in iodine vacancy (V_I) generation rates influenced by the interaction between CTL and the perovskite absorber.[158] As shown in **Figure 5D**, the dominant degradation pathway in devices with PEDOT:PSS is the redistribution of mobile ions, driven by a rapid increase in V_I caused by chemical reactions between the perovskite and the acidic PEDOT:PSS. In contrast, devices with PTAA exhibit less ion-redistribution-related degradation, likely due to weaker chemical interactions between PTAA and iodine in the perovskite.

(2) HTL/Perovskite Interface Impurities

In inverted PSCs, the HTL not only functions to extract and transport holes but also plays a crucial role in directing perovskite crystallization and determining the quality of the resulting perovskite film. Poor HTL properties can lead to heterogeneous nucleation, or unreacted precursors at the HTL/perovskite interface. For example, the intrinsic hydrophobic property makes the PTAA layer incompatible with the polar perovskite precursor solution, thus hindering the growth of high-quality perovskite film.

At the PTAA/perovskite interface, on one hand, Huang et al. found that the numerous voids existing at the PTAA/perovskite interface can act as reservoirs for decomposition products such as I_2 and initialize the film degradation under illumination.[54] These voids originate from the shrinkage of perovskite layers owing to the removal of residual DMSO and the conversion of amorphous phase to the crystalline phase.[159] However, they also revealed that the amorphous phase instead of voids is the primary source of iodide interstitials (I_i^-) which are the dominant defects responsible for light- and thermal-induced degradation.[160] On the other hand, the incomplete conversion of the immediate phase also leads to large flaky lead-halide ($PbI_{2-x}Br_x$) grains at the PTAA/perovskite interface, which are

both larger and more abundant than those observed on the top side **(Figure 5E)**. These submicron imperfections can further trigger interfacial reactions and non-radiative recombination, leading to serious interfacial energy losses and instability issues of devices.[161]

View Article Online
DOI: 10.1039/D5EE07642K

Additionally, grain surface concavities (GSCs) at the HTL/perovskite interface, which have long been overlooked in morphological studies, also compromise structural integrity and weaken the micro-heterointerface between perovskite grains and HTL.[162-164] As shown in **Figure 5F**, during thermal cycling tests, the accumulated thermal stress on the convex ridges easily causes interfacial delamination at the micro-heterointerface. Moreover, GSCs facilitate moisture ingress and impede heat dissipation, leading to the accumulation of moisture and heat at these micro-heterointerfaces. Furthermore, the exposed surfaces of GSCs are susceptible to photothermal decomposition, exacerbating the devices degradation.[162]

(2) **Perovskite/ETL Interface Impurities**

On the one hand, studies by Huang et al. revealed the presence of defective nanocrystals and some amorphous phases on the surface of the perovskite film (approximately 0-50 nm), the area approaching C_{60} ETL **(Figure 5G)**.[165] These nanoscopic impurities create more open and defect-prone structures resembling grain boundaries, resulting in the reduced surface hardness, improving the permeability to moisture and oxygen, and accelerating the ion migration and the subsequent formation of iodide interstitials.[160]

On the other hand, fullerene-based ETLs, particularly C_{60}, have been reported to introduce additional trap states within the perovskite bandgap.[96] The perovskite-fullerene interface is a dominant origin of voltage loss in devices, due to work function overlap that creates interfacial trap states. According to the study by Stolterfoht et al., the major contribution to C_{60}-induced recombination loss arises from its very first monolayer, rather than from the C_{60} bulk or the uncovered perovskite surface. Experimental evidence confirms that interfacial C_{60} molecules act as deep trap states upon direct contact with perovskite **(Figure 5H)**.[166] These traps impurities not only hinder charge extraction, but also compromise interface stability and thus device lifespan.

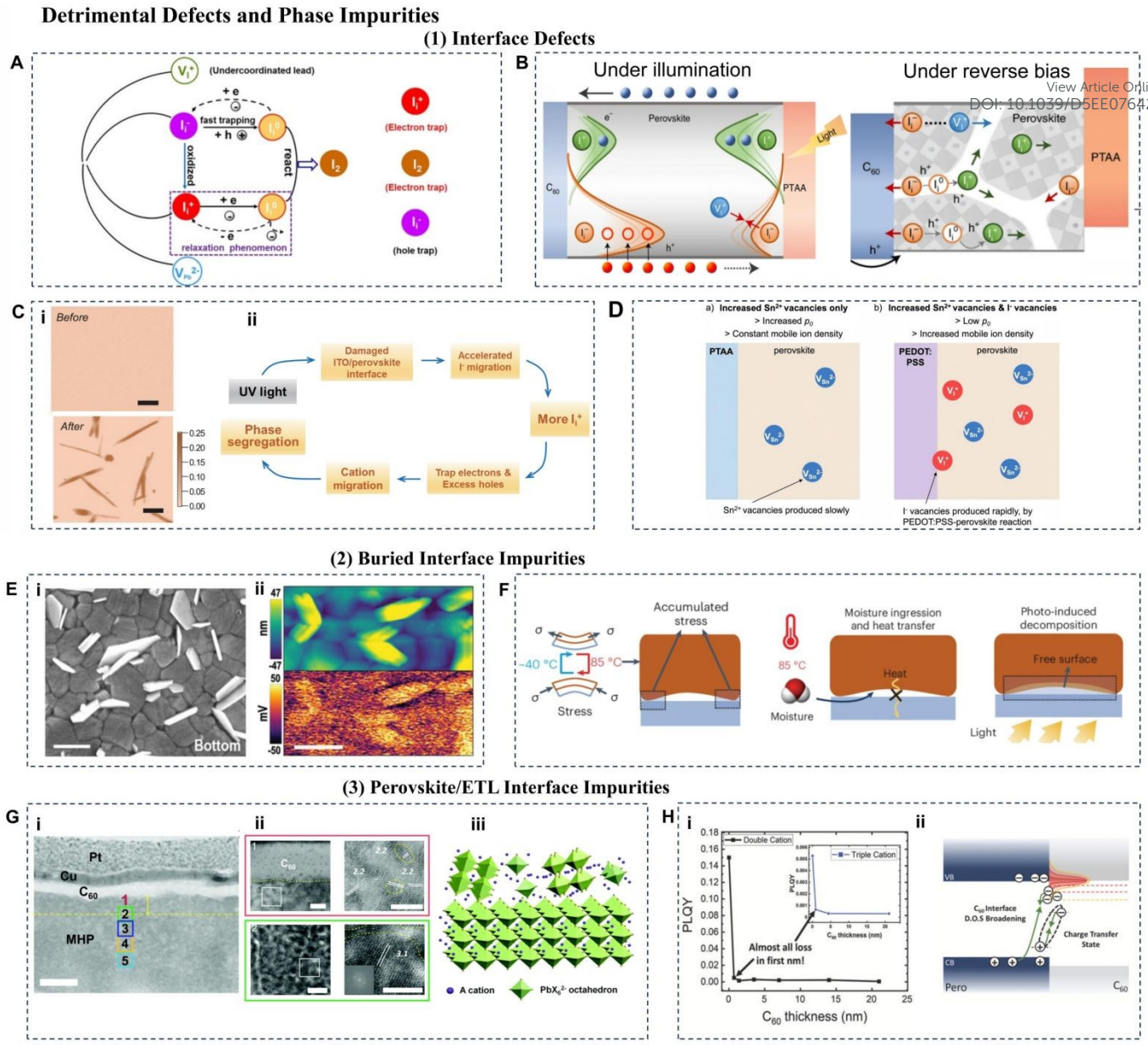

Figure 5. Detrimental Defects and Phase Impurities. (A) Schematic diagram of iodide interstitials evolution.[167] Copyright 2023, Wiley-VCH. (B) Schematic of the generation of iodide interstitials in devices under illumination (left), and the degradation processes in devices under reverse bias (right).[156] Copyright 2022, Nature Publishing Group. (C) (Ci) XRF mapping of the Cs/I ratio (right) of the PTAA-based perovskite films before and after LEP lamp illumination for ~100 hours. (Cii) Schematic degradation process of perovskite under light illumination with strong UV light.[157] Copyright 2024, Science Press. (D) Interface defect (V_{Sn} and V_I) change of devices using PTAA and PEDOT:PSS.[158] Copyright 2025, Nature Publishing Group. (E) (Ei) SEM images of bottom sides of the perovskite films. (Eii) AFM image (top panel), and corresponding KPFM image (bottom panel) of the bottom side.[161] Copyright 2021, Wiley-VCH. (F) Schematic illustration of the strain evolution in a perovskite film during -40 °C to 85 °C thermal cycling (left), damp heat test (middle), photothermal decomposition (right) with GSCs.[162] Copyright 2024, Nature Publishing Group. (G) (Gi) Cross-sectional TEM image of a device with a structure of ITO/PTAA/$MAPbI_3$/C_{60}/BCP/Cu. (Gii) HRTEM images of $MAPbI_3$ at positions 1. (Giii) Schematic illustration of the nanocrystals and amorphous phase at the top surface of MHP polycrystalline films.[165] Copyright 2021, Royal Society of Chemistry. (H) (Hi) PLQY versus C_{60} thickness for a double cation perovskite, and triple cation perovskite (inset), showing that the PL emission is quenched within the first few nm of C_{60} indicating the importance of recombination directly across the interface. (Hii) Final proposed mechanism and causes of C_{60} induced nonradiative losses showing increased nonradiative recombination either via a charge transfer state or low lying C_{60} states at the interface due to D.O.S broadening.[166] Copyright 2021, Wiley-VCH.

2.2.3 Ion Migration and Accumulation

(1) Ion Accumulation at the Perovskite/CTL Interface

As reported, the diffusion coefficient of migrating ions in the p-i-n structure is three orders of magnitude higher than in the n-i-p cells, leading to different accumulation rates of ions near the interfaces.[168] Driven by the electric field, positively charged defects (e.g., V_I and MA_i) and negatively charged defects (e.g., V_{MA} and I_i) migrate toward the HTL and ETL interfaces, respectively. The ion accumulation results in field screening that weakens the built-in potential, impedes efficient charge extraction, and promotes further the ion migration and defects formation. Over time, these defects increase nonradiative recombination and trigger chemical degradation at the interfaces. Additionally, mismatched band alignment between the perovskite and the adjacent CTL can exacerbate the ion accumulation at the perovskite/CTL heterointerfaces.

This challenge becomes particularly acute in mixed halide perovskite based inverted PSCs, serving as the sub-cells of perovskite based TSCs. Our group revealed that inefficient charge extraction within devices leads to carrier trapping at iodide interstitials, exacerbating the formation of I_2 and thus promoting the halide segregation.[169] Tan et al. systematically studied the photostability of devices under MPPT and open-circuit (OC) conditions (**Figure 6A**). They found that devices under OC conditions showed more severe degradation than those under MPPT, with the difference in degradation rates being more pronounced in wide-band gap (WBG, 1.68 and 1.78 eV) PSCs compared with mid-gap PSCs. This is attributed to charge accumulation accelerating halide segregation under illumination, due to the mismatched energy level and high trap density at the perovskite/C_{60} heterointerface.[170]

Further insights by Wolf et al. reveal that valence band maximum (VBM) offsets and energy barriers at the HTL/perovskite interface affect the charge accumulation, which exacerbates halide segregation and deteriorate operational stability of WBG PSCs (1.69, 1.81, and 2.00 eV) (**Figure 6B**).[81] Energy barriers cause holes to accumulate, drawing in anions, while VBM offsets lead to electron buildup, attracting cations. With well-aligned VBM levels, ion accumulation and halide segregation are minimized, thereby enhancing the operational stability of devices. These findings highlight the design of heterointerfaces that facilitate charge extraction and maintain durable interfacial contact.

(2) A-site Cation Diffusion at 2D/3D Perovskite Heterojunction Interface

Two-dimensional (2D) perovskites have emerged as effective passivation layers at the perovskite/ETL interface, significantly mitigating non-radiative recombination, suppressing ions migration, and enhancing interfacial stability.[171, 172] Despite substantial advancements in device operational longevity enabled by 2D/3D perovskite heterostructures, fundamental challenges persist, such as the complex ionic dynamics nature. In particular, A-site cation diffusion between the surface 2D perovskite layer and the underlying 3D bulk can trigger dimensional transformations under thermal, light, and bias stress, which would lead to interface reconstruction and loss of initial properties.[140, 173-176]

Perini and co-workers reported accelerated degradation in 2D/3D PSCs based on (CsMAFA)$Pb(I,Br)_3$ treated with PEAI and octylammonium bromide (OABr), compared to untreated devices.[176] The stability tests were conducted under inert atmosphere, 1 sun illumination, and at 55°C for 1000 hours. The reduced stability was attributed to ion migration at the 2D/3D interface during thermal annealing and device operation, leading to increased halide heterogeneity, particularly on PEAI-treated surfaces (**Figure 6C**). Similarly, Sutanto et al. reported that prolonged thermal annealing (50°C for >2 hours) of 2D/3D perovskites based on 2-thiophene methylammonium iodide (TMAI) on (CsMAFA)$Pb(I,Br)_3$ induces continuous 2D-phase structural evolution, with a gradual shift toward high-n phases ($n \geq 2$) and overall phase degradation.[140] Consistently, as shown in **Figure 6D**, atomic force microscopy-based infrared spectroscopy (AFM-IR) and X-ray photoelectron spectroscopy (XPS) spectra reveal a pronounced increase in FA^+ signals on the surface of the PEAI-based 3D/2D perovskite heterostructure after thermal aging (100°C, 120 minutes).[174] This observation indicates upward diffusion of FA^+ ions and a transformation of the 2D perovskite into a more 3D-like phase, thereby compromising the structural and electronic advantages of the 2D interlayer. Collectively, these results highlight that ion migration-induced interfacial and structural instability plays a critical role in the degradation of 2D/3D hetero-interface, underscoring the importance of maintaining the structural integrity of the 2D capping layer for long-term operational stability.

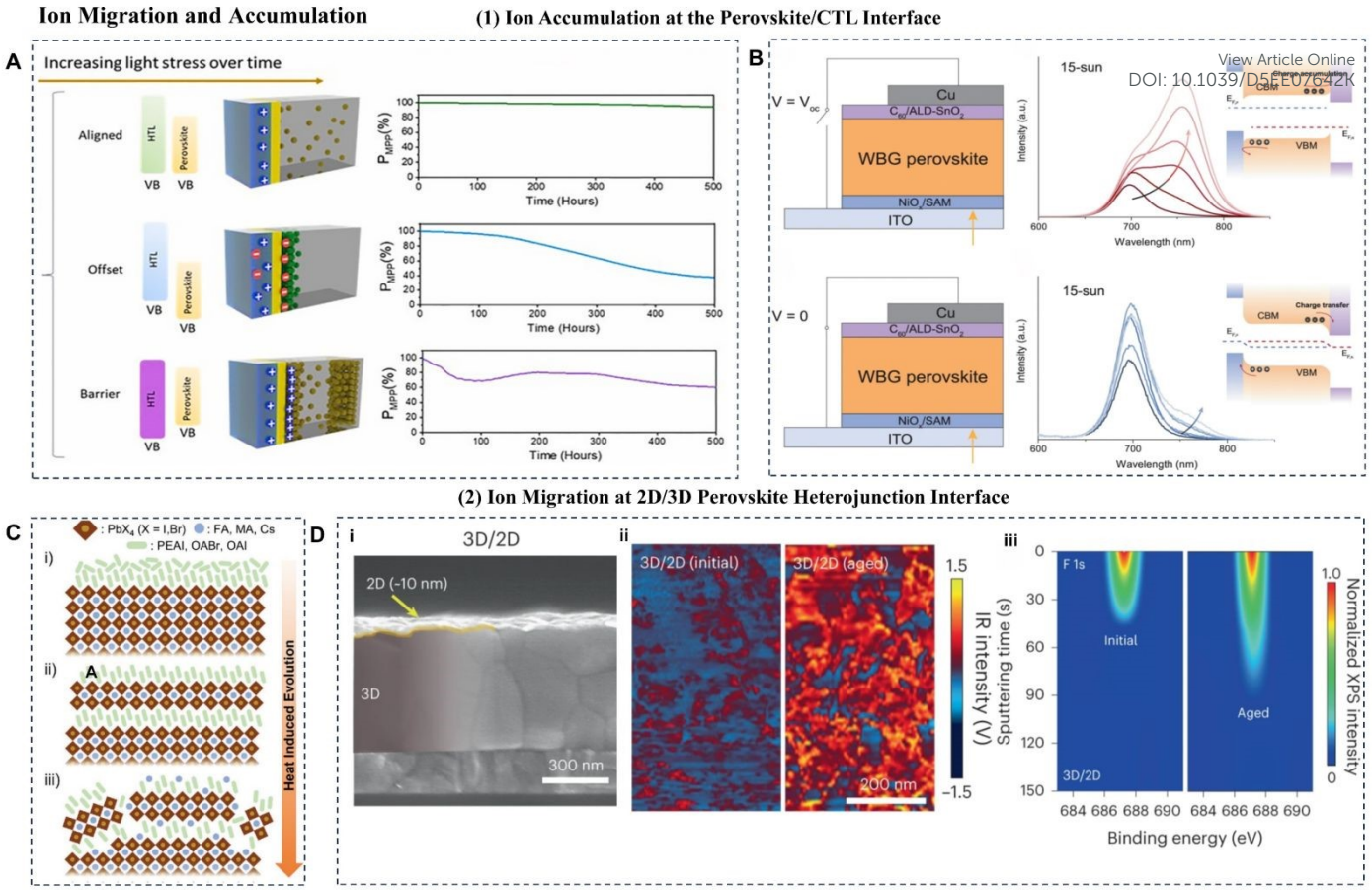

Figure 6. Ion Accumulation and Migration. (A) Minimalistic scheme of charge density and mobile ions under light stress at the HTL/perovskite interface when their VBMs are aligned, in offset or in barrier, and smoothed normalized MPPT of 1.69 eV devices under AM1.5G.[81] Copyright 2024, Cell Press. (B) PL spectra of 1.77 eV devices for photostability study under open-circuit and short-circuit conditions.[170] Copyright 2023, Nature Publishing Group. (C) Schematics of the evolution of the interface treated with bulky cations upon annealing: i) Formation of an organic overlayer; ii) bulky cation diffusion and RP phase formation; iii) RP reconstruction.[176] Copyright 2022, Wiley-VCH. (D) (Di) Cross-sectional SEM images of 3D/2D perovskite heterostructures. (Dii) AFM-IR (recorded at 1712 cm^{-1} corresponding to the symmetric $C{=}NH_2^+$ bending of FA^+) images of 3D/2D perovskite heterostructures before and after ageing at 100°C for 120 minutes. (Diii) XPS depth profiling of 3D/2D perovskite heterostructures before and after ageing.[174] Copyright 2023, Nature Publishing Group.

2.2.4 Interfacial Stress and Mechanical Delamination

Strain has emerged as a critical factor influencing the structural and chemical stability of perovskite materials across multiple length scales. At the macroscale, residual stress is frequently introduced during thermal annealing due to higher coefficients of thermal expansion of the perovskite compared with underlying charge transport layers (e.g., HTL in p-i-n structures) (**Figure 7A**).[177] Perovskite layers are inherently prone to volumetric expansion, which induces tensile strain that is highly concentrated at the interfaces. For one thing, the tensile strain drives vacancy formation, promotes halide segregation, accelerates ion migration and phase transitions, ultimately resulting in perovskite decomposition when exposed to external stress.[177 178] For example, in $FAPbI_3$ and $FA_{0.75}Cs_{0.25}PbI_3$, strain has been shown to convert shallow iodide vacancy (V_I) defects into deep-level states.[179] For another, the interface serves as a mechanical weak point while interfacial stresses can cause the interfacial delamination, especially during thermal cycling **(Figure 7B and 7C)**. For inverted PSCs, interface delamination is further aggravated when perovskite films are deposited on hydrophobic layers such as PTAA due to weak interfacial adhesion.[76] For flexible inverted PSCs, beyond cracking and delamination, mechanical deformation can also induce buckling and wrinkling within the perovskite layer, creating localized regions of high strain that further amplify the risk of mechanical breakdown.[180]

Mechanical robustness has been identified as a central obstacle to the commercialization of PSCs, and much of this

vulnerability stems from the use of fullerene-based ETLs. Fullerenes such as C_{60} and PCBM are characterized by weak intramolecular cohesion and poor interfacial adhesion to neighboring layers, owing to their van der Waals-dominated interactions.[98, 99] This renders them susceptible to both interfacial delamination at the perovskite and metal electrode interfaces and cohesive fracture within the fullerene layer itself, consistent with their low intermolecular bonding energy (~0.44 eV). Rolston and colleagues investigated the interfacial adhesive fracture energy (G_c) of inverted PSCs and found that cracks predominantly propagated cohesively within the charge transport layers, particularly the C_{60} layer, highlighting it as a mechanically vulnerable component in the p-i-n architecture.[98] Notably, the interface between C_{60} and tin oxide (SnO_x) in tandem devices exhibits exceptionally low fracture energy, facilitating delamination and crack propagation. This fragility becomes even more problematic during module integration processes, such as cell cutting, interconnection, and vacuum lamination.[181, 182] In tandem photovoltaic architectures incorporating PSCs, the accumulation of internal stress due to multilayer stacking further amplifies the risk of mechanical failure. As shown in **Figure 7D**, fullerene-related delamination has been observed under the electron microscopy in small-area laboratory cells and at the macroscopic scale during outdoor testing of perovskite modules, highlighting fullerene fragility as a critical challenge for scaling perovskite photovoltaics.[99] Given these considerations, interfacial delamination represents a non-negligible reliability concern, and all layers and interfaces in PSCs must therefore comply with IEC 61646 standard qualification protocols (200 cycles from -40 to 85℃). Developing interfaces with high G_c is essential to resist crack propagation and delamination under stresses imposed during fabrication and service.

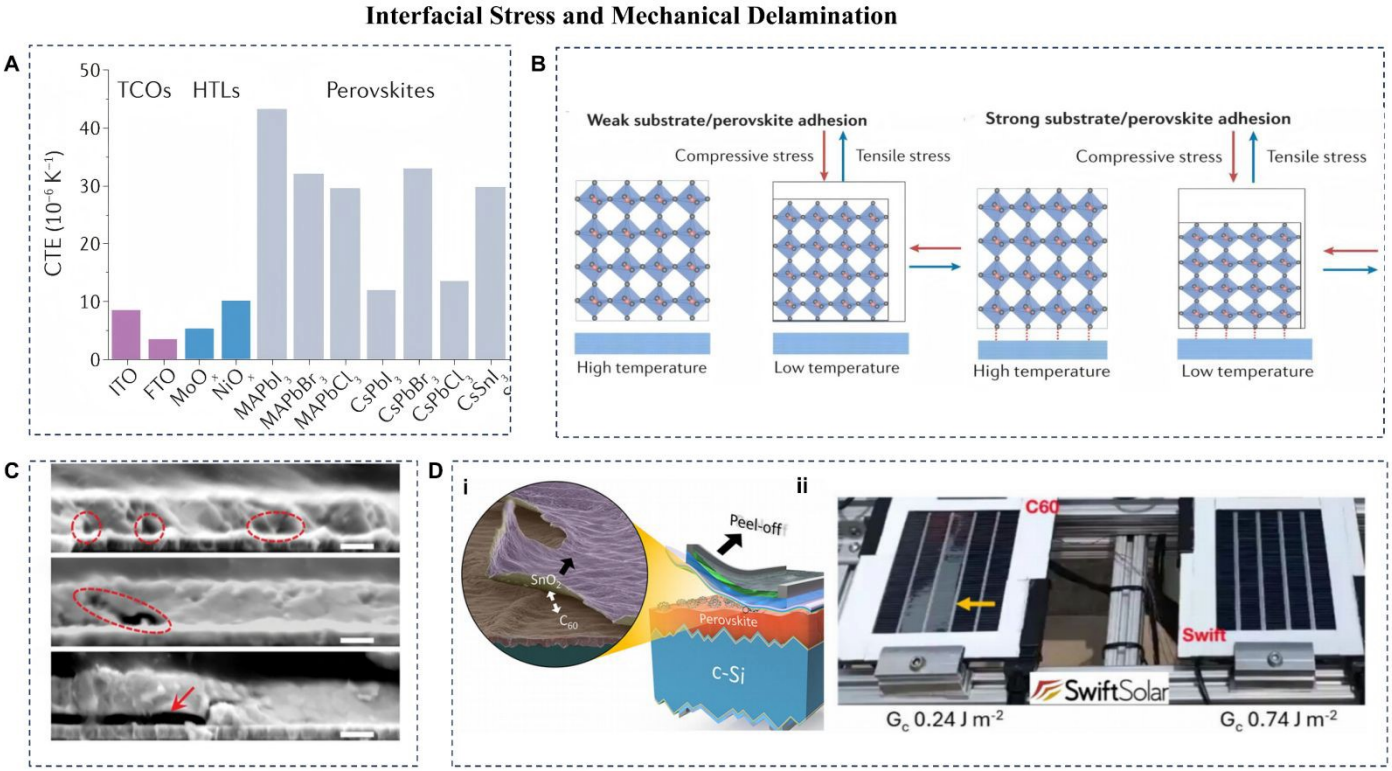

Figure 7. Interfacial Stress and Mechanical Delamination. (A) Coefficient of thermal expansion of commonly used TCOs, perovskites and metaloxide-based ETLs and HTLs. (B) Illustration of the formation of compressive and tensile stresses in perovskite films with weak and strong substrate adhesion.[76] Copyright 2023, Nature Publishing Group. (C) Cross-sectional SEM images of the PSC without SAMs tested for 757 hours showing morphological degradation at the ETL/MHP interface.[70] Copyright 2021, Science Press. (D) Fullerene-related delamination. (Di) Scanning electron microscope image demonstrating delamination between C_{60} and SnO_x.[182] Copyright 2022, American Chemical Society. (Dii) Photograph of modules under outdoor test at NREL with C_{60} and a proprietary, fullerene-free ETL.[99] Copyright 2025, American Chemical Society.

3. Interface Engineering Driven Stability Strategies

The current interface engineering includes: (i) Surface treatment through modulating the properties of perovskite such as defect activity and surface energy-level. (ii) Specifically designed interface materials for stability enhancement of perovskite absorber and interface.

3.1 Controllable Surface Reconstruction

3.1.1 Target Surface Passivation

Activities of iodide interstitials (I_i) deteriorate device stability, as discussed above. The feasibility of I_i formation correlates with the dissociation energy of I^- from the perovskite lattice. Indeed, Huang and co-workers found that the surface I^- binding energy on the perovskite termination surface is strengthened by Cd^{2+}, which is introduced by surface CdI_2 treatment.[183] This effectively increases the defect formation energy of I_i and iodine vacancy (V_I) and thus their density, contributing to greatly improved device stability. The product of I_2, as result of the defect activities of I_i can initiate a series of instabilities in the perovskite. Therefore, preventing the reaction between I_2 and perovskite represents another category of effective strategies to improve device stability. Yuan and co-workers introduced perfluorododecyl iodide with strong affinity for I_2 into the perovskite, which preferentially captures the formed I_2 before it damages the perovskite (**Figure 8A**).[94] As a result, the UV irradiation and thermo-photostability of devices have been improved by more than tenfold, and the reverse bias stability improved by 1,000 times.

However, this strategy may encounter problems during the long-term operation of devices, as the additive could be saturated with formed I_2. Pointing at this issue, anthraquinone (AQ) additive, acting as a redox shuttle, convert I_2 back to I^- upon formation, greatly improving the operational stability of WBG (1.81 eV) PSCs (T_{95} of 500 hours under MPPT, ISOS-L-1), and perovskite/organic TSCs (T_{92} of 500 hours under MPPT, ISOS-L-1).[184] Similarly, Ge at al. introduced a multifunctional dye molecule (D358) that facilitates the reduction of I_2 to I^- and the oxidation of Pb^0 to Pb^{2+}, thereby effectively suppressing halide phase segregation.[185] The resultant WBG (1.77 eV) based devices retained 82.9% of their initial PCE, while all-perovskite TSCs preserved 86.9% after 1,000 hours of MPPT (ISOS-L-1I). These highlight the critical role of redox-mediated electron shuttling in mitigating halide segregation in WBG perovskite.

B-site metal cations can undergo redox reactions under harsh aging conditions. In particular, Pb^{2+} can be reduced to metallic Pb^0 under heat or illumination.[186] The formation of Pb^0 introduces deep-level defect states that severely deteriorate both the performance and operational stability of PSCs. Passivating undercoordinated Pb^{2+} defects via Lewis base coordination, analogous to V_I passivation, has proven effective in enhancing device stability, and a wide range of Lewis base molecules have been developed for this purpose.[8, 10, 61, 187-190] Liu et al. introduced a bimolecular passivation approach by combining sulfur-functionalized methylthio molecules and diammonium species.[8] The former effectively passivate undercoordinated Pb^{2+} ions by robust coordination (Pb-S bonds) and hydrogen bonding, while the latter enables field-effect passivation by electrostatically repelling minority carriers at the contact interface. This dual-passivation strategy resulted in remarkable operational stability, with devices retaining performance for over 2,000 hours at 65°C under ambient air. However, it was then identified that the formation of densely packed, electrically resistive passivation layers perpendicular to the surface can hinder efficient charge extraction, thus limiting the fill factor of inverted devices. To address this, they proposed a dual-site-binding with two neighboring Pb^{2+} defect sites (Pb-O and Pb-Cl bonds) in a planar ligand orientation by 4-chlorobenzenesulfonate (4Cl-BZS). (**Figure 8B**).[10] The devices achieved a T_{95} of 1,200 hours under MPPT at 65°C, underscoring the synergistic benefits of multi-functional ligand design. Based on the study of iodide chemistry related to perovskite stability, research in our group has shown that passivation of undercoordinated Pb defects can suppress the formation of detrimental I_2 , which serves as a defect reservoir, using tri-n-octylphosphine oxide (TOPO) or polyethylene oxide (PEO).[126] This study further underscores the critical importance of pinpointing the defects that most strongly impact light and thermal stability, and achieving precise passivation of these defects to further improve the stability of inverted PSCs.

Undercoordinated Pb^{2+} defects can be effectively passivated through π-π interactions, and host-guest chemistry with supramolecular agents[191-195]. Moreover, the formation of protective layers can shield the perovskite from environmental stressors, such as moisture and oxygen, thereby improving long-term device stability. A representative example is crown ethers[195-197], which form host-guest complexes with dangling Pb^{2+} ions, suppressing the formation of metallic Pb^0 on the surface of FA-rich perovskite films, reducing defect densities and suppressing ion migration. In addition, porphyrin[198-200] and heterocyclic aromatic compound[191, 201, 202] introduce π-π stacking, forming ordered networks to restrict undesirable molecular rearrangements that can lead to degradation under external stress. For instance, a molecular bridge based on 2, 4, 6-tris(4-aminophenyl)-s-triazine (TAPT) was introduced to link PTAA and the

perovskite.[172] The amino groups form H-π interactions with PTAA, while the triazine core coordinates with Pb^{2+} by π-Pb^{2+} interactions, enabling efficient interfacial passivation. This dual interaction stabilizes the interface, suppressing nonradiative recombination and ion migration, and significantly improves device stability, with the device retaining 89.7% of its initial efficiency after 1,500 hours of MPPT and 91.9% after 1,065 hours at 85°C.

View Article Online
DOI: 10.1039/D5EE07642K

On the other hand, the surface energy level of the perovskite absorber plays a decisive role in determining band alignment and electron extraction at the perovskite/C_{60} interface, which is often hindered by significant energy mismatches and large electron transfer barriers. Ion and defect accumulation at this interface further undermines interfacial stability, as discussed in section 2.2.3. Therefore, defect modulation has therefore emerged as an effective strategy to tune surface energy levels and improve charge extraction. Building on this concept, a range of defect-modulation approaches have been developed to facilitate interfacial charge extraction while simultaneously improving stability.[6, 203-205] For instance, facilitating the V_I formation at the perovskite surface induces n-type doping near the contact with C_{60}, thereby lowering the extraction barrier and improving the device stability.[6] Additionally, 1,4-butanediamine surface treatment eliminates nonstoichiometric p-type defects caused by intrinsically lead deficiency at the $CsPbI_3$ surface, thereby enabling more efficient electron extraction and enhanced long-term device stability.[204] These advancements underscore the pivotal role of tailoring surface defect chemistry in governing interfacial quality and, consequently achieving precise passivation of these defects to further improve the stability of inverted PSCs.

3.1.2 Surface Polishing

Perovskite surface polishing using physical or chemical approaches has been demonstrated to effectively remove surface defects. Huang et al. found that defective surface regions exhibit weaker mechanical strength compared to the crystalline regions, allowing them to be selectively peeled away using adhesive tape (**Figure 8C**).[206] The enhanced photoluminescence intensity following mechanical polishing suggests suppressed nonradiative recombination due to the elimination of defective surfaces. Consequently, tape-treated devices maintained 97.1% of their initial efficiency after 1,440 hours of light soaking (65°C, ISOS-L-2). Wet polishing by employing nanoscale abrasives suspended in a liquid medium, has also been developed to polish the perovskite surface. This technique offers advantages of minimizing friction between the perovskite surface and the polishing interface and facilitates the efficient removal of abraded perovskite during the polishing, thereby mitigating surface scratching and enhancing the reproducibility. For example, nano-polishing with an Al_2O_3/anisole dispersion of WBG perovskite (1.67 eV) removed the defect-rich crystal surface while simultaneously passivating the newly exposed high-crystallinity surface with anisole (**Figure 8D,** Effect I).[207] Elimination of the defective surface layer suppresses defect-assisted ion migration and thus halide segregation (Effect II). Furthermore, the surface layer commonly has mismatched lattice with the bulk regions; and thus, surface nano polishing helps to mitigate crystallinity inhomogeneity across the perovskite film and relieve residual strain (Effect III). Additionally, nano-polishing preferentially removes defective I-rich species and leaves the surface to be Br-rich, due to the stronger binding energy of Br^- than I^-. The Br-rich phase could prevent the trapping of photogenerated charge carriers in the grain bulk by forming a type-I heterojunction, which suppresses instability and energy loss initiated by defect activities largely from the perovskite surface (Effect IV). The treated WBG perovskite-based devices retained 80% of its initial efficiency after 1,505 hours of MPPT under 1-sun illumination.

The surface polishing strategy also has effect on enhancing the stability of Sn-based inverted PSCs. Zhou et al. proposed a chemo-thermal surface de-doping strategy that substantially reduces Sn (IV) self-dopants on the surface of Sn-based perovskites, thereby improving device stability.[208] Building on this concept, a surface reconstruction strategy was further developed by combining 6-maleimidohexanehydrazide trifluoroacetate (MHATFA) and isopropanol to post-treat $FASnI_3$ films.[209] The strongly electron-withdrawing trifluoromethyl ($-CF_3$) moiety in MHATFA interacts with the polar hydroxyl (-OH) groups of isopropanol solvent which otherwise damage the perovskite layer, effectively polishing the defective surface. The surface refinement enhances structural uniformity and defect mitigation, enabling devices to retain over 75% of their initial PCE after 1,000 hours of continuous illumination. Extending this concept to Sn-Pb perovskites, Chen and co-workers reported a surface reconstruction strategy employing a surface polishing agent, 1,4-butanediamine (BDA), combined with a surface passivator, $EDAI_2$, which effectively eliminates Sn-related defects (Sn^{4+}) and passivates organic cation vacancies (V_A) and V_I at the surface of Sn-Pb perovskite films.[210] The all-perovskite TSCs

retained 79.7% of their initial PCE after 550 hours operated at MPPT in ambient air.

3.1.3 Surface Sulfidation

Treating the perovskite surface with sulfur-containing species induces the formation of compounds such as $PbSO_4$ or PbS through reactions with surface Pb atoms, which mitigates ion migration and fortifies the uppermost layer of the perovskite film. The strong bonding between the inorganic layer and the perovskite surface yields a mechanically durable coating. Fang and co-workers found that a stable perovskite heterojunction was formed by sulfidation of surface Pb-rich perovskite films through pyridine-2-carboxylic lead ($PbPyA_2$), and the formed PbS reinforces the underlying perovskite structures (**Figure 8E**).[211] Devices with surface sulfidation retained over 90% of their initial efficiency for 2,200 hours after thermal aging at 85°C, or after 1,000 hours of MPPT at 55±5°C. Huang and co-workers demonstrated that transforming lead halide perovskite surfaces into water-insoluble lead(II) oxysalts via sulfate ($APbX_3 + SO_4^{2-} \rightarrow A^+ + 3X^- + PbSO_4$) or phosphate ion ($3APbX_3 + 2PO_4^{3-} \rightarrow 3A^+ + 9X^- + Pb_3(PO_4)_2$) treatment markedly enhances the stability of the perovskite film.[212] The resultant devices maintained 96.8% of their initial PCE after 1,000 hours operated at MPPT (65°C).

View Article Online
DOI: 10.1039/D5EE07642K

3.1.4 Amine Condensation Surface Reaction

An alternative approach involves leveraging the protonation reaction between the amine groups of surface-treatment salts and the FA^+ cations of the perovskite. Jiang et al. post-treated the perovskite surface with 3-(aminomethyl)pyridine (3-APy) molecule which selectively reacts with FA^+ ions.[6] The reaction products ($MPyFA^+$) achieve the polishing effect, leading to a perovskite surface with a more homogeneous potential. Meanwhile, the reduced formation energy of V_I induce the n-type surface doping, which is beneficial for interfacial electron extraction (**Figure 8F**). The resultant devices maintained 87% of their initial efficiency after more than 2,400 hours of operation at ~55°C in air.

The protonated amine can also interact with halide-related defects. Xu et al. compared various configurations and protonation states within the polyethylenimine (PEI) family as a proof of concept.[213] In addition to the conventional physisorption and metal-chelation mechanisms, they identified a novel interaction mode between perovskite and PEI, an in-situ protonation process. The protonation from $-NH_2$ to $-NH_3^+$ enables stronger interfacial bonding with I^- ions of perovskite and promotes the ordering of the $R-NH_3^+$ branches for more effective passivation. This process effectively suppresses surface I_i defects and outperforms conventional ex-situ protonated and non-protonated amino groups ($-NH_2$). The cells exhibit no degradation during accelerated aging tests at 85°C for >1,000 hours and operating at MPP for > 1,000 hours (ISOS-L-1).

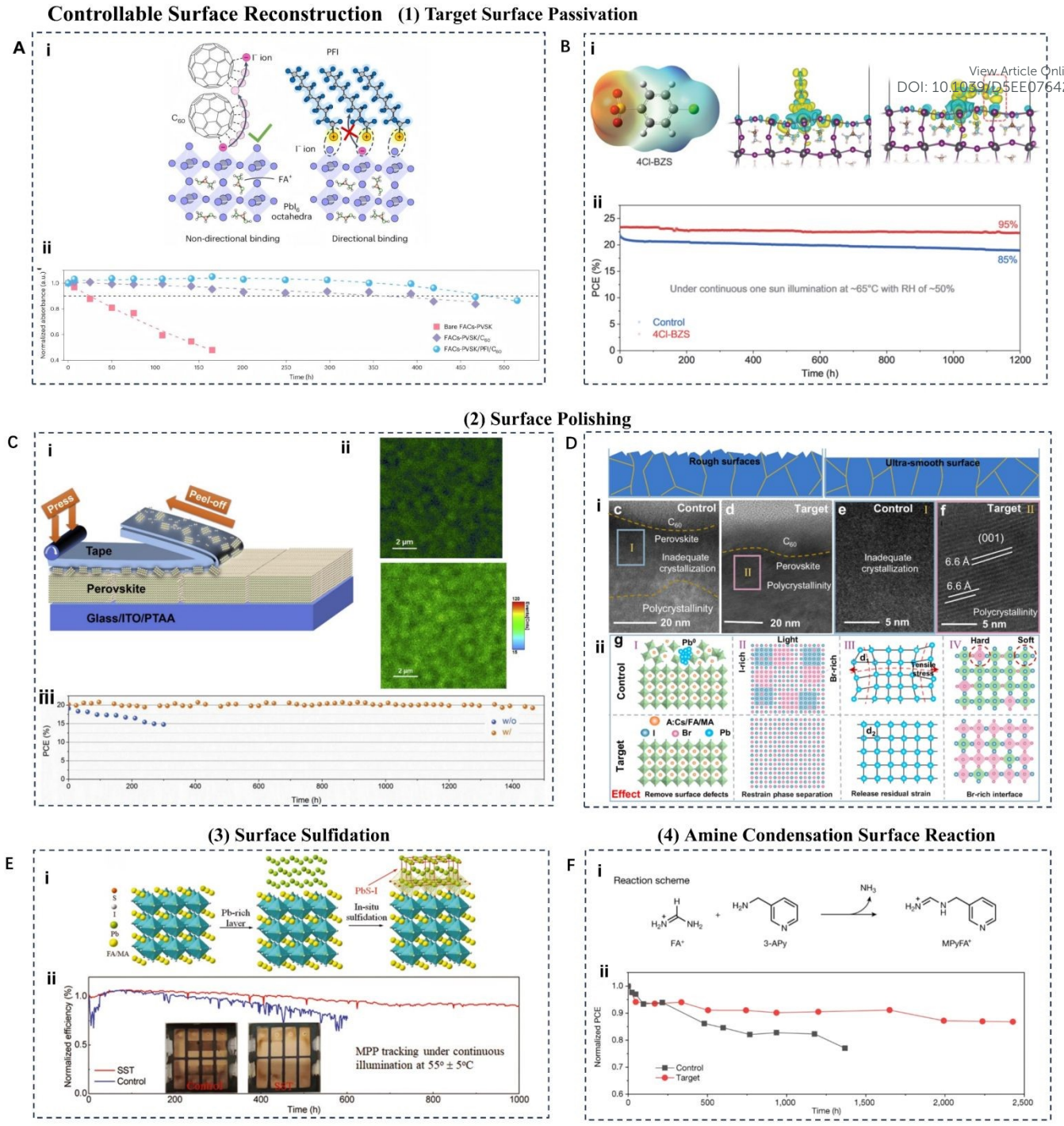

Figure 8. **Controllable Surface Reconstruction**. (A) (Ai) Illustration of C_{60} with non-directional iodine affinity and PFI with directional iodine affinity, respectively. (Aii) Absorption reduction (at 600 nm) of FACs-PVK, FACs-PVK/C_{60} and FACs-PVK/PFI/C_{60} films (without extrinsic I_2) under ultraviolet light exposure (395 nm, 60 mW·cm^{-2}) at 85°C.[94] Copyright 2024, Nature Publishing Group. (B) (Bi) Structure and electrostatic potential of 4Cl-BZS ligands (left), atomic structures of ligand adsorbed in a perpendicular orientation (middle), a planar or parallel orientation (right) on perovskite surface. (Bii) MPPT of encapsulated devices under simulated 1-sun illumination (50% RH, 65°C).[10] Copyright 2024, Science Press. (C) (Ci) Schematic of peeling an adhesive tape off a $MAPbI_3$ film. (Cii) PL mapping of a $MAPbI_3$ film before (top) and after (bottom) tape treatment. (Ciii) Operational stability of encapsulated devices.[206] Copyright 2020, Cell Press. (D) (Di) Cross-sectional TEM images of the device. (Dii) Schematic diagram of the changes in perovskite film before and after nano-polishing treatment.[207] Copyright 2024, Nature Publishing Group. (E) (Ei) Schematic diagram of a surface sulfidation treatment. (Eii) MPPT of devices at 55±5°C. The inset shows photographs of PSCs after MPPT.[211] Copyright 2022, Science Press. (F) (Fi) Condensation reaction scheme of FA^+ and 3-APy. (Fii) MPPT of devices under 1-sun illumination at 55±2°C in air (40-60% RH).[6] Copyright 2022, Science Press.

Table 1. Stability development of single-junction and tandem solar cells by controllable surface reconstruction.

Year	Strategy	PCE (certified)	Stability Improvement Mechanism	Stability for devices	
				Operation	Thermal/Light/Humidity
Single-junction PSCs					
2022	(Aminomethyl)pyridine (3-APy)[6]	25.49	Selective reaction with FA^+ for smoothing surface, promotes V_I-induced n-type surface doping	T_{87}~2,428 h (55°C); T_{90}~1315 h (ISOS-L-2I; 65°C)	T_{94}~850 h (ISOS-D-3; 85°C, 85% RH)
2022	Polyethylenimine (PEI)[213]	24.3	In-situ protonation of PEIE reduce the deep-level I_i defects	T_{100}~1,100 h (35~40°C)	T_{100}~1,100 h
2022	Pyridine-2-carboxylic lead (PbPyA2)[211]	24.3	Surface sulfidation (Pb-S bonding), induces n-N back-surface field	$T_{90.5}$~1,000 h (55°± 5°C)	$T_{91.8}$~2,200 h (85°C)
2023	Fluorinated aniliniums (345FAn)[9]	(24.09)	Minimize reactivity with perovskites for more effective passivation	T_{85}~1,560 h (ISOS-L-3)	/
2024	Dual-site-binding ligands (4Cl-BZS)[10]	26.9 (26.15)	Bind two neighboring Pb^{2+} defect in planar ligand orientation	T_{95}~1,200 h (65°C, 50% RH); T_{87}~540 h (85°C)	T_{95}>1,500 h (85°C)
2024	Bimolecular passivation ($PDAI_2$/3MTPAI)[8]	26.4 (25.1)	Chemical and field-effect passivation	T_{96}~2,000 h (ISOS-L-3; 65°C, 50% RH)	T_{95}>1,600 h (ISOS-D-2I; 85°C)
2024	Ligands amidination (4FBII)[11]	26.7 (26.28)	Resists deprotonation under elevated temperature	T_{90}~1,130 h (ISOS-L-2; 65°C)	/
Perovskite/Si Tandem Solar Cells					
2024	Dynamic spray-coating fluorinated thiophene -thylammonium (CF_3-TFA)[214]	30.89	Passivates defects (V_A, I_{Pb}, I_A), reconfigures interfacial electronic structure	T_{97}~600 h (Air)	/
2025	Cage-like diammonium chloride (DCl)[215]	31.1	Induces phase-pure quasi-2D perovskite with spontaneous in-plane orientation and strong ferroelectricity	$T_{91.4}$>792 h (N_2)	/
All-Perovskite Tandem Solar Cells					
2024	1,4-butanediamine (BDA) and $EDAI_2$ (NBG)[210]	28.80 (28.49)	Surface polishing to eliminate Sn^{4+} defects and passivate V_A/V_I	$T_{79.7}$~550 h (30-40% RH)	/
2025	Organics dyes (D358) (WBG)[185]	28.83	Reduce I_2 to I^-, oxidize Pb^0 to Pb^{2+}	$T_{82.9}$~1,000 h (ISOS-L-1I)	/

3.2 Constructing Robust Multi-Layered Interface

3.2.1 Functionalized Materials at the Perovskite/ETL Interface

Functionalized interfacial materials have been widely employed to regulate the chemical and electronic environment at perovskite interfaces. At molecular level, these materials can passivate under-coordinated surface defects, optimize interfacial band alignment, and suppress ion migration pathways. Organic ammonium layers are commonly used at both hole- and electron-selective interfaces to enable high-efficiency PSCs; however, their limited photothermal stability often compromises long-term device operation. Therefore, developing more robust organic functional layers or incorporating inorganic interfacial materials has emerged as an effective strategy to improve the operational stability of inverted PSCs.

Some inorganic salts can react with the perovskite surface to enhance carrier extraction while acting as a buffer layer that prevents the ingression of moisture, oxygen, and other harmful species. In one example, an ultrathin magnesium fluoride (MgF_x) interlayer at the perovskite/C_{60} interface not only mitigates gap state-assisted recombination caused by C_{60}, but also promotes favorable band alignment for efficient electron extraction.[96] The resulting perovskite-

silicon TSCs retained approximately 95% of its initial efficiency after 1,000 hours following damp-heat testing (85°C, 85% RH; ISOS-D-3). More recently, ALD-Hafnium oxide (HfO_x) interlayers stabilize double interfaces under operational stress **(Figure 9A)**.[13] At the NiO_x/SAM interface, a hydroxyl-rich, Lewis-acidic n-HfO_x layer promotes tridentate phosphonic acid coordination, improving SAM retention and thermal stability. At the perovskite/C_{60} interface, a p-HfO_x layer anchors 3-fluorophenylethylammonium iodide (3F-PEAI) through Hf···F interactions while serving as a barrier against I^- and Ag^+ ions diffusion. As a result, the devices achieved a PCE of 27.1% (26.6% certified) and retained over 90% of their initial efficiency after 5,000 hours of MPPT in ambient air (85°C, 50% RH; ISOS-L-3). This inorganic oxide-constrained architecture offers a promising pathway toward achieving the decades-long operational lifetimes required for the real-world deployment of perovskite modules.

By leveraging the unique characteristics of inorganic 2D monolayers, including dangling-bond-free surfaces, atomic thickness, and continuous planar morphology, enables efficient and stable PSCs and establishes a versatile platform for heterojunction engineering between 2D materials and soft-lattice optoelectronic materials. Along this line, Zhou and co-workers introduced wafer-scale TMDC monolayers (e.g., MoS_2 and WS_2, atomic thickness, < 1 nm) at perovskite interface, which form strong interfacial Pb-S bonding to passivate defects and stabilize α-$FAPbI_3$, act as an effective barriers against ion migration and environmental ingress, and block the minority carriers through a type-I band alignment (**Figure 9B**).[12] The inverted PSCs with a MoS_2/$FAPbI_3$/MoS_2 structure demonstrated a T_{95} lifetime exceeding 1,200 hours under the damp-heat test (85°C, 85% RH; ISOS-D-3), and showed almost no efficiency loss after 2,000 hours of MPPT. The device also exhibited excellent operational stability at high temperatures, maintaining over 96% of its initial efficiency after 1,200 hours of MPPT at 85°C (ISOS-L-2).

Metal-organic compounds, particularly ferrocene (Fc)-based derivatives, have emerged as versatile interfacial modifiers in PSCs. These materials not only form chemical bonds to strengthen the perovskite lattice but also adjust electrical properties, such as surface work function and band alignment for facilitating electron extraction at the perovskite/ETL interface. An organometallic compound, ferrocenyl-bis-thiophene-2-carboxylate (FcTc2) functionalized the perovskite/C_{60} interface, which not only forms strong Pb-O coordination bonds to passivate surface trap states but also facilitates interfacial electron transfer through the electron-rich, delocalized ferrocene units.[216] The resultant devices retained over 98% of their initial efficiency after more than 1,500 hours of continuous illumination and demonstrated excellent stability under damp-heat conditions (85°C, 85% RH; ISOS-D-3), meeting the international standards for silicon solar cells (**Figure 9C**). Ferrocenyl tetraphenylporphyrin cobalt (FcTTPc), with inherent carboxylate and thiophene functionalities surrounding the central ferrocene motif, forms strong coordination interactions with the perovskite/PCBM interface through its conjugated framework and electron-rich sites.[217] The carboxylate (C=O) and thiophene (C-S) groups in FcTTPc interact strongly with undercoordinated Pb^{2+} ions, effectively passivating interfacial defects. Additionally, the thiophene moiety forms strong π-π interactions with ETL, promoting efficient interfacial electron transport. Consequently, devices retained 94% of their initial efficiency after 1,000 hours of MPPT (in N_2).

Dipole interlayers can passivate surface defects and modulate the electronic properties at the perovskite/C_{60} interface, thereby improving interfacial contact and stability through both chemical and field-effect passivation. These effects originate from changes in surface energy levels and work function induced by the intrinsic dipoles of the ligands and the interfacial dipoles formed upon binding to the perovskite surface.[218] Typical examples include commonly used post-treatment agents such as $EDAI_2$ and $PDAI_2$.[133, 210, 219-222] Their interaction with the perovskite surface increases the majority carrier concentration at the electron-selective contact, thereby reducing interfacial recombination. Meanwhile, the resulting field-effect passivation enhances electron concentration throughout the intrinsic perovskite absorber, improving conductivity and reducing carrier transport losses. Perovskite/silicon TSCs incorporating a PDAI dipole layer which increased the majority charge carriers and reduced interfacial recombination at the perovskite/C_{60} interface were further evaluated under outdoor stability conditions combined with damp-heat testing (85°C, 85% RH; ISOS-D-3) for 1,000 hours. The target devices exhibited improved resistance to FF and V_{oc} losses, retaining 83.4% of their initial PCE, compared with 73.7% for the control devices.[133] Li et al. also introduced sodium heptafluorobutyrate (SHF) to functionalize the electron-selective contact.[7] The SHF layer forms a hydrophobic barrier while passivating surface

defects. Its dipole moment induces carrier redistribution and adjusts the perovskite surface work function for facilitating electron extraction. During C_{60} deposition, SHF promotes dense and uniform C_{60} stacking, suppressing ion diffusion within the device. This regulation suppresses C_{60} aggregation on hydrophilic perovskite surface, ensuring uniform coverage and improved interfacial stability. The devices achieved a PCE of 27.02%, along with no degradation after 1,200 hours of MPPT (ISOS-L-1). Devices also demonstrate exceptional thermal stability, retaining 92% of their initial PCE after ageing at 85°C for 1,800 hours (ISOS-D-2) and 94% after 200 thermal cycles between -40°C and +85°C (ISOS-T-3).

Functional polymer passivation layers are advantageous for achieving durable defect passivation under operational conditions, owing to their bulky, long-range-ordered structures and multiple anchoring sites. Polymers incorporating functional groups such as carbonyl, amino, pyridine, thiophene, and cyano can strongly interact with perovskite through coordination bonding, effectively reducing surface defect densities.[190] A self-assembled monolayer of amphiphilic silane (AS) molecules serves as a "molecular glue" to strengthen adhesion toughness of ITO/perovskite/C_{60} interface.[223] Strong Si-O bonds formed through silanization anchor the molecules to the TCO surface, while the amino group ($-NH_2$) groups chemically interact with C_{60}, thereby reinforcing interfacial bonding. The fully printed devices showed no performance degradation after being stored under ambient conditions for more than 3,000 hours. More recently, the mechanical properties of perovskite films were strengthened by incorporating a polymer-coupled monolithic single-layer graphene interface (**Figure 9D**).[224] Benefiting from graphene's mechanical strength and the polymer coupling effect, this structure suppresses photoinduced lattice expansion from 0.31% to 0.08%, and mitigating expansion-induced damage near grain boundaries. In addition, the interlayer acts as a physical barrier that limits the lateral diffusion of mobile species, thereby protecting the underlying perovskite film. As a result, the devices demonstrated excellent stability, retaining over 97% of their initial PCE after more than 3,670 hours of MPPT at 90°C.

3.2.2 Functionalized Materials at the HTL/Perovskite Interface

Suppressing interfacial reactions while maintaining efficient hole extraction is critical for stabilizing the HTL/perovskite interface. Nanocomposite interfacial layers have emerged as an effective strategy, as they can simultaneously enable defect passivation, facilitate charge transport, and provide structural protection at the HTL/perovskite interface. A physical passivation technique involves generating fixed charges using ALD-deposited aluminum oxide nanoparticles (Al_2O_3, which carry negative fixed charges) at the perovskite/NiO_x interface.[225] This fixed charge passivation modifies the carrier concentration distribution near the heterojunctions, thereby facilitating hole extraction and reducing interfacial recombination. Moreover, the strong acidity of Al_2O_3 nanoparticles protects the perovskite from deprotonation by NiO_x at elevated temperatures. The encapsulated devices, operated at MPP, show almost no efficiency loss after ageing under continuous illumination for 2,000 hours (85°C, air). Furthermore, the incorporation of an amorphous-crystalline silicon nitride (CS-Si_3N_4) nanocomposite at the HTL/perovskite interface stabilizes large-area perovskite modules (1,252 cm^2), enabling stable power output for over six months of outdoor operation.[226] The nano-cacher effectively mitigates charge accumulation and disrupts the self-reinforcing cycle of degradation. Specifically, the amorphous shell passivates surface defects due to its low density of dangling bonds, while the crystalline core mitigates defect evolution ($I_i^+ + e^- = I_i^0$) by trapping accumulated charge carriers during operation (**Figure 9E**). This charge trapping strengthens the internal electric field for charge extraction and suppressing defect evolution caused by carrier accumulation.

Lewis-base functional groups can functionalize the HTL/perovskite interface layer to passivate undercoordinated metal cations defects at the HTL/perovskite interface. For example, a mercapto-functionalized mesoporous silica layer was introduced as a superstructure at the PEDOT:PSS/NBG perovskite interface. The chelating interaction between the functionalized sulfhydryl (-SH) group and metal cations, i.e., Sn^{2+} and Pb^{2+}, suppresses the I^- ion migration and Sn^{2+} oxidation, thus suppressing the formation of I_2 and Sn^{4+} defects.[40] The all-perovskite TSCs maintained 90% of their initial efficiency after 445 hours of MPPT (ISOS-L-1I). 1,3-bis(diphenylphosphino)propane (DPPP), a diphosphine Lewis base, can passivate the undercoordinated Pb^{2+}, and bridge the HTL/perovskite interfaces and grain boundaries of the perovskite absorber (**Figure 9F**).[227] The devices showed a PCE slightly higher than their initial PCE after MPPT over 3,500 hours at room temperature and maintained ~90% of their initial PCE after 1,500 hours of thermal stress test

(85°C; ISOS-D-2).

The introduced polymers can also act as both a mechanical buffer and a chemical stabilizer at the HTL/perovskite interface. Their viscous nature helps to absorb and dissipate optical and thermal stresses that typically degrade the HTL/perovskite interface during device operation.[228-230] Hou et al. introduced a cohesive guanidine polymer where the guanidine motifs chemically bridge the perovskite/substrate layers, as macromolecular glue, effectively restricting the interfacial ion migration and morphology variation under environmental stresses.[228] This mechanical strengthening of the HTL/perovskite interface, enabled the devices with a T_{97} lifetime exceeding 1,630 hours of MPPT at 55°C.

View Article Online
DOI: 10.1039/D5EE07642K

3.2.3 Controllable 2D Perovskite Engineering the Perovskite/CTL Interface

The integration of two-dimensional (2D) perovskites as interfacial layers has emerged as a powerful strategy to enhance the light and thermal stability of inverted PSCs. Compared with their 3D counterparts, 2D perovskites exhibit suppressed ion migration in both lateral and vertical directions, primarily due to their lower intrinsic defect density (e.g., reduced vacancy concentration) and the steric hindrance imposed by the bulky organic spacer layers, which restrict ion migration pathways. Notably, the microstructural and phase heterogeneities of 2D perovskite passivators can influence their passivation efficiencies and durability of passivation efficiencies.

A key parameter in 2D perovskites is the dimensionality factor-n, which represents the number of inorganic layers per structural unit and critically governs the environmental stability. It has also been demonstrated that the activation energy for halide exchange reactions increases with decreasing n-value, indicating that lower-n phases offer stronger resistance to halide ion migration and compositional redistribution.[231] However, the random orientation of the spontaneously formed 2D phase atop the pre-deposited 3D perovskite film can deteriorate charge extraction owing to energetic disorder, limiting the maximum achievable PCE and long-term stability of inverted devices. To address this issue, current strategies focus on optimizing the thickness and orientation of the 2D passivation layer to avoid excessive transport barriers, engineering quasi-2D phases with controlled n-value distributions, and tailoring energy-level alignment to minimize interfacial resistance.

Phase-pure 2D perovskites employed as surface passivation layers form well-defined quantum-well architectures with a relatively uniform interfacial energy landscape.[232] In this configuration, inorganic slabs are uniformly encapsulated by organic spacer layers, which effectively mitigate environmental attack and ion migration, thereby enhancing interfacial robustness and operational stability. To further optimize these interfacial structures, a range of molecular engineering have been developed, including rational ligand structural design, such as conjugation extension and steric modulation[233-236], as well as tailoring coordination interactions (e.g., ligand-ligand and ligand-solvent interactions)[237-239], to regulate the interfacial assembly of 2D perovskite layers. For example, a surface-confined phase-pure 2D passivation layer was achieved by a dual-ligand co-deposition approach. The preferential adsorption of bulky 3,6-dimethyl-carbazole-9-ethylammonium iodide regulates the reaction between m-fluorophenylethylammonium iodide (mFPEAI) and the perovskite surface, leading to a 2D layer with a narrower quantum-well distribution (n=1) and more homogeneous energy landscape. The dual-ligand modulated 2D perovskite layer endowed the devices with superior operational stability (T_{90} > 1,000 hours) and enhanced thermal robustness, compared with single mFPEAI passivation with a disordered n-phase distribution and shorter device lifetime (T_{80} ≈ 500 hours).[237]

Another direction aims at refining post-treatment processing (e.g. solvent, annealing temperature) and rational ligand design. A meta-amidinopyridine ligand and a solvent post-dripping step were introduced to generate a highly ordered 2D perovskite phase (n=1) on the surface of 3D perovskite.[240] The MAP ligand, featuring an asymmetric structure and a strong dipole moment, induces the reorientation of 2D domains from random to ordered alignment during the multiple isopropanol (IPA)-dripping process. Meanwhile, the multiple post-dripping redissolved the unreacted MAP ligand in IPA and thus facilitated the reconversion to 2D perovskites with a preferable parallel orientation (**Figure 9G**). Devices based on the reconstructed 2D/3D perovskite maintained 82% and 75% of their initial PCE after 1,000 hours and 840 hours under damp-heat (85°C, 85% RH; ISOS-D-3) and outdoor tests. Additionally, the incorporation of heteroatoms (e.g., O, S, N, F, Cl, Br, I) into bulky A-site organic cations introduce additional non-covalent interactions, including hydrogen bonding, halogen bonding, and S-S interactions. These interactions reinforce lattice cohesion and modulate interlayer coupling, thereby governing the phase distribution and crystallographic orientation of the surface

2D perovskite domains.[241, 242] Liu et al. developed the morpholine hydriodide (MORI) and thiomorpholine hydriodide (SMORI) to modify the perovskite surface by introducing O or S to replace N in the piperazinium iodide (PI) molecule. The 1D perovskite capping layer (with PI) is transformed into a 2D perovskite capping layer (with MORI or SMORI, n = 1), which achieved more robust surface passivation and stronger n-N homotype 2D/3D heterojunctions for facilitating charge transport. SMORI-based devices maintained over 87.6% of their initial efficiency while PI-based devices dropped to ~63.3% of initial efficiency after 1,500 hours of MPPT (45°C).[235]

Despite the significantly advanced performance and stability of devices, some issues still exist in the 2D/3D heterointerface, primarily arising from ionic diffusion and intrinsic instability of organic ammonium ligands. Ionic diffusion between the surface 2D perovskite and the underlying 3D perovskite leads to the structural dimensionality transformations under light or heat.[173] Strategies to suppress cation diffusion in 2D-3D perovskites include: (1) establishing molecular bridging at the 2D/3D interface to enhance interfacial cohesion[174, 243-247]; (2) leveraging intermolecular interactions between dual organic ammonium ligands to impose steric confinement[248-250]; and (3) engineering the functional groups of 2D cations to strengthen binding and reduce ion mobility[251]. For example, Li et al. introduced a cross-linked polymer (CLP) interlayer atop the 3D perovskite, followed by the deposition of a 2D perovskite layer using a vapor-assisted two-step process, thereby forming a robust 3D/CLP/2D heterostructure.[174] More recently, Zhou et al. incorporated a PCBM molecular interlayer to modulate the interfacial reaction between the 2D passivation layer and the underlying perovskite.[243] This strategy enables the formation of a uniform, phase-pure 2D perovskite capping layer (n =1 and 2). The resulting devices exhibited a laminated heterointerface on the electron-extracting side, which enhances charge extraction dynamics through favorable band alignment while simultaneously improving film stability via structural protection. Benefiting from this engineered interface, the devices achieve T_{90} operational lifetimes exceeding 1,000 hours under both damp-heat (85°C, 85% RH; ISOS-D-3) and MPPT in N_2. This research provides an innovative solution to the instability issues associated with conventional ammonium salts surface-treatment.

In parallel, the chemical instability of conventional ammonium ligands, particularly their tendency to deprotonate into amines under thermal and illumination stress, further limits device durability.[9, 138] Huang et al. introduced ammonium cations with a high acid dissociation constant (pK_a), such as $PEAMA^+$ (pK_a = 12.0) and $BAMA^+$ (pK_a = 12.0), to replace conventional PEA^+ or BA^+ for passivation, offering enhanced resistance to further deprotonation.[138] Consequently, PSCs incorporating the $PEAMA^+$ demonstrated the remarkable stability, retaining over 90% of their initial efficiency after 1,500 hours of continuous illumination at open-circuit conditions and 90°C. Sargent's group explored nonreactive ammonium ligands for perovskite passivation, systematically varying ligand structures (**Figure 9H**).[9] They found that fluorinated aniliniums effectively passivate interfaces while minimizing reactivity. Encapsulated devices achieved a T_{85} lifetime of 1,560 hours of MPPT (85°C, 50% RH; ISOS-L-3). Building further upon these insights, Yang et al. addressed the intrinsic instability of conventional ammonium ligands, which are prone to deprotonation under prolonged thermal and light exposure.[11] They developed a library of amidinium-based ligands, leveraging their resonance-stabilized structures and strengthened N-H bonds to enhance thermal robustness. The optimized devices exhibited exceptional thermal durability, achieving a T_{90} lifetime of 1,100 hours of MPPT (85°C, 50% RH; ISOS-L-3). In addition, leveraging intermolecular interactions provides an alternative route to suppress ion migration. For instance, methylammonium (MA^+) was employed to disrupt intermolecular interactions between ethylenediammonium (EDA^{2+}) and formamidinium (FA^+) during solution post-treatment, thereby directing the selective formation of a well-defined n = 3 Dion-Jacobson (D-J) surface heterostructure, and enabling modules to retain over 90% of their initial efficiency after >1,000 hours of outdoor operation.[252] Collectively, these results highlight that stabilizing the 2D/3D heterointerface requires simultaneous control over ion diffusion and ligand chemical stability. Future strategies should further suppress ligand intercalation and structural evolution under thermal stress to achieve long-term durability.

2D perovskite layer is also introduced at the HTL/perovskite interface for stability improvement. Chen et al. systematically investigated bottom interface modification in inverted PSCs using three types of 2D spacers: Ruddlesden-Popper (RP), Dion-Jacobson (DJ), and strong passivation spacers (ACI).[253] The performance enhancement was attributed to the formation of 2D/3D heterojunctions, where the cascade valence band alignment promotes hole

extraction, and the electron back-scattering field suppresses interfacial recombination. The unencapsulated devices retained 90% of their initial efficiency after 30 days under ambient conditions (30 ± 5% RH). Incorporating bottom-up 2D/3D heterostructures through doping 4-hydroxybenzylamine (HBzA) into the perovskite precursor significantly improved the device stability, maintaining performance under damp-heat conditions (85°C, 85% RH; ISOS-D-3).[254] However, achieving solution-processed HTL/perovskite heterostructures remains challenging due to solvent incompatibilities, which disrupt the underlying layer and cause texture incompatibilities and resulting in incomplete coverage on rough substrates. Alex et al. developed a hybrid two-step deposition method to form robust 2D perovskite layers with cross-linkable ligands beneath the 3D perovskite layers.[255] This structurally coherent interlayer promotes strain-free and uniform growth of the upper perovskite, suppresses interfacial defect-induced instability and recombination, and enhances charge extraction through ideal energy-level alignment. Perovskite/silicon TSCs based on industrially textured Czochralski (CZ) silicon retain 89% of their initial efficiency after more than 1,000 hours of operation (65°C, 60% RH; ISOS-L-3).

View Article Online
DOI: 10.1039/D5EE07642K

View Article Online
DOI: 10.1039/D5EE07642K

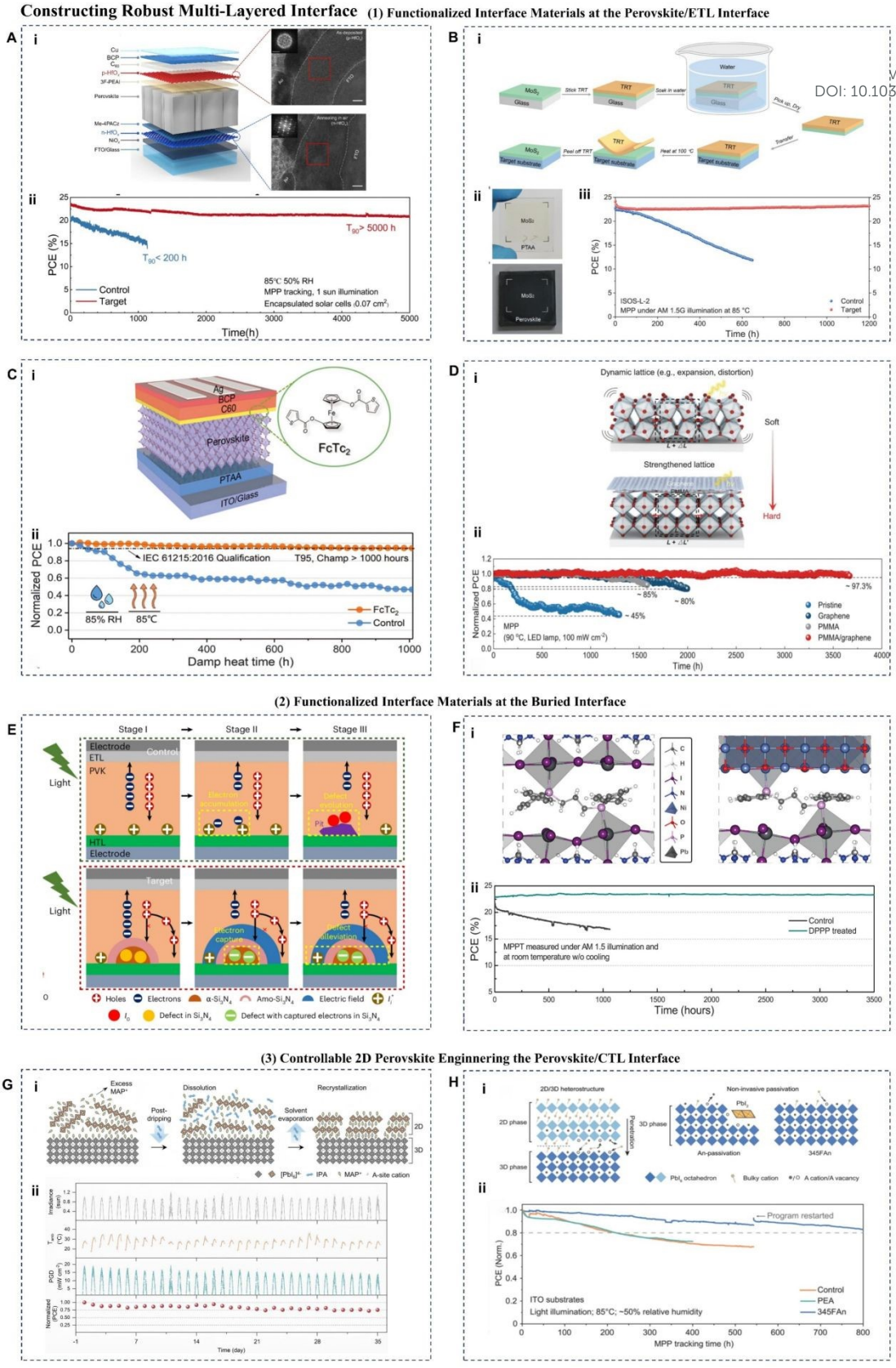

Figure 9. **Constructing Robust Multi-Layered Interface.** (A) (Ai) Device architecture with multifunctional HfO_x integration, and HR-TEM images of p-HfO_x and n-HfO_x films; the sample structure is FTO/p- or n-HfO_x (15 nm; 150 ALD cycles)/Au (5 nm). (Aii) MPPT of devices under 1-sun illumination in ambient air (85°C, 50% RH).[13] Copyright 2026, Science Press. (B) (Bi) Schematic diagram of the transfer process of the MoS_2 film. (Bii) Photographs of the MoS_2 films transferred onto the surfaces of PTAA and perovskite. (Biii) MPPT of encapsulated devices under AM 1.5G illumination at 85°C in ambient atmosphere.[12] Copyright 2025, Science Press. (C) (Ci) Schematic illustration of inverted PSC based on $FcTc_2$ as the interface functionalization material. (Cii)

Encapsulated devices stored in 85% RH and 85°C (ISOS-D-3).[216] Copyright 2025, Science Press. (D) (Di) The alterations in the perovskite lattice structure induced by light radiation exposure and schematic diagram of the transfer process of monolayer graphene to the perovskite film surface. (Dii) Long-term operational stability of devices with various interfacial structures (MPPT, 90°C).[224] Copyright 2025, Science Press. (E) Schematic illustration of the defect evolution.[226] Copyright 2026, Nature Publishing Group. (F) (Fi) Two perovskite slabs and perovskite and NiO_x substrate through chemical-bond formation between P and Pb or Ni atoms in a Lewis acid-base reaction. (Fii) MPPT of devices measured under continuous 1-sun illumination in an N_2 at 40°C.[227] Copyright 2023, Science Press. (G) (Gi) Schematic illustrating the reorientation of the 2D-MAP perovskite during and after the post-dripping process. (Gii) Outdoor stability of a 2D-MAP-ordered device. The outdoor stability measurements were conducted on the KAUST campus in Thuwal, Kingdom of Saudi Arabia, from December 2023 to January 2024 for 35 days.[240] Copyright 2025, Nature Publishing Group. (H) (Hi) Schematic depiction of the model of ammonium ligand and perovskite interactions. (Hii) MPPT of encapsulated control, PEA, and 345FAn devices performed using ITO substrates (85°C, ~50% RH, 0.8-sun illumination).[9] Copyright 2023, Science Press.

View Article Online
DOI: 10.1039/D5EE07642K

Table 2. Stability development of single-junction and tandem solar cells by constructing robust multi-layered interface.

Year	Strategy	PCE (certified)	Stability Improvement Mechanism	Stability of devices	
				Operation	Thermal/Light/Humidity
Single-junction PSCs					
Perovskite/ETL Interface					
2022	Oganometallic forrocene derivative (FcTc2)[216]	25.0	Strong Pb-O coordination, facilitates electron transfer by delocalized ferrocene	T_{98}>1,500 h (ISOS-L-1)	T_{95} > 1,000 h (ISOS-D-3; 85°C, 85% RH), T_{85}> 200 cycles (-40-85 °C)
2024	Ferrocenyl tetraphenylporphyrin cobalt (FcTTPc)[217]	25.39	C=O/C-S coordinate with Pb^{2+}, robust π-π interactions of thiophene-PCBM promote electron transport	T_{94}~1,000 h (N_2)	$T_{88.7}$~800 h (60°C, Dark) $T_{96.2}$~1,600 h (25°C, 40% RH)
2025	Polymer-coupled monolithic single-layer graphene[224]	24.6	Restricts photoinduced lattice expansion	T_{97}>3,670 h (90°C)	T_{98}>1,656 h (~1.3×10^3 Pa, Light)
2025	Laminate-structured perovskite heterointerface[243]	25.97	Stacked with a 2D molecular layer, a PCBM interlayer, a 2D perovskite layer (n=1 and 2)	T_{90}>1,000 h (N_2)	T_{90}>1,000 h (ISOS-D-3; 85°C, 85% RH)
2025	Fluorinated isopropanol (FIPA) as post-treatment solvent[256]	26.0	FIPA reduces the passivator reactivity to enable complete passivation	T_{80}~1,000 h (ISOS-L-3; 65°C, N_2)	/
2025	Sodium-heptafluorobutyrate (SHF) [257]	27.02 (26.96)	Ion shield, promotes a compact C_{60} layer to blocks ion diffusion	T_{100}~1,000 h (ISOS-L-1)	T_{92}~1,800 h (ISOS-D-2; 85°C); T_{94}~200 cycles (ISOS-T-3; -40°C-85°C)
2026	Electron-selective SAM (3PDPA)[258]	26.82	P=O coordinate Pb^{2+} defects, stable H-bonded rings with FA^+, π-π interactions with C_{60} to enhance interfacial contact	T_{90}~1,000 h (ISOS-L-3; 65°C, 50% RH)	/
HTL/Perovskite Interface					
2023	Porous Al_2O_3 (~100 nm) insulator contact[52]	25.5 (24.7)	Contact area reduction, defect passivation at perovskite/PTAA interface	T_{98}>1,000 h (35-40°C)	T_{98}~1,000 h (unencapsulated, 85°C, N2)
2023	ALD-deposited Al_2O_3[225]	22.5	Suppresses perovskite/MO interfacial reactions, modulates charge distribution via fixed negative charges	/	No loss~2,000 h (85°C, Air, Light)
2026	Amorphous (shell)-crystalline (core) Si_3N_4 nanocomposite[226]	26.65 (26.37)	Nano-cacher mitigates charge accumulation and defect evolution	T_{95}~3,000 h (Air) Module:6-months stable power output	/

2023	1,3-bis(diphenylphosphino)propane (DPPP)[227]	24.5	Diphosphine Lewis-base passivates and bridges the perovskite/NiO_x interface via P-Pb coordination	T_{100}>3,500 h (25°C)	T_{80}>1,500 h (ISOS-D-2; 85°C); No degradation>1,500 h (85°C, Light)
2025	Aluminum glycinate organometallic molecule[188]	26.74 (26.21)	Al-OH anchors O=P-OH/NiO-OH of NiO_x/SAM, -NH_2-Pb^{2+} coordination retards crystallization/passivates defects	T_{92}~1,200 h	T_{91}~1,200 h (25°C, 85±5% RH); T_{91}~1,200 h (85°C, N_2)
HTL/Perovskite/ETL Dual-Interface					
2024	4-hydroxybenzylamine (HBzA) ligand[14]	25.6 (25.0)	Forms near-phase-pure 2D perovskite layers at top and bottom interfaces	T_{90}~1,000 h (40°C)	T_{95}~1,000 h (85°C, Air, Light)
2025	Double-side wafer-scale continuous MoS_2 monolayer[12]	26.21 (25.9)	Physically blocks ion migration, stabilizes α-$FAPbI_3$ via Pb-S bonding	T_{96}>1,200 h (ISOS-L-2; 85°C); No degradation~2,000 h (RT)	T_{95}>1,200 h (ISOS-D-3; 85°C, 85% RH); $T_{96.6}$~2,000 h (Light)
2025	Double-side HfO_x by ALD[13]	27.1 (26.6)	n-HfO_x promotes tridentate SAM coordination, p-HfO_x anchors 3F-PEAI via Hf…F at the perovskite/C_{60} interface, blocking I^-/Ag^+ migration	T_{90}>5,000 h (ISOS-L-3; 85°C, 50% RH)	/
Perovskite/Si Tandem Solar Cells					
2022	MgF_x interlayer[96]	(29.3)	Mitigates C_{60}-induced gap state, improves band alignment at the perovskite/C_{60} interface	/	T_{95}~ 1,000 h (ISOS-D-3; 85°C, 85% RH)
2024	Dual-interface 2D/3D heterojunction[259]	31.2	Passivates defect, tuns energy-level alignment at adjacent contacts	T_{80}~1,700 h	/
2025	n-type regulation ($SbCl_3$) of 2D perovskite interlayers[260]	33.10 (32.53)	Passivate defect, tuns energy-level alignment at perovskite/C_{60} interface	$T_{90.2}$~1,000 h (ISOS-L-2; 25°C); $T_{92.8}$~350 h (ISOS-L-2; 85°C)	/
2025	1,3-diaminopropane dihydroiodide (PDAI) dipole layer[133]	33.1	Chemical and field-effect passivation	Stable for 1,000 hours (Outdoor stability)	$T_{83.4}$~1,000 h (ISOS-D-3; 85°C, 85% RH)
All-Perovskite Tandem Solar Cells					
2025	Precisely tuned 3D/Quasi-2D perovskite heterojunctions (WBG)[261]	28.99 (28.81)	Controlled evaporation/solution processing forms uniform 2D phase at the perovskite/C_{60} interface	T_{80}~501 h	/
2025	Parallel dipole regulation (POEAX) (WBG)[262]	28.92 (28.51)	Dipoles passivate Pb^{2+} defects, and facilitate electron extraction	T_{80}>1,000 h (N_2)	/
2025	Mercapto-functionalized mesoporous silica layer (NBG)[40]	29.6 (29.5)	Regulates crystallization, passivates defects, suppresses Sn^{2+} oxidation at HTL/perovskite interface	T_{90}~445 h (Air)	/
2025	Sulfanilic acid (SA) layer (NBG)[263]	30.6 (30.1)	Dipole-assisted defect passivation, matched band alignment at HTL/perovskite interface	T_{87}~1,025 h (Air)	/

3.3 Rational Design of Self-assembled Monolayers (SAMs)

Self-assembled monolayers (SAMs) are central to improving the chemical, thermal, and mechanical stability of inverted PSCs, as they define the properties of the buried interface. However, structural degradation or desorption within the SAM layer, as well as interfacial evolution at the SAM/perovskite junction, can progressively destabilize this interface, leading to leakage currents, enhanced non-radiative recombination, and device deterioration. The inferior wettability and anchoring variation also amplify device-to-device inconsistencies. To address these challenges, stability engineering of SAM-based buried interfaces can be systematically approached from four key aspects: (i) Designing intrinsically stable SAM molecules with robust chemical backbones and improved resistance to thermal and photo-

induced degradation; (ii) Strengthening SAM anchoring on MO substrates to mitigate desorption and ensure durable interfacial bonding; (iii) Enhancing the surface wettability of SAM-modified substrates to promote uniform perovskite deposition; (iv) Minimizing defective sites at the buried interface through defect passivation and electronic structure optimization. Moving forward, further optimization of SAM, particularly regarding molecular ordering control, and compatibility with large-area processing, will be required to ensure reproducible interfacial properties and long-term operational stability, thereby facilitating scalable manufacturing.

View Article Online
DOI: 10.1039/D5EE07642K

3.3.1 Designing Intrinsically Stable SAMs

Weak intermolecular interactions of SAMs are easily disrupted under thermal and light stress, resulting in disordered packing that reduces both the dipole moment and hole-transport efficiency.[264] Therefore, achieving a balance between facile processability and robust molecular ordering requires the deliberate design of both the linker and terminal groups of SAMs molecules. Building upon prototypical SAMs such as 2PACz, MeO-2PACz, and Me-4PACz, researchers have progressively developed a broader library of tailored SAMs, enabling more stable and efficient inverted PSCs. Mainstream SAM design strategies, such as π-expansion, conjugated linkers, and ring condensation, enhance conjugation and electron delocalization, thereby improving conductivity and interfacial stability.

Dibenzo[c,g]carbazole (DBC) moiety features a non-coplanar screw-shaped configuration arising from steric repulsion between terminal aromatic rings. This π-expansion structural feature effectively hinders molecular aggregation and enhances the solubility of SAMs.[265] Building on this structural advantage, Jen et al. designed two novel HTMs, CbzPh ((4-(7H-benzo[c]carbazol-7-yl)butyl)phosphonic acid) and CbzNaph ([4-(7H-dibenzo[c,g]carbazol-7-yl)butyl]phosphonic acid), by modifying the carbazole core of 4PACz with asymmetric or helical π-expansion.[266] The helical π-expanded CbzNaph exhibited a pronounced molecular dipole (2.41 D), a well-aligned HOMO level, and compact π-π stacking, promoting the formation of a compact and ordered monolayer. Devices incorporating CbzNaph demonstrated significantly superior performance compared with those based on CbzPh and 4PACz. Almost simultaneously, Zhao et al. introduced CbzNaph (they denoted as 4PADCB) in WBG (1.77 eV) sub-cell of all-perovskite TSCs.[267] Incorporation of 4PADCB improved SAMs coverage and orderliness, thereby accelerating hole extraction and suppressing nonradiative recombination (**Figure 10A**). The monolithic all-perovskite TSCs (aperture area of 1.044 cm²) retained 80% of their initial efficiency after 415 hours of MPPT, markedly outperforming counterparts based on PTAA and 4PACz.

Another design strategy involves introducing a conjugated phenyl linker between the carbazole unit and the anchoring group, thereby improving the charge transport while stabilizing the arylamine moiety through electron delocalization.[268-270] For example, compared with the conventional MeO-2PACz, which contains a flexible alkyl linker, the newly designed molecule 2-(3,6-dimethoxy-9H-carbazol-9-yl)phenyl cyanoacetic acid (Cz-CA) exhibits extended conjugation, with both the HOMO and LUMO delocalized across the linkage group.[268] This enhanced conjugation not only facilitates charge transfer but also improves photochemical robustness under light soaking. After 12 hours of light soaking, the UV-vis absorption peak of MeO-2PACz (around 370 nm) decreased by more than 30%, accompanied by a color change from transparent to light yellow, indicating molecular degradation. In contrast, Cz-CA maintained nearly unchanged absorption intensity under the same conditions. Consistently, devices based on MPA-Ph-CA retained over 95% of their initial PCE after 800 hours of MPPT, highlighting the critical role of conjugated linker engineering in enhancing both molecular durability and operational stability.

However, excessive conjugation often induces molecular stacking, which compromises film uniformity in large-area solution processing. Donor-acceptor (D-A) molecular engineering offers an effective strategy to regulate electronic structure while mitigating excessive π-π stacking.[24] For example, a light-stable donor-acceptor interface was constructed using an asymmetric carbazole-based SAM (BrAs) and N-hydroxyethyl phthalimide (PIE).[24] The single-sided electron-withdrawing bromine in BrAs preserves wettability and reduces the valence band offset. Meanwhile, the asymmetric dipole reorients carbazole units and strengthens short-range Coulomb interactions, enabling densely packed and uniform SAM coverage for efficient carrier transport. The devices retained over 95% of their initial efficiency after 1,500 hours of illumination (65°C; ISOS-L-2). Building on this concept of electronic structure regulation, stable open-shell diradicals offer an alternative strategy.[271-273] Their unpaired electrons increase carrier density and create favorable orbital energies,

thereby overcoming poor conductivity. Bulky steric groups further stabilize the radicals, ensuring molecular robustness and solution processability. Qin et al. developed open-shell diradical SAMs using a coplanar D-A design.[273] As shown in **Figure 10B**, strong D-A interactions and planar conjugation enabled efficient diradical generation and stabilization. Additional steric hindrance further improved stability and solution processability. The device maintained 97% of its initial efficiency after 2,000 hours of MPPT at 45°C.

View Article Online
DOI: 10.1039/D5EE07642K

Incorporating fused-ring structures with heteroatom substitutions as terminal groups can improve the chemical stability of SAMs by increasing molecular rigidity and modulating electronic delocalization.[274] By introducing a sulfur-containing terminal group, the MeO-BTBT molecule achieves a more delocalized electron distribution and a favorable LUMO level, which collectively suppress photo-induced oxidation. The MeO-BTBT based devices can maintain approximately 95% of their initial values after 1,000 hours aging (65°C; ISOS-L-2). Moreover, heteroatoms can form strong interactions with the perovskite surface, thereby enhancing interfacial coupling. Sulfur-modulated fully-conjugated SAMs, 5-(4-bis(4-methylthiophenyl)amino)phenyl) thiophenylphosphonic acid (SMe-TPA-ThPA) were developed to achieve a T_{90} lifetime exceeding 1,700 hours under 25°C (ISOS-L-1) and 65°C (ISOS-D-2).[275] Methylthio substituents enhance interfacial defect passivation, while the thiophene linker in SMe-TPA-ThPA strengthens intermolecular interactions, improves energy-level alignment with the perovskite, promotes uniform coverage on ITO, and enables efficient hole extraction.

However, heteroatom substitution represents a double-edged design strategy. While it can improve carrier transport and tune energy levels, excessive bond polarization or the introduction of chemically active sites may compromise the intrinsic molecular robustness, rendering SAMs more susceptible to degradation under external stress. In contrast, the heteroatom-free molecule (2-(pyren-1-yl)ethyl)phosphonic acid (Py3), featuring a highly conjugated pyrene core, minimizes bond polarization while maintaining extended electron delocalization (**Figure 10C**).[19] Devices based on Py3 exhibited an extrapolated T_{90} exceeding 10,000 hours of MPPT under accelerated aging conditions (85°C), highlighting their exceptional long-term operational stability. These results highlight that the molecular stability of SAMs is governed by the balance between electronic delocalization and bond polarization. Rational molecular design aimed at achieving uniformly delocalized electron distribution while minimizing chemically vulnerable sites offers a robust strategy to enhance both structural and operational stability.

3.3.2 Strengthening SAM anchoring on MO substrates

One persistent challenge in SAM formation is molecular aggregation during deposition, which often results in suboptimal packing density and poor uniformity, even on flat substrate.[20, 276, 277] This issue primarily stems from the limited solubility of phosphonic acids and their suboptimal bonding with MO surfaces. The introduction of additives into SAMs to engineer co-assembled monolayers (Co-SAMs) has emerged as an effective strategy to overcome this problem. By introducing a co-adsorbent strategy to disassemble high-order phosphonic acid aggregates, a significantly more homogeneous molecular distribution and high coverage was achieved on textured ITO substrates.[277] The low-loss contacts endowed devices with a T_{95} operational lifetime exceeding 1,000 hours (65°C, 50% RH). As a more effective strategy, a hybrid SAM architecture was developed by incorporating a multi-carboxylic acid-functionalized aromatic molecule, 4,4′,4″-nitrilotribenzoic acid (NA), into the Me-4PACz monolayer on NiO_x surface.[20] Synergistic interactions between Me-4PACz and the triphenylamine moiety inhibited molecular aggregation, leading to a more uniform SAM coverage at the NiO_x/perovskite interface. Devices exhibited outstanding stability, maintaining 96.1% after over 2,400 hours of MPPT under ambient conditions (65°C), and 97.4% of their initial PCE after 500 hours of damp-heat aging (85°C, 85% RH; ISOS-D-3).

In parallel, stability at the SAM/MO interface remains a critical issue, as external stress can disrupt the chemical bonds between the SAMs and MO substrates, which triggers SAMs desorption and undermines device stability. The absorption behavior of SAMs on MO substrates depends on their chemical structures. One effective strategy is to increase the number of anchoring groups. For example, Yip et al. designed TPA2P((2-(4-(diphenylamino)phenyl) -1-phosphonovinyl)phosphonic acid), a novel SAM material featuring a conjugated bisphosphonic acid anchoring group **(Figure 10D)**.[278] The dual phosphonic acid configuration enhances substrate binding on ITO, improves SAM uniformity, and increases interfacial stability. Unencapsulated TPA2P devices retained 96.7% of their initial PCE after 1,000 hours

of MPPT (40±5°C; ISOS-L-1I). The development of ((9H-fluoren-9-ylidene)methyl)cyanophosphonic acid (FY-CPA) introduced a rigid multidentate molecule capable of forming strong tetradentate coordination with the underlying NiO_x layer, thereby enhancing interfacial binding and promoting efficient charge extraction **(Figure 10E)**.[279] The device maintained 96.5% and 93.8% of its initial efficiencies after MPPT at 50°C for 1,000 hours and aging at 85°C in N_2 atmosphere over 1,300 hours, respectively.

View Article Online
DOI: 10.1039/D5EE07642K

Another strategy to enhance the stability of MO/SAMs interfaces is to regulate molecular orientation during anchoring MO substrate, thereby promoting ordered assembly and improving interfacial electronic coupling. SAMs based on functionalized π-conjugated cores often adopt an edge-on configuration, where the π-plane is perpendicular to the substrate surface. This orientation can limit orbital overlaps with the perovskite absorber and induce undesired lateral hole transport. To address this issue, a tripodal SAM molecule, 3PATAT-C3, incorporating three phosphonic acid anchoring groups, was designed to enforce a face-on orientation on MO surfaces.[280] This geometry enhances vertical orbital coupling with the perovskite layer and facilitates hole extraction. Consequently, devices based on 3PATAT-C3 exhibit significantly improved operational stability, showing no noticeable degradation after more than 2,000 hours of shelf testing.

In addition to molecular orientation, achieving uniform surface coverage and intimate interfacial contact is critical for stabilizing SAM-based interfaces. An asymmetric SAM, HTL201, was developed as a hole-selective layer for perovskite/silicon TSCs.[281] Compared with symmetric phosphonic acid-terminated SAMs, HTL201 features a carbazole core with asymmetric anchoring and spacer groups, which reduce steric hindrance during self-assembly and enable more uniform coverage on the TCO recombination layer. As a result, perovskite/silicon TSCs incorporating HTL201 retained approximately 98% of their initial efficiency after 1,000 hours of MPPT (25°C; ISOS-L-1I).

Beyond optimizing molecular orientation and surface coverage, ensuring the conformational stability of SAMs under operational stress represents another crucial design principle. Jen et al. introduced a cross-linkable co-SAM system to reinforce the structural robustness of hole-selective SAMs while suppressing defect and void formation during self-assembly.[21] In this design, an azide-containing guest SAM (JJ24) forms covalent bonds with the alkyl linkers of the host SAM (CbzNaph), creating a cross-linked molecular network (CbzNaph: JJ24). This cross-linked structure effectively stabilizes the SAM conformation under external stress and prevents direct contact between the perovskite layer and the TCO substrate, thereby mitigating interfacial degradation and perovskite decomposition (**Figure 10F**). As a result, the devices exhibit outstanding thermal durability, maintaining nearly unchanged performance during MPPT for 1,000 hours (85°C; ISOS-L-2) and retaining over 98% of their initial PCE after 700 thermal cycles (-40 to 85°C; ISOS-T-2), setting a new benchmark for SAM-based interfacial stability.

Beyond SAM molecular design, engineering the MO substrate itself offers an additional approach to strengthen the SAM anchoring. A solution-based strategy was developed to rapidly hydroxylate ITO surfaces within just 15 seconds. This hydroxylation process not only introduces abundant hydroxyl groups but also exposes uncoordinated indium ions, which significantly improves SAM attachment (**Figure 10G**), endowing the devices with exceptional thermal stability, retaining 96% of their initial efficiency after 2,800 hours of MPPT (65°C; ISOS-L-2).[282] The polar solvents used in perovskite precursor solutions can disrupt hydrogen-bonded SAMs, whereas covalently bonded monolayers remain intact. To address this limitation, atomic layer deposition (ALD) was employed to modify ITO substrates with covalently bonded hydroxyl groups, enabling robust trimethoxysilane-functionalized SAM attachment through covalent tridentate achoring.[283] Devices retained 98.9% of their initial PCE after 1,000 hours of damp-heat exposure (85°C, 85% RH; ISOS-D-3) and 98.2% after 1,200 hours of MPPT (85°C; ISOS-L-2I), , demonstrating outstanding interfacial stability in SAM-based devices. When extending to the large-area modules, Shi et al. introduced a green, precise, and scalable laser-induced hydroxylation strategy to overcome these challenges.[284] Laser irradiation creates oxygen vacancies in NiO_x, and air annealing induces a hydroxyl-rich surface with undercoordinated Ni sites, enabling robust tridentate SAM anchoring and densely packing. The resulting modules (65 cm^2) achieved a certified PCE of 22.01%, among the highest efficiencies for large-area modules (50-200 cm^2). The unencapsulated device retained >91% of its initial PCE after 1,500 hours aging (85°C, N_2; ISOS-D-2) and 2,000 hours aging (65°C; ISOS-L-2).

3.3.3 Regulating the Surface Wettability of SAMs

View Article Online
DOI: 10.1039/D5EE07642K

Currently, most SAMs still suffer from intrinsic wettability limitations, which often lead to poor film uniformity and limited device reproducibility.[82, 285] These issues become more pronounced when scaling to large-area modules, where ink dewetting on exposed glass regions around P1 scribe lines can cause pinholes and electrical shunting between sub-cells, thereby degrading module performance.[82]

To address these challenges, multiple interfacial engineering strategies have been developed. One approach involves tuning the surface energy of SAM-modified substrates and improving wetting behavior through adding additives into the precursor solution or by rationally combining different SAM molecules. For example, incorporating 1,3-dimethyl-3,4,5,6-tetrahydro-2(1H)-pyrimidinone (DMPU) into the Me-4PACz solution enhances the interaction between the SAMs and the perovskite precursor ink, leading to improved wettability and more uniform film formation **(Figure 10H)**.[82] This strategy enables WBG PSCs (1.67 eV) with PCE up to 22.4% for small-area devices and 20% for mini-modules (9.8 cm^2), along with high reproducibility. The perovskite/silicon TSCs exhibited improved photostability, retaining 80% of their initial efficiency after 490 hours of MPPT (ISOS-L-1).

Another effective approach involves the rational design of amphiphilic SAMs that simultaneously interact with the substrate and perovskite precursor. Zhang et al. reported an amphiphilic SAM (MPA-CPA) featuring a hydrophilic cyanovinyl phosphonic acid anchoring group and a hydrophobic arylamine-based hole-extraction unit, which enhanced perovskite deposition quality through improved wetting and passivation **(Figure 10I)**.[286] The perovskite modules showed negligible performance loss over 500 hours of MPPT in ambient air (45°C, 30~40% RH; ISOS-L-1), and retained more than 95% of their initial performance after 500 hours aging under damp heat conditions (85°C, 85% RH; ISOS-D-3). Qu et al. developed a functionalized SAM denoted 4-(7H-dibenzo[c,g]carbazol-7-yl)phenyl)phosphonic acid (Bz-PhpPACz) by expanding the molecular π-conjugation to strengthen intermolecular π-π interactions.[287] This design promotes the self-assembly of molecules into an ordered hydrophilic bilayer structure that benefit sthe deposition of high-quality, large-area perovskite films.[287] The devices maintained 91.94% of their initial PCE after 3,000 hours of MPPT at 65±10°C in N_2, representing excellent long-term operational stability. In addition, plasma treatment has been widely employed to modify substrate surface chemistry and morphology, enhancing surface activation and enabling more conformal and homogeneous SAM assembly.[288]

Beyond direct modification of the SAM or substrate, Kirchartz et al. introduced a universal triple co-solvent system composed of dimethylformamide (DMF), dimethyl sulfoxide (DMSO), and N-methyl-2-pyrrolidone (NMP) to enhance the interaction between the perovskite precursor ink and the underlying SAM, thereby mitigating wettability limitations.[289] Compared with conventional DMF- or DMSO-based formulations, the incorporation of NMP significantly increases the binding energy between the perovskite ink and Me-4PACz, leading to improved interfacial adhesion and better perovskite film uniformity.

3.3.4 Minimizing Defective Sites at the Buried Interface

To enhance durability, SAMs are designed with stable structures, often incorporating saturated alkyl chains and large π-conjugated groups that act as barriers to prevent unwanted interfacial chemical reactions caused by MO and the perovskite absorber **(Figure 10J)**. For example, the use of (4-(3,11-dimethoxy-7H-dibenzo[c,g]carbazol-7-yl)butyl)phosphonic acid (MeO-4PADBC), which chemically anchors to NiO_x surface, stabilizing the NiO_x/perovskite interface.[18] Devices incorporating MeO-4PADBC maintained over 80% of their initial efficiency for more than 10 months (ISOS-L-1). Similarly, (4-(7H-dibenzo[c,g]carbazol-7-yl)ethyl)phosphonic acid (2PADBC) at the $FASnI_3/NiO_x$ interface, anchors undercoordinated Ni cations via phosphonic acid groups, which suppressed the reaction between highly active $Ni^{\geq 3+}$ defects and perovskites, and increases the electron density and, consequently, the oxidation activation energy of Sn^{2+} at the perovskite interface (**Figure 10K**).[290] The $FASnI_3$-based devices maintained more than 93% of their initial efficiency after 1,000 hours of MPPT (ISOS-L-1).

As previously noted, device degradation is largely driven by interface defects. The terminal groups of SAMs are critical for enhancing stability by passivating these defects in the perovskite absorber. Hong et al. developed a phenothiazine-based SAM, (2-(3,7-dibromo-10H-phenothiazin-10-yl)ethyl)phosphonic acid (Br-2EPT), which forms Pb-S and halogen bonds with the perovskite, thereby reducing interface trap density and achieving excellent device stability.[291] To further improve passivation efficiency, they replaced the sulfur atom in phenothiazine with oxygen or

selenium, yielding Br-2EPO ((2-(3,7-dibromo-10H-phenoxazin-10-yl)ethyl)phosphonic acid) and Br-2EPSe ((2-(3,7-dibromo-10H-phenoselenazin-10-yl)ethyl)phosphonic acid), respectively.[292] Among these, Br-2EPSe exhibited the strongest interaction with the perovskite. Correspondingly, devices showed different long-term PCE retention after 500 hours of MPPT Br-2EPSe (~96%) > Br-2EPT (~80%) > Br-2EPO (~67%). Encouragingly, the diversity of SAMs also overcomes the limitations caused by acidic PEDOT:PSS in NBG PSCs. Based on 2PACz, Sargent et al. designed SAMs bearing thiol and carboxylic groups, which produce a lowered rate of acidity-related degradation and form strong Pb-S bonding, thus strengthening the HTL/perovskite interface. These devices exhibited the markedly enhanced thermal stability, with a T_{80} of 85 times longer than PEDOT:PSS and well beyond that of 2PACz (< 200 hours).[50]

View Article Online
DOI: 10.1039/D5EE07642K

Additive molecular engineering has been also employed to simultaneously enhance interfacial stability and mitigate bulk defects.[293] Incorporating a redox-active molecule, methylene blue, into Me-4PACz films enabled the selective reduction of $Ni^{\geq 3+}$ defects in NiO_x and the oxidation of metallic Pb^0 species within the perovskite absorber (**Figure 10L**).[294] In addition to passivation, π-π interactions between methylene blue and Me-4PACz molecules improved the monolayer dispersion, reducing voids and aggregates, and resulting in a denser interfacial contact. The resultant devices demonstrated remarkable resilience, maintaining 91% of their initial efficiency after 1,500 hours of UV irradiation and 90% after 1,500 hours of MPPT under harsh damp-heat conditions (85°C, 85% RH; ISOS-D-3). Taken together, these results indicate that rational molecular design and structural optimization of SAMs are critical to mitigating intrinsic interfacial instability at the HTL/perovskite junction.

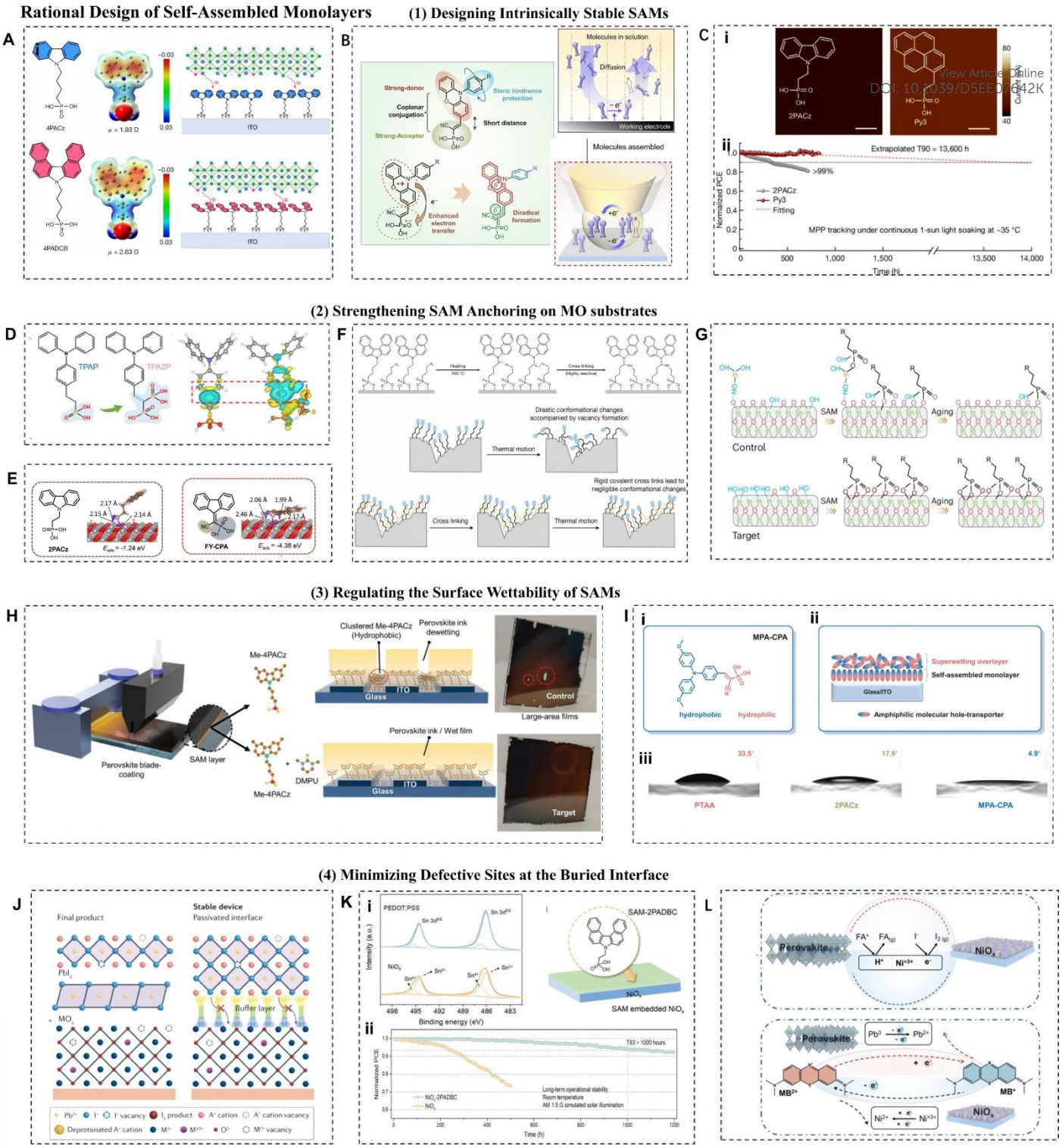

Figure 10. Rational Design of SAMs. (A) Molecular structure and calculated ESP of 4PACz and 4PADCB, and schematic of the interconnection between ITO, HTL and perovskite for 4PACz and 4PADCB.[267] Copyright 2022, Nature Publishing Group. (B) Design concept of open-shell diradical SAMs and schematic diagram of electrochemical measurement for molecules dissolved in solution.[273] Copyright 2025, Science Press. (C) (Ci) Conductive AFM images and the corresponding surface current signals of 2PACz and Py3 SAM. (Cii) MPPT of the devices under continuous 1-sun light soaking at ~35°C.[19] Copyright 2024, Nature Publishing Group. (D) Chemical structures of TPAP and TPA2P, and intramolecular charge density differences of TPAP and TPA2P.[278] Copyright 2025, American Chemical Society. (E) Rational design of molecules through DFT calculations and corresponding binding models of 2PACz and FY-CPA on NiO_x surface.[147] Copyright 2025, Cell Press. (F) (Fi) The proposed cross-linking mechanism between CbzNaph and JJ24. (Fii) Schematic diagram of the random thermal swing of SAM molecules leading to substrate exposure and subsequent perovskite decomposition.[295] Copyright 2025, Nature Publishing Group. (G) Schematic of

SAM bonding on control and target ITO.[22] Copyright 2025, Nature Publishing Group. (H) Blade coating of perovskite ink on control (Me-4PACz) and target (Me-4PACz+DMPU) large-area substrates.[82] Copyright 2024, Wiley-VCH. (I) (Ii) Molecular structure of the amphiphilic MPA-CPA molecule. (Iii) Schematic depiction of the bilayer stack of MPA-CPA molecules on ITO substrate. (Iiii) Contact angles of the perovskite precursor solution on different HTLs.[286] Copyright 2023, Science Press. (J) Schematic illustration of the suppressed defect site by a buffer layer at MO/perovskite interface.[76] Copyright 2023, Nature Publishing Group. (K) (Ki) XPS spectra of Sn elements in perovskite films with low solution concentrations on PEDOT:PSS and NiO_x HTL. (Kii) MPPT of the encapsulated devices at room temperature in N_2.[296] Copyright 2023, Wiley-VCH. (L) Diagram of interfacial redox reactions and inhibition by methylene blue.[294] Copyright 2025, Royal Society of Chemistry.

View Article Online
DOI: 10.1039/D5EE07642K

Table 3. Stability development of single-junction and tandem solar cells by rational design of SAMs.

Year	Strategy	PCE (certified)	Stability Improvement Mechanism	Stability for devices	
				Operation	Thermal/Light/Humidity
Single-junction PSCs					
2023	Conformal SAMs[277]	25.3 (24.8)	3-MP disassembles aggregates, enabling uniform SAM distribution	T_{95}~1,000 h (ISOS-L-3; 65°C, 50% RH)	/
2023	Mixed SAMs (MeO-2PACz and Me-4PACz)[105]	25.5	Improves ion-blocking properties	T_{93}~5,030 h (ISOS-L-1I; 1.2-sun, N_2); T_{90}~22 weeks (Outdoor stability)	No degradation~56 weeks (ISOS-D-1I; N_2); T_{92}>2,560 h (ISOS-D-3; 85°C, 85% RH); C_{95}~1,000 h (ISOS-T-3; -40-85 °C, Dark)
2023	MeO-4PADCB[18]	(25.6)	Stabilize NiO_x/perovskite interface and tuns interfacial band alignment	T_{90}~1,200 h (65°C); T_{74}~1,200 h (85°C) (ISOS-L-2I)	/
2024	*peri*-Fused polyaromatic core structure SAMs (Py3)[19]	26.1	Chemically inert and structurally stable molecular contact	T_{99}>1,000 h (35°C); T_{99}>600 h (55°C)	T_{95}>3,000 h (ISOS-D-2); T_{98}>3,300 h (ISOS-L-2;65°C)
2024	Trimethoxysilane based SAMs (DC-TMPS) on ALD deposited ITO[283]	24.8 (24.6)	Covalent tridentate anchoring on ALD-ITO enhances SAM attachment	T_{98}~1,200 h (ISOS-L-2I)	T_{99}~1,000 h (ISOS-D-3; 85°C, 85% RH)
2025	Self-assembled bilayers[297]	26.3 (26.08)	Covalently linked phosphonic acid SAM-triphenylamine bilayer forms thermally stable polymerized network	T_{98}~1,000 h (ISOS-L-1I; 55°C)	T_{96}>2,000 h (ISOS-D-2); C_{97}>1,200 cycles (ISOS-T-3)
2025	π-expanded SAMs (Bz-PhpPACz)[287]	26.46 (26.39)	Strong π-π interactions promote ordered hydrophilic bilayer structure	T_{92}~3,000 h (65±10°C, N_2)	/
2025	2-methyltetrahydrofuran-processed PTACz-PO HTL[298]	26.31	Green-solvent processable, deep HOMO, high mobility, strong passivation	T_{94}>1,450 h (ISOS-L-3; 65°C, 50% RH)	T_{95}>2,000 h (ISOS-D-2)
2025	Orthogonal π-skeleton SAMs (SAX)[15]	25.1	Disordered amorphous structure enhances resilience to external stimuli	$T_{91.5}$~2,500 h (50°C); T_{90}~400 h (85°C)	T_{95}~1,000 h (ISOS-D-2; 85 °C, Dark); T_{97}~2,000 h (ISOS-L-2; 65°C, Light)
2025	Asymmetric SAMs (4PABCz)[16]	26.9 (26.81)	π-π interactions and dipoles induce tightly packed face-on HTLs	T_{94}~1,000 h (ISOS-L-2)	/
2025	In-situ crosslinked SAMs (JJ24)[21]	26.98	In-situ crosslinking suppresses SAM detachment under thermal stress	T_{100}~1,000 h (ISOS-L-2; 85°C, 70-80% RH)	C_{98}~700 cycles (ISOS-T-2; -40-85°C, Dark)
2026	Photostable donor-acceptor SAM (BrAs)[24]	(27.19)	Dipole-regulated packing, BrAs-PIE D-A energy transfer enhance charge extraction	T_{95}~1,500 h (ISOS-L-2; 65°C)	$T_{88.7}$~1,000 h (85°C, N_2, Dark)
2025	Rigid molecules anchoring NiO_x[147]	26.21	Tetradentate anchoring on NiO_x induces parallel orientation for charge extraction	$T_{96.5}$~1,000 h (50°C, N_2)	$T_{93.8}$~1,300 h (85°C, N
2025	Seeding -OH groups by H_2O_2/ultraviolet bath[77]	26.19	Strengthen and homogenize SAM deposition on substrates (-P-O-Sn…-OH)	T_{90}>1,000 h (ISOS-L-3; 65°C)	/

2025	Fully hydroxylate ITO[22]	26.6	Create abundant uncoordinated In^+ on ITO for SAM anchoring	T_{96}~2,800 h (ISOS-L-2)	T_{98}~1000 h (ISOS-D-3; 85°C, 85% RH); T_{93}~1600 h (ISOS-T-1)
2026	Laser-induced surface hydroxylation of NiO_x[284]	(22.01) 65 cm^2	Induce oxygen vacancies on NiOx surface, enabling tridentate SAM anchoring and densely packing	T_{91}~2,000 h (ISOS-L-2; 65°C)	T_{91}~1,500 h (ISOS-D-2; 85°C, N_2)
Perovskite/Si Tandem Solar Cells					
2025	DMPP SAM[299]	33.86 (33.59)	Prioritizes molecular stability and packing, homogenizes perovskite crystallization	T_{90}~2,000 h (ISOS-L-1)	$T_{80.9}$~624 h (85°C, Light)
2025	Asymmetric SAM (HTL201)[281]	(34.58)	Minimized steric hindrance improves SAM coverage on TCO and coordination with perovskite	T_{98}~1,020 h (25°C, Air); $T_{91.3}$~1,020 h (45°C, Air)	/
2025	In-situ cross-linked SAM (CL-SAMs)[300]	34 (33.61)	Stabilizes SAM structures, improves passivation and perovskite quality	T_{97}>1,200 h (ISOS-L-2; 65°C)	/
2026	Binary mixed SAM[301]	31.4	Strong intermolecular interactions for dense coverage on textured Si	T_{97}~1,000 h (45±10°C, N_2); T_{91}~1,000 h (65±10°C, N_2) (ISOS-L-1I)	/
2026	6AHPACl additive in SAMs[302]	29.1 (1 cm^2)	Modulates pH of SAM to suppress aggregation, dipole facilitate extraction	/	C_{95}~1,010 cycles (-40-85°C, 85% RH)
All-Perovskite Tandem Solar Cells					
2025	MPA-BT-BA SAM (NBG)[51]	28.61	Oligoether chains promote hole extraction, regulate perovskite growth, passivate defects	T_{92}~400 h (ISOS-L-1I)	/
2025	DCB-Br-2 SAM (WBG)[303]	27.70	Passivates V_I, optimizes interfacial band alignment	T_{80}~440 h (ISOS-L-1; 65°C, 85% RH)	/
2025	Poly(carbazole phosphonic acid) SAM (WBG)[304]	28.51	Multiple phosphonic groups enable robust anchoring on NiO_x	T_{80}~700 h (ISOS-L-1I)	/
2025	Less-acidic boric acid SAM (WBG)[305]	28.5	Milder anchoring group chemisorbs onto NiO_x via strong -BO_2-Ni coordination	T_{90}~500 h (ISOS-L-1)	/
2025	5-AVAI additive in Me-4PACz (WBG)[306]	28.9	In-situ compensation of SAM vacancies, defect passivation via -NH_2/C=O groups	$T_{87.3}$~800 h	/
[illegible]	SA additive in Me-4PACz (WBG)[307]	28.94 (28.78)	Co-adsorption with Me-4PACz suppresses competitive deposition	T_{87}~500 h (ISOS-L-1; 45°C, 30-40%RH)	/

3.4 Engineering Stable Electron Transport Layers (ETL)

3.4.1 Engineering Fullerene Derivatives-based ETL

Pristine fullerene (C_{60}) has greatly contributed to the advancement of PSCs, yet its low solubility and strong tendency to aggregate hinders the formation of high-quality solution-processed films, necessitating thermal evaporation to produce well-ordered films. C_{60} functionalization has emerged as a strategy to improve the performance and stability of fullerene-based ETL.[308-310] A C_{60}-polymer assembly strategy by incorporating an n-type polymer, dithienylpyrazine diimide-bithiophene imide (TPDI-BTI), suppresses C_{60} aggregation and enhances both electron transport and interfacial contact.[310, 311] The optimized devices maintained 95% under light soaking (white LED) for 1,800 hours and 80% of their efficiency at 65°C for 700 hours. In another approach, a C_{60}-based ionic salt ETL was developed by Zhu et al. where the introduction of ionic head groups enhanced molecular packing and significantly improved interfacial toughness, achieving a threefold increase compared to pristine C_{60} (**Figure 11A**).[308] Devices employing this ETL exhibited outstanding operational stability, with only a 2% performance loss after 2,100 hours at 65°C. Furthermore, a novel fullerene derivative, BTP C_{60}, was synthesized by grafting a non-fullerene acceptor (NFA) fragment onto the C_{60}

framework.[310] This molecular design disrupted the dense packing of the C_{60} cage and promoted strong fullerene-NFA interactions (**Figure 11B**), enabling devices to retain ~90% of their initial efficiency after 1,500 hours at 85°C.

Additionally, C_{60} are often incompatible with balanced charge extraction in inverted PSCs, which arises from SAMs with conjugated structures typically facilitate faster hole extraction than the electron extraction provided by ETL.[18, 94, 312] To address this mismatch, Liang et al. developed an endohedral metallofullerene-polymer composite ETL, Nd@C_{82}-PMMA, which offers both ultrafast intramolecular electron transfer channels and interfacial polarization, thereby enabling highly efficient and balanced charge extraction.[312] The unencapsulated devices retained ~82% of their initial PCE after 2,500 hours (65°C; ISOS-L-3), ~95% after 1,750 hours (85°C; ISOS-D-2I) and almost exhibited no efficiency reduction during the damp heat test (85°C, 85% RH; ISOS-D-3) over 1,000 hours.

PCBM also faces critical challenges. Under illumination and thermal stress, cycloaddition reactions can occur, leading to the dimerization of PCBM on the perovskite surface.[313, 314] This process has been proposed to deteriorate operational stability by reducing charge carrier mobility and disrupting energy-level alignment. Furthermore, molecular dimerization on the perovskite surface compromises the uniformity of the PCBM layer. Therefore, suppressing PCBM dimer formation on the perovskite surface is key to improving both stability and scalability. Liang et al. developed a molecular dopant, 2,3,5,6-tetrafluoro-4-iodobenzoic acid (FIBA), to reorient PCBM molecules by π-π stacking and hydrogen bonding, thereby suppressing dimer formation and improving film uniformity.[315] This strategy ultimately reduces efficiency losses during scale-up (21.3% of 764 cm^2) and enhances operational device stability. The FIBA-based devices retained 93% of its initial PCE after 1,500 hours (85°C, N_2; ISOS-L-2I), and 85% of its initial PCE after 2,000 hours of aging (85°C, 85% RH; ISOS-L-3).

3.4.2 Advancing Fullerene-free ETLs

Despite these advancements, fullerene-based ETLs still exhibit inherent drawbacks, in which the poor mechanical robustness greatly limits device durability and motivates the search for alternative electron transport materials.[98, 99] However, direct substitution with inorganic metal oxides remains challenging, as hybrid perovskites are thermally sensitive and cannot withstand the high-temperature processing typically required for metal oxide optimization. Atomic layer deposition **(**ALD)-derived SnO_2 is widely used in inverted PSCs, where its dense, uniform films protect perovskites from sputtering damage during electrode deposition. Zhu et al. introduced a simultaneous co-deposition strategy that allows for the direct formation of SnO_x/Ag electrodes without the need for fullerene layers (**Figure 11C**).[26] The ALD-SnO_x layer acts as a robust and thermally stable inorganic ETL. The resulting devices retained a certified T_{97} lifetime of 1,000 hours under MPPT (65°C; ISOS-L-2).

Fused-ring electron acceptors (FREAs) with donor-acceptor-donor architectures, along with naphthalene diimide (NDI)-based derivatives, have recently emerged as promising alternatives to fullerene ETLs.[97] Huang et al. reported two Y-type NFAs, Y-Phen and Y-CE, designed by replacing the benzothiadiazole core of Y6 with higher-polarity phenanthroline and crown ether units to improve interfacial interactions and molecular packing (**Figure 11D**).[316] These modifications promote ordered assembly on the perovskite surface and enhance charge transport. Devices using Y-CE as the ETL achieved a certified PCE of 25.59% and maintained over 90% of the initial efficiency after 1,440 hours of thermal aging. This result significantly narrows the performance gap between fullerene-free and conventional fullerene-based devices. Despite these promising efficiencies, practical challenges remain. The synthesis of Y6 typically requires up to 15 steps, with overall yields as low as ~12%[317, 318], raising concerns about scalability and cost for large-scale applications. Moreover, many FREAs, including Y6, contain electron-withdrawing end groups linked to the conjugated core through highly polarized double bonds, which are susceptible to nucleophilic attack, especially halide anions from perovskites. Consequently, their chemical stability under operational conditions remains uncertain.

Compared with complex FREAs, NDI-based materials offer a more scalable alternative for fullerene-free ETLs due to their simpler synthesis (~3 steps, ~70% yield), low cost, and good thermal and photochemical stability.[319, 320] NDI films show electron mobilities (~10^{-4} $cm^2 \cdot V^{-1} \cdot s^{-1}$) comparable to thermally evaporated C_{60}, and minimal visible absorption, reducing parasitic losses. Their tunable LUMO levels and chemical robustness make NDIs promising candidates for durable, large-scale perovskite photovoltaics. However, tuning the electronic structure of NDIs remains challenging, as donor substitution raises the HOMO level and narrows the optical gap, thereby increasing parasitic

absorption. In addition, the ultrathin (~2 nm) layers required for optimal performance are difficult to control uniformly over large areas, limiting scalability. Charge transport in NDI films is also anisotropic and highly sensitive to deposition conditions and molecular orientation. Developing vapor-deposition-compatible NDIs or combining vapor deposition with post-treatment processes may improve film uniformity and charge transport facilitating for scalable fabrication.[321]

View Article Online
DOI: 10.1039/D5EE07642K

3.4.3 Novel Buffer Layer

The diffusion or migration of mobile ions from the perovskite absorber through the top ETL, leading to their accumulation at the metal electrode interface, can corrode the metal electrodes. Furthermore, the migration of metal atoms from the electrode into the underlying ETL and perovskite layers presents another critical concern for long-term stability.[322] Inserting a bilayer buffer of BCP and bismuth (Bi) between the ETL and the metal electrode effectively blocks moisture penetration into the perovskite and shields the metal electrode from iodine-induced corrosion (**Figure 11E**).[323] Devices incorporating this Bi interlayer retained 95% and 97% of their initial PCEs after 500 hours of thermal aging at 85°C and light soaking, respectively. More recently, an amorphous ZrN_x barrier layer has been introduced to further suppress ion diffusion and mitigate metal electrode corrosion.[324] The PSCs maintained 88% of their initial efficiency after 1,500 hours of continuous MPPT (N_2), along with strong thermal stability, retaining 90% efficiency after 1,000 hours at 85°C.

Direct contact between metal electrodes and ETLs can lead to the formation of Schottky contacts, causing detrimental charge accumulation. Incorporating a buffer layer, such as BCP, is often necessary to mitigate this issue, as it promotes ohmic contact and reduces charge accumulation at the interface. However, the organic BCP layer is relatively unstable, posing risks to the device's long-term thermal stability. To overcome this limitation, a chemically stable and multifunctional buffer material, ytterbium oxide (YbO_x), was designed using scalable thermal evaporation deposition **(Figure 11F)**.[28] When subjected to the ISOS-L-3 accelerated aging conditions (85°C, 50% RH), encapsulated devices incorporating YbO_x exhibit markedly enhanced device stability.

In perovskite solar modules with series-connected subcells, the metal electrodes directly contact the perovskite layer at the P2 scribe lines.[325, 326] This direct interface raises concerns regarding the long-term stability of the modules, as chemical reactions and iodide diffusion between the metal and perovskite materials may occur. To address this issue, introducing additional barrier layers, such as 2D graphitic carbon nitride nanosheets or ALD-deposited SnO_x, at the interconnection regions has been proven as effective approaches.[325, 327] A low-temperature solution-processing approach was developed to achieve stable and efficient perovskite modules by incorporating low-dimensional diffusion barriers (**Figure 11G**). This method significantly mitigated the additional degradation caused by diffusion in perovskite solar modules. Tan et al. developed a thin, conformal diffusion barrier (CDB) of SnO_x, deposited after P2 scribing (**Figure 11H**).[327] This conductive CDB effectively suppressed halide-metal interdiffusion and acted as a lateral barrier between interconnected subcells, thereby preventing direct interaction between the metal electrodes and perovskite layers. These advantages allowed the all-perovskite tandem modules to maintain their initial PCE even after 500 hours of MPPT.

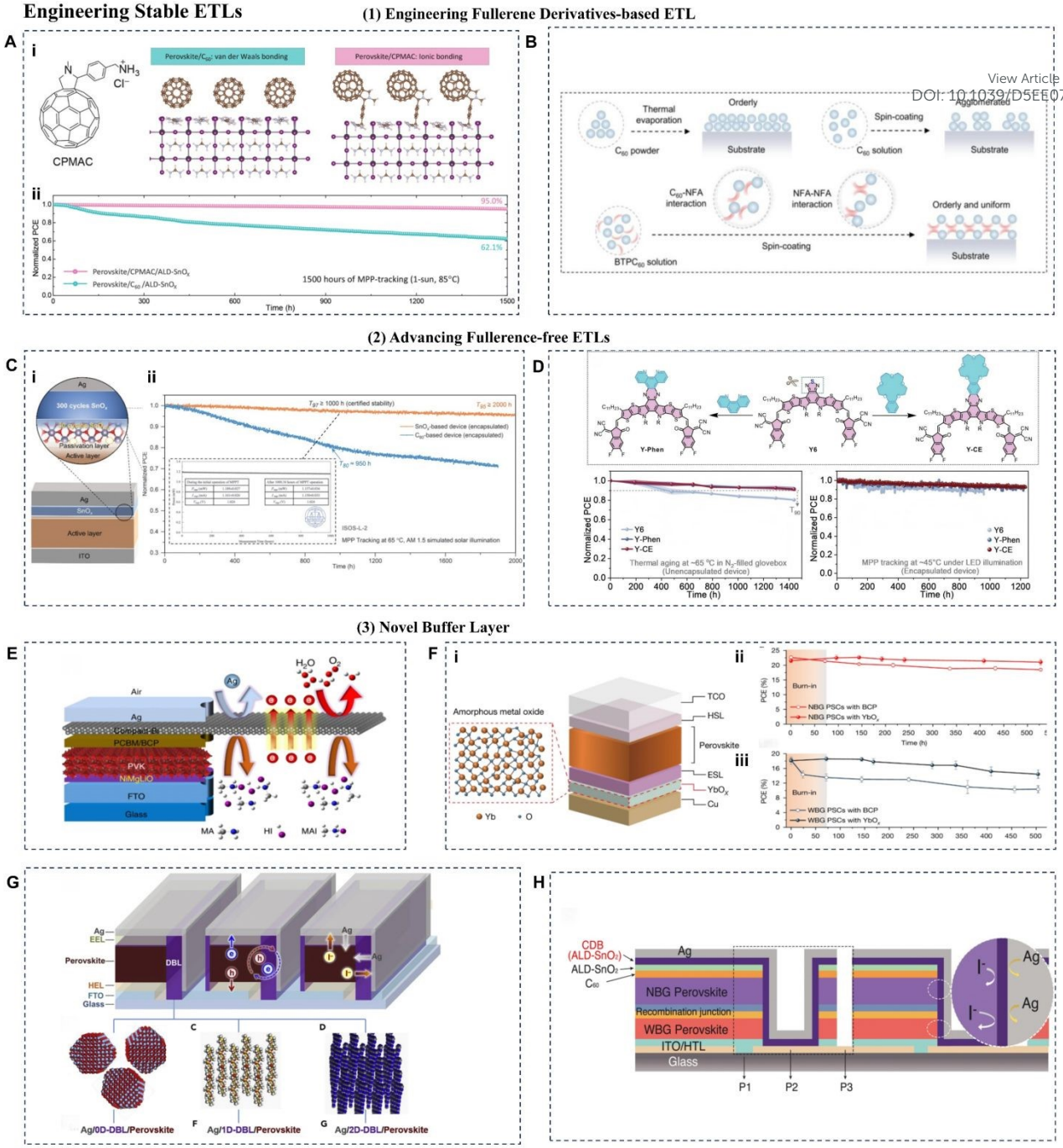

Figure 11. Engineering Stable ETLs. (A) (Ai) Comparison of C_{60} and CPMAC on their different interactions with the perovskite surface. (Aii) Comparison of operational stability of devices under 1-sun MPPT (65°C, N_2; ISOS-L-1).[308] Copyright 2025, Science Press. (B) Schematic diagram of molecular packing during C_{60} and $BTPC_{60}$ film preparation.[310] Copyright 2024, Wiley-VCH. (C) (Ci) Schematic illustration of the device structure with SnO_x ETL. (Cii) Certified operational stability of devices (65°C; ISOS-L-2).[26] Copyright 2024, Science Press. (D) (Di) Intrinsic stability of unencapsulated devices aged at 65°C in a N_2-filled glovebox. (Dii) MPPT of encapsulated devices at ~45°C under LED illumination.[316] Copyright 2015, Nature Publishing Group. (E) Schematic diagram of the device structure, the Bi interlayer has a superior shielding capability, prohibiting both inward and outward permeation.[323] Copyright 2019, Nature Publishing Group. (F) (Fi) Schematic of the device configuration of a typical p-i-n PSCs with the YbO_x buffer layer. (Fii) Variations of the PCEs of the encapsulated NBG-containing PSCs (top) and WBG-containing PSCs (bottom) with the BCP or YbO_x buffer layer aged in an N_2-filled glovebox under 85°C, dark.[28] Copyright 2023, Nature Publishing Group. (G) Schematic illustration of diffusion barriers within perovskite modules.[325] Copyright 2019, Cell Press. (H) Schematic diagram of the structure of the series-connected all-perovskite tandem module with CDB to prevent ion diffusion.[327] Copyright 2022, Science Press.

Table 4. Stability development of inverted single-junction solar cells by engineering robust ETL.

Year	Strategy	PCE (certified)	Stability Improvement Mechanism	Stability for devices	
				Operation	Thermal/Light/Humidity
Engineering Fullerene Derivatives-based ETL					
2025	C_{60}-based ionic salt ETL[308]	26.1	CH_2-NH_3^+ head groups improve interface and molecular packing	$T_{97.6}$~2,100 h (65°C, N_2); T_{95}~1,500 h (85°C, N_2)	/
2025	Magnetic endohedral metallofullerene Nd@C_{82} ETL[312]	26.78 (26.29)	Utrafast electron extraction and in-situ interfacial encapsulation	T_{82}~2,500 h (ISOS-L-3; 65°C)	T_{95}~1,750 h (ISOS-D-2I; 85°C); Almost no degradation >1,000 h (ISOS-D-3; 85°C, 85% RH)
2025	Molecular dopants 2,3,5,6-tetrafluoro-4-iodobenzoic acid (FIBA) in PCBM[104]	26.4	Reorient PCBM molecules to suppress PCBM dimer formation	T_{98}~2,200 h (ISOS-L-1I); T_{93}~1,500 h (ISOS-L-2I); T_{85}~2,000 h (ISOS-L-3; 85°C)	T_{97}~1,000 h (ISOS-D-2I; 85°C)
2026	Crosslinked siloxane matrix in PCBM[328]	26.39 (26.27)	Suppress thermally induced PCBM aggregation	T_{90} > 800 hours (ISOS-L-3; 85°C)	/
Advancing Fullerene-free ETLs					
2024	ALD-SnO_x ETL[26]	25.1	Durable inorganic fullerene-free	Certified T_{97}>1,000 h (ISOS-L-2)	/
2025	Supramolecular-force-driven NFA ETL (Y-type NFAs)[316]	25.59	Supramolecular interactions promote ordered ETL assembly on perovskite	T_{90}>1,200 h (45°C, N_2)	T_{90}>1,440 h (65°C, N_2)
Novel Buffer Layer					
2023	ZrN_x barrier[324]	23.1	Reduced amorphous-crystalline density, suppressing ion-metal inter-diffusion by dense structure	T_{88}~1,500 h	T_{90}~1,000 h (85°C, N_2)
2024	Thermally evaporated YbO_x buffer layer[28]	25.2 (25.09)	Intrinsically stable, multifunctional material replacing BCP	T_{97}~1,000 h (ISOS-L-3; 85°C, 50% RH)	T_{98}~500 h (85°C, Dark)

4. Outlook and Challenges

The trajectory of inverted perovskite solar cells (PSCs) is at a pivotal juncture. Although record-breaking PCEs have been achieved, the paramount challenge for their commercial viability remains bridging the substantial operational stability gap compared to established technologies like crystalline silicon. The path forward is unequivocally centered on interface. Future research must adopt a holistic and co-optimization approach, moving beyond the singular focus on PCE. The following key directions are critical:

(1) **Deepening the Fundamental Understanding of Interfacial Crosstalk**: A molecular-level understanding of interactions dynamics at the perovskite/CTM interface during aging process is required. This includes:

i. How functional groups in CTMs passivate or activate specific defects.

ii. How energy-level alignment and interface-mediated charge extraction kinetics influence the ion migration and photochemical reactions.

iii. The bidirectional degradation pathways: not just how CTMs affect perovskite stability, but also how perovskite decomposition products corrode or degrade the transport layers.

iv. In-situ/operando characterization of the dynamics change at interfaces would be highly beneficial. Key questions remain regarding whether the selected passivators and interfacial structures maintain stability under relevant stress conditions, such as elevated temperatures (e.g., 85°C) and thermal cycling (ISOS-T protocols). Furthermore, the chemical stability, molecular binding configurations, and defect passivation capabilities of these interfacial layers may evolve under coupled stresses of heat, illumination, and electrical bias. Advanced operando characterizations such as photoelectron microscopy and synchrotron radiation, are required to monitor dynamic interfacial reactions, ion migration, and structural reconstruction in real time, enabling a deeper understanding of degradation pathways and guiding the rational design of more stable interfaces.

(2) Thin Film Growth Control for Universal Stability. We have learned that the metal oxide (MO)/SAM/perovskite interface critically governs the stability of p-i-n structured devices. In part this is related to robust anchoring of SAMs on the MO substrate during both deposition and operational processes, in part it is related to the effective coordination at the SAM/perovskite interface for defect passivation and, crucially, crystallization regulation. Treatment of the perovskite thin film surface, interfaced with the ETL, also seems to be unavoidable, and as for the buried interface with the substrate, a trade-off between stability (chemical and mechanical) and efficiency must be found. Then, the need to develop interfacial engineering strategies that are effective across the wide range of bandgaps required for tandem devices and different perovskite compositions must be compromised with the awareness that a "one-size-fits-all" solution is unlikely. As a result, so far, despite remarkable efficiency advances, the operational stability of tandem devices still lags behind that achieved in single-junction counterparts. In tandem architecture, the interfacial landscape is inherently more complex than in single-junction devices, as stability must be simultaneously ensured for both subcells and the interconnecting layers.

Said this, there is an interesting message that coming across the last reports on the development of perovskite thin films for solar cells, but not only, and it points to the crystallization of the perovskite thin film. Despite the massive research effort, still, the control of the crystallization process, both solvent and vacuum mediated, is poor if compared with established technologies. Open questions regard the role of precursors inclusions in thin films, the impact of precursors purity and how they are responsible for the need for specific passivation strategy. The open question is: are all the passivation strategies proposed really needed if we could gain more in-depth understanding of the actual thin film composition and crystallization?

(3) Beyond current charge extraction layers. The introduction of SAMs to modulate the HTL/perovskites interface has driven the advancement in the p-i-n structured PSCs, while the perovskites/ETL is stuck. The capability of electronic doping of the device contacts may result in a universal solution in the simplification of the device architecture. A few proof-of-concepts have been reported based on charge transfer concept through molecular systems.[329, 330] The control of substitutional doping focused on the metal cation, if successful, may represent a game changer approach.

(4) Challenge faced from laboratory cells to scalable modules: Despite substantial stability gains in small-area devices, translating interfacial strategies to large-area modules remains challenging. Perovskite modules experience complex, field-specific degradation mechanisms distinct from those in conventional photovoltaics. Even small-area modules typically lose more than 20% of their efficiency annually, whereas degradation rates below 0.5% per year are required to match the operational stability of silicon photovoltaics.[1, 331, 332] The following points highlight several key considerations when translating laboratory-scale devices to modules.

i. SAMs often suffer from limited reproducibility and non-uniform coverage on large substrates. During P1 scribing, exposed glass regions create wettability contrasts with ITO, so hydrophobic SAM deposition can lead to non-uniform perovskite coating, resulting in pinholes and electrical shunts between sub-cells. Hence, more robust and reliable SAMs must be developed to enable stable perovskite modules.

ii. Surface passivation strategies based on 2D perovskites typically rely on precisely controlled solution processing—often achieved through dynamic spin-coating—which is difficult to replicate with scalable deposition. Vapour[333-335] and vacuum deposition[170, 336] approaches have therefore been explored as scalable alternatives. Additionally, the use of ammonium cations that do not form 2D perovskites may broaden the processing window for scalable solution processing, offering a promising route toward high-efficiency large-area perovskite modules.[129, 337, 338]

iii. Many surface functional layers rely on spin-coating, posing challenges for scalable manufacturing, while the high cost of some functional materials further limits module deployment. Solvent-free solid-phase passivation offers a promising scalable alternative compatible with large-area processing.[339, 340] Future efforts should focus on translating insights from small-area devices to identify chemically stable passivators with durable interfacial interactions for module-level applications.

iv. Fully vacuum-processed PSCs have recently emerged as a promising route toward scalable manufacturing.[341-346] The deposition of high-quality interfacial layers by vacuum techniques is therefore critical for enabling efficient and scalable modules. Beyond technological advances in vacuum-processing, further studies are required to

understand the long-term stability and interfacial evolution of vacuum-deposited layers under operational conditions.

In conclusion, the future of stable inverted PSCs depends on designing and integrating interfaces that are not merely electrically functional but are also chemically inert, physically robust, and actively protective. By shifting the paradigm from interface engineering for performance to interface stewardship for longevity, the field can make the critical leap from laboratory research to sustainable commercial deployment.

View Article Online
DOI: 10.1039/D5EE07642K

Acknowledgement

The authors acknowledge the support from the projects supported by the Cariplo EDO project (No. EPFDO0195), HORIZON Grants VALHALLA (No. 101082176) and the Italian Ministry of Environment and Energy Security in the framework of the Project GoPV (CSEAA_00011) for Research on the Electric System.

Conflict of Interest

The authors declare no conflict of interest.

Reference

1. N.-G. Park, H. J. Snaith and T. Miyasaka, *Nature Reviews Clean Technology*, 2026, **2**, 6-7.
2. L. A. Castriotta, *ACS Energy Letters*, 2026, **11**, 2378-2381.
3. J. Han, K. Park, S. Tan, Y. Vaynzof, J. Xue, E. W.-G. Diau, M. G. Bawendi, J.-W. Lee and I. Jeon, *Nature Reviews Methods Primers*, 2025, **5**, 3.
4. L. A. Castriotta, *ACS Energy Letters*, 2026, **3**, 2378-2381.
5. M. V. Khenkin, E. A. Katz, A. Abate, G. Bardizza, J. J. Berry, C. Brabec, F. Brunetti, V. Bulović, Q. Burlingame, A. Di Carlo, R. Cheacharoen, Y.-B. Cheng, A. Colsmann, S. Cros, K. Domanski, M. Dusza, C. J. Fell, S. R. Forrest, Y. Galagan, D. Di Girolamo, M. Grätzel, A. Hagfeldt, E. von Hauff, H. Hoppe, J. Kettle, H. Köbler, M. S. Leite, S. Liu, Y.-L. Loo, J. M. Luther, C.-Q. Ma, M. Madsen, M. Manceau, M. Matheron, M. McGehee, R. Meitzner, M. K. Nazeeruddin, A. F. Nogueira, Ç. Odabaşı, A. Osherov, N.-G. Park, M. O. Reese, F. De Rossi, M. Saliba, U. S. Schubert, H. J. Snaith, S. D. Stranks, W. Tress, P. A. Troshin, V. Turkovic, S. Veenstra, I. Visoly-Fisher, A. Walsh, T. Watson, H. Xie, R. Yıldırım, S. M. Zakeeruddin, K. Zhu and M. Lira-Cantu, *Nature Energy*, 2020, **5**, 35-49.
6. Q. Jiang, J. Tong, Y. Xian, R. A. Kerner, S. P. Dunfield, C. Xiao, R. A. Scheidt, D. Kuciauskas, X. Wang, M. P. Hautzinger, R. Tirawat, M. C. Beard, D. P. Fenning, J. J. Berry, B. W. Larson, Y. Yan and K. Zhu, *Nature*, 2022, **611**, 278-283.
7. G. Li, Z. Zhang, B. Agyei-Tuffour, L. Wu, T. W. Gries, K. Prashanthan, L. Frohloff, A. Musiienko, J. Li, R. Zhu, L. J. F. Hart, L. Wang, Z. Li, B. Hou, N. Koch, M. Saba, P. R. F. Barnes, J. Nelson, P. J. Dyson, M. K. Nazeeruddin, M. Li and A. Abate, *Nature Photonics*, 2026, **20**, 55-62.
8. C. Liu, Y. Yang, H. Chen, J. Xu, A. Liu, A. S. R. Bati, H. Zhu, L. Grater, S. S. Hadke, C. Huang, V. K. Sangwan, T. Cai, D. Shin, L. X. Chen, M. C. Hersam, C. A. Mirkin, B. Chen, M. G. Kanatzidis and E. H. Sargent, *Science*, 2023, **382**, 810-815.
9. S. M. Park, M. Wei, J. Xu, H. R. Atapattu, F. T. Eickemeyer, K. Darabi, L. Grater, Y. Yang, C. Liu, S. Teale, B. Chen, H. Chen, T. Wang, L. Zeng, A. Maxwell, Z. Wang, K. R. Rao, Z. Cai, S. M. Zakeeruddin, J. T. Pham, C. M. Risko, A. Amassian, M. G. Kanatzidis, K. R. Graham, M. Grätzel and E. H. Sargent, *Science*, 2023, **381**, 209-215.
10. H. Chen, C. Liu, J. Xu, A. Maxwell, W. Zhou, Y. Yang, Q. Zhou, A. S. R. Bati, H. Wan, Z. Wang, L. Zeng, J. Wang, P. Serles, Y. Liu, S. Teale, Y. Liu, M. I. Saidaminov, M. Li, N. Rolston, S. Hoogland, T. Filleter, M. G. Kanatzidis, B. Chen, Z. Ning and E. H. Sargent, *Science*, 2024, **384**, 189-193.
11. Y. Yang, H. Chen, C. Liu, J. Xu, C. Huang, C. D. Malliakas, H. Wan, A. S. R. Bati, Z. Wang, R. P. Reynolds, I. W. Gilley, S. Kitade, T. E. Wiggins, S. Zeiske, S. Suragtkhuu, M. Batmunkh, L. X. Chen, B. Chen, M. G. Kanatzidis and E. H. Sargent, *Science*, 2024, **386**, 898-902.

12. H. Zai, P. Yang, J. Su, R. Yin, R. Fan, Y. Wu, X. Zhu, Y. Ma, T. Zhou, W. Zhou, Y. Zhang, Z. Huang, Y. Jiang, N. Li, Y. Bai, C. Zhu, Z. Huang, J. Chang, Q. Chen, Y. Zhang and H. Zhou, *Science*, 2025, **387**, 186-192.
13. Y. Yang, S. Cheng, X. Yang, M. Li, X. Zhu, Z. Yang, Y. Zheng, Y. Liu, Q. Lin, N. Yan, S. Yuan and Z. Wang, *Science*, 2026, **391**, 926-930.
14. R. Azmi, D. S. Utomo, B. Vishal, S. Zhumagali, P. Dally, A. M. Risqi, A. Prasetio, E. Ugur, F. Cao, I. F. Imran, A. A. Said, A. R. Pininti, A. S. Subbiah, E. Aydin, C. Xiao, S. I. Seok and S. De Wolf, *Nature*, 2024, **628**, 93-98.
15. J. Zhou, Y. Luo, R. Li, L. Tian, K. Zhao, J. Shen, D. Jin, Z. Peng, L. Yao, L. Zhang, Q. Liu, S. Zhang, L. Jin, S. Chu, S. Wang, Y. Tian, J. Xu, X. Zhang, P. Shi, X. Wang, W. Fan, X. Sun, J. Sun, L.-Z. Chen, G. Wu, W. Shi, H.-F. Wang, T. Deng, R. Wang, D. Yang and J. Xue, *Nature Chemistry*, 2025, **17**, 564-570.
16. J. Du, J. Chen, B. Ouyang, A. Sun, C. Tian, R. Zhuang, C. Chen, S. Liu, Q. Chen, Z. Li, X. Wu, J. Cai, Y. Zhao, R. Li, T. Xue, T. Cen, K. Zhao and C.-C. Chen, *Energy & Environmental Science*, 2025, **18**, 3196-3210.
17. Z. Xu, X. Sun, W. Hui, Q. Wang, P. Xu, W. Tang, H. Hu, L. Song, X. Xu, Y. Wu and Q. Peng, *Angewandte Chemie International Edition*, 2025, **64**, e202503008.
18. Z. Li, X. Sun, X. Zheng, B. Li, D. Gao, S. Zhang, X. Wu, S. Li, J. Gong, J. M. Luther, Z. a. Li and Z. Zhu, *Science*, 2023, **382**, 284-289.
19. K. Zhao, Q. Liu, L. Yao, C. Değer, J. Shen, X. Zhang, P. Shi, Y. Tian, Y. Luo, J. Xu, J. Zhou, D. Jin, S. Wang, W. Fan, S. Zhang, S. Chu, X. Wang, L. Tian, R. Liu, L. Zhang, I. Yavuz, H.-f. Wang, D. Yang, R. Wang and J. Xue, *Nature*, 2024, **632**, 301-306.
20. S. Liu, J. Li, W. Xiao, R. Chen, Z. Sun, Y. Zhang, X. Lei, S. Hu, M. Kober-Czerny, J. Wang, F. Ren, Q. Zhou, H. Raza, Y. Gao, Y. Ji, S. Li, H. Li, L. Qiu, W. Huang, Y. Zhao, B. Xu, Z. Liu, H. J. Snaith, N.-G. Park and W. Chen, *Nature*, 2024, **632**, 536-542.
21. W. Jiang, G. Qu, X. Huang, X. Chen, L. Chi, T. Wang, C.-T. Wong, F. R. Lin, C. Yang, Q. Jiang, S. Wu, J. Zhang and A. K. Y. Jen, *Nature*, 2025, **646**, 95-101.
22. C. Luo, Q. Zhou, K. Wang, X. Wang, J. He, P. Gao, C. Zhan, Z. Bi, W. Li, Y. Ma, W. Chen, Y. Hou, Z. Liu and Q. Zhao, *Nature Materials*, 2025, **24**, 1265-1272.
23. Q. Tan, Z. Li, G. Luo, X. Zhang, B. Che, G. Chen, H. Gao, D. He, G. Ma, J. Wang, J. Xiu, H. Yi, T. Chen and Z. He, *Nature*, 2023, **620**, 545-551.
24. C. Tian, A. Sun, J. Chen, R. Zhuang, C. Chen, J. Zheng, S. Liu, J. Du, Q. Chen, L. Cai, S. Han, F. Tian and C.-C. Chen, *Nature Photonics*, 2026, **20**, 287-295.
25. S. You, H. Zhu, Z. Shen, X. Wang, B. Shao, Q. Wang, J. Lu, Y. Yuan, B. D. Dou, E. M. Sanehira, T. Russell, A. Lorenz, Y. Dong, L. Chen, M. Casareto, N. Rolston, M. C. Beard, J. J. Berry, M. Freitag, Y. Yan, O. M. Bakr and K. Zhu, *Science*, 2025, **388**, 964-968.
26. D. Gao, B. Li, Q. Liu, C. Zhang, Z. Yu, S. Li, J. Gong, L. Qian, F. Vanin, K. Schutt, M. A. Davis, A. F. Palmstrom, S. P. Harvey, N. J. Long, J. M. Luther, X. C. Zeng and Z. Zhu, *Science*, 2024, **386**, 187-192.
27. Y. Lin, Z. Lin, S. Lv, Y. Shui, W. Zhu, Z. Zhang, W. Yang, J. Zhao, H. Gu, J. Xia, D. Wang, F. Du, A. Zhu, J. Liu, H. Cai, B. Wang, N. Zhang, H. Wang, X. Liu, T. Liu, C. Kong, D. Zhou, S. Chen, Z. Yang, T. Li, W. Ma, G. Fang, L. Echegoyen, G. Xing, S. Yang, T. Yang, W. Cai, M. Li, W. Huang and C. Liang, *Nature*, 2025, **642**, 78-84.
28. P. Chen, Y. Xiao, J. Hu, S. Li, D. Luo, R. Su, P. Caprioglio, P. Kaienburg, X. Jia, N. Chen, J. Wu, Y. Sui, P. Tang, H. Yan, T. Huang, M. Yu, Q. Li, L. Zhao, C.-H. Hou, Y.-W. You, J.-J. Shyue, D. Wang, X. Li, Q. Zhao, Q. Gong, Z.-H. Lu, H. J. Snaith and R. Zhu, *Nature*, 2024, **625**, 516-522.
29. B. Li and W. Zhang, *Communications Materials*, 2022, **3**, 65.
30. Q. Jiang and K. Zhu, *Nature Reviews Materials*, 2024, **9**, 399-419.
31. D. Zhao, M. Sexton, H.-Y. Park, G. Baure, J. C. Nino and F. So, *Advanced Energy Materials*, 2015, **5**, 1401855.
32. J.-Y. Jeng, Y.-F. Chiang, M.-H. Lee, S.-R. Peng, T.-F. Guo, P. Chen and T.-C. Wen, *Advanced Materials*, 2013, **25**, 3727-3732.
33. L. V. Kayser and D. J. Lipomi, *Advanced Materials*, 2019, **31**, 1806133.
34. Y.-C. Chin, M. Daboczi, C. Henderson, J. Luke and J.-S. Kim, *ACS Energy Letters*, 2022, **7**, 560-568.
35. G. Kapil, T. Bessho, Y. Sanehira, S. R. Sahamir, M. Chen, A. K. Baranwal, D. Liu, Y. Sono, D. Hirotani, D. Nomura, K. Nishimura, M. A. Kamarudin, Q. Shen, H. Segawa and S. Hayase, *ACS Energy Letters*, 2022, **7**, 966-974.
36. D. He, P. Chen, J. A. Steele, Z. Wang, H. Xu, M. Zhang, S. Ding, C. Zhang, T. Lin, F. Kremer, H. Xu, M. Hao and L. Wang, *Nature Nanotechnology*, 2025, **20**, 779-786.

37. Y. Zhang, C. Li, H. Zhao, Z. Yu, X. Tang, J. Zhang, Z. Chen, J. Zeng, P. Zhang, L. Han and H. Chen, *Nature Communications*, 2024, **15**, 6887.
38. Y. Zhang, Y. Pi, J. Guo, H. Liu, R. Yang, S. Ren, C. Ding, Y. Li, C. Chen and D. Zhao, *Journal of Materials Chemistry C*, 2025, **13**, 21248-21274.
39. W. Gao, F. Yang, Z. Wang, Y. Lan, R. Nie and C. Ran, *Advanced Materials*, 2026, **38**, e21789.
40. J. Wang, S. Hu, H. Zhu, S. Liu, Z. Zhang, R. Chen, J. Wang, C. Shi, J. Zhang, W. Liu, X. Lei, B. Liu, Y. Pan, F. Ren, H. Raza, Q. Zhou, S. Li, L. Qiu, G. Zheng, X. Qin, Z. Zhao, S. Yang, N. Li, J. Li, A. Wakamiya, Z. Liu, H. J. Snaith and W. Chen, *Nature Communications*, 2025, **16**, 4917.
41. J. Zhu, Y. Xu, Y. Luo, J. Luo, R. He, C. Wang, Y. Wang, K. Wei, Z. Yi, Z. Gao, J. Wang, J. You, Z. Zhang, H. Lai, S. Ren, X. Liu, C. Xiao, C. Chen, J. Zhang, F. Fu and D. Zhao, *Science Advances*, 2024, **10**, eadl2063.
42. W. Zhang, L. Huang, H. Guan, W. Zheng, Z. Li, H. Cui, S. Zhou, J. Liang, G. Li, T. Wang, P. Qin, W. Ke and G. Fang, *Energy & Environmental Science*, 2023, **16**, 5852-5862.
43. J. Zhou, H. Qiu, T. Wen, Z. He, C. Zou, Y. Shi, L. Zhu, C.-C. Chen, G. Liu, S. Yang, F. Liu and Z. Yang, *Advanced Energy Materials*, 2023, **13**, 2300968.
44. D. He, K. Liu, Z. Li, X. Zhang, H. Gao, Z. Niu, T. Cheng, G. Ma, J. Wang, F. Lamberti and Z. He, *Advanced Functional Materials*, 2024, **34**, 2411750.
45. X. Sun, H. Wu, Z. Li, R. Zhu, G. Li, Z. Su, J. Zhang, X. Gao, J. Pascual, A. Abate and M. Li, *Angewandte Chemie International Edition*, 2024, **63**, e202409330.
46. J. Zhu, Y. Luo, R. He, C. Chen, Y. Wang, J. Luo, Z. Yi, J. Thiesbrummel, C. Wang, F. Lang, H. Lai, Y. Xu, J. Wang, Z. Zhang, W. Liang, G. Cui, S. Ren, X. Hao, H. Huang, Y. Wang, F. Yao, Q. Lin, L. Wu, J. Zhang, M. Stolterfoht, F. Fu and D. Zhao, *Nature Energy*, 2023, **8**, 714-724.
47. J. Roe, J. G. Son, S. Park, J. Seo, T. Song, J. Kim, S. O. Oh, Y. Jo, Y. Lee, Y. S. Shin, H. Jang, D. Lee, D. Yuk, J. G. Seol, Y. S. Kim, S. Cho, D. S. Kim and J. Y. Kim, *ACS Nano*, 2024, **18**, 24306-24316.
48. C. Liu, R. Lin, Y. Wang, H. Gao, P. Wu, H. Luo, X. Zheng, B. Tang, Z. Huang, H. Sun, S. Zhao, Y. Guo, J. Wen, F. Fan and H. Tan, *Angewandte Chemie International Edition*, 2023, **62**, e202313374.
49. S. Lee, J. Ryu, D.-G. Lee, P. Pandey, C.-M. Oh, I.-W. Hwang, S. Cho, S. Yoon, J.-Y. Lee and D.-W. Kang, *Energy & Environmental Science*, 2024, **17**, 8140-8150.
50. A. S. R. Bati, C. Liu, I. W. Gilley, C. B. Musgrave, A. Maxwell, J. A. Steele, Y. Yang, H. Chen, H. Wan, J. Xu, E. Solano, R. Zhang, C. Huang, B. Rehl, N. Lempesis, V. Carnevali, A. Vezzosi, L. Zeng, L. Grater, M. Li, N. Rolston, D. Choi, V. Sláma, U. Rothlisberger, L. Wang, W. A. Goddard, M. G. Kanatzidis, B. Chen, O. M. Bakr and E. H. Sargent, *Joule*, 2025, **9**, 102047.
51. J. Zhu, X. Huang, Y. Luo, W. Jiao, Y. Xu, J. Wang, Z. Gao, K. Wei, T. Ma, J. You, J. Jin, S. Wu, Z. Zhang, W. Liang, Y. Wang, S. Ren, C. Wang, C. Chen, J. Zhang and D. Zhao, *Nature Communications*, 2025, **16**, 240.
52. W. Peng, K. Mao, F. Cai, H. Meng, Z. Zhu, T. Li, S. Yuan, Z. Xu, X. Feng, J. Xu, M. D. McGehee and J. Xu, *Science*, 2023, **379**, 683-690.
53. Y. Yao, C. Cheng, C. Zhang, H. Hu, K. Wang and S. De Wolf, *Advanced Materials*, 2022, **34**, 2203794.
54. S. Chen, X. Dai, S. Xu, H. Jiao, L. Zhao and J. Huang, *Science*, 2021, **373**, 902-907.
55. X. Sun, Z. Li, X. Yu, X. Wu, C. Zhong, D. Liu, D. Lei, A. K.-Y. Jen, Z. a. Li and Z. Zhu, *Angewandte Chemie International Edition*, 2021, **60**, 7227-7233.
56. R. Chen, S. Liu, X. Xu, F. Ren, J. Zhou, X. Tian, Z. Yang, X. Guanz, Z. Liu, S. Zhang, Y. Zhang, Y. Wu, L. Han, Y. Qi and W. Chen, *Energy & Environmental Science*, 2022, **15**, 2567-2580.
57. A. Magomedov, A. Al-Ashouri, E. Kasparavičius, S. Strazdaite, G. Niaura, M. Jošt, T. Malinauskas, S. Albrecht and V. Getautis, *Advanced Energy Materials*, 2018, **8**, 1801892.
58. E. Yalcin, M. Can, C. Rodriguez-Seco, E. Aktas, R. Pudi, W. Cambarau, S. Demic and E. Palomares, *Energy & Environmental Science*, 2019, **12**, 230-237.
59. Q. Zhou, G. Huang, J. Wang, T. Miao, R. Chen, X. Lei, E. Xu, S. Liu, H. Zhu, Z. Tan, C. Shi, X. Liu, Q. Wang, J. Li, Y. Chen, Q. Chen, Y. Shen, M. Sui, Y. Lu, Z. Liu and W. Chen, *Nature Energy*, 2025, **10**, 1371-1381.
60. Z. Xiong, Q. Zhang, K. Cai, H. Zhou, Q. Song, Z. Han, S. Kang, Y. Li, Q. Jiang, X. Zhang and J. You, *Science*, 2025, **390**, 638-642.

61. H. Lu, X. Zhuang, J. Ding, Z. Zhang, M. Li, C. Li, W. Wu, M. Lu, H. Liu, Z. Lin, W. Feng, J. Chen, J.-X. Tang and C. Chen, *Advanced Materials*, 2026, **38**, e17596.
62. E. Li, C. Liu, H. Lin, X. Xu, S. Liu, S. Zhang, M. Yu, X.-M. Cao, Y. Wu and W.-H. Zhu, *Advanced Functional Materials*, 2021, **31**, 2103847.
63. P. Thissen, M. Valtiner and G. Grundmeier, *Langmuir*, 2010, **26**, 156-164.
64. R. Luschtinetz, J. Frenzel, T. Milek and G. Seifert, *The Journal of Physical Chemistry C*, 2009, **113**, 5730-5740.
65. A. Al-Ashouri, E. Köhnen, B. Li, A. Magomedov, H. Hempel, P. Caprioglio, J. A. Márquez, A. B. Morales Vilches, E. Kasparavicius, J. A. Smith, N. Phung, D. Menzel, M. Grischek, L. Kegelmann, D. Skroblin, C. Gollwitzer, T. Malinauskas, M. Jošt, G. Matič, B. Rech, R. Schlatmann, M. Topič, L. Korte, A. Abate, B. Stannowski, D. Neher, M. Stolterfoht, T. Unold, V. Getautis and S. Albrecht, *Science*, 2020, **370**, 1300-1309.
66. C. Li, Z. Zhang, H. Zhang, W. Yan, Y. Li, L. Liang, W. Yu, X. Yu, Y. Wang, Y. Yang, M. K. Nazeeruddin and P. Gao, *Angewandte Chemie International Edition*, 2024, **63**, e202315281.
67. C. E. Puerto Galvis, D. A. González Ruiz, E. Martínez-Ferrero and E. Palomares, *Chemical Science*, 2024, **15**, 1534-1556.
68. Y. Bai, Q. Dong, Y. Shao, Y. Deng, Q. Wang, L. Shen, D. Wang, W. Wei and J. Huang, *Nature Communications*, 2016, **7**, 12806.
69. W. Wei, Y. Zhang, Q. Xu, H. Wei, Y. Fang, Q. Wang, Y. Deng, T. Li, A. Gruverman, L. Cao and J. Huang, *Nature Photonics*, 2017, **11**, 315-321.
70. Z. Dai, S. K. Yadavalli, M. Chen, A. Abbaspourtamijani, Y. Qi and N. P. Padture, *Science*, 2021, **372**, 618-622.
71. H. Xu, K. Long Wong, X. Zhou, X. Liu, H. Chen, Y. Lin, S. Xu, H. Xu, Y. He, W. Zhu, J. Yin and X. Song, *Advanced Functional Materials*, 2026, **36**, e12687.
72. M. Dubey, T. Weidner, L. J. Gamble and D. G. Castner, *Langmuir*, 2010, **26**, 14747-14754.
73. S. A. Paniagua, A. J. Giordano, O. N. L. Smith, S. Barlow, H. Li, N. R. Armstrong, J. E. Pemberton, J.-L. Brédas, D. Ginger and S. R. Marder, *Chemical Reviews*, 2016, **116**, 7117-7158.
74. X. Yu, X. Sun, Z. Zhu and Z. a. Li, *Angewandte Chemie International Edition*, 2025, **64**, e202419608.
75. A. Alberti, C. Bongiorno, E. Smecca, I. Deretzis, A. La Magna and C. Spinella, *Nature Communications*, 2019, **10**, 2196.
76. F. H. Isikgor, S. Zhumagali, L. V. T. Merino, M. De Bastiani, I. McCulloch and S. De Wolf, *Nature Reviews Materials*, 2023, **8**, 89-108.
77. S. Fu, N. Sun, H. Chen, Y. Li, Y. Li, X. Zhu, B. Feng, X. Guo, C. Yao, W. Zhang, X. Li and J. Fang, *Energy & Environmental Science*, 2025, **18**, 3305-3312.
78. Y. Yang, X. Shi, A. N. Stein, M. R. Lockett and J. Huang, *Advanced Energy Materials*, 2026, **16**, e05937.
79. C. Li, Y. Zhang, H. Zhao, J. Zhang, Z. Yu, X. Tang, Y. Wang and H. Chen, *Energy & Environmental Science*, 2026, **19**, 958-968.
80. H. Wu, J. Wu, Z. Zhang, X. Guan, L. Wang, L.-l. Deng, G. Li, A. Abate and M. Li, *Journal of the American Chemical Society*, 2025, **147**, 8004-8011.
81. L. V. Torres Merino, C. E. Petoukhoff, O. Matiash, A. S. Subbiah, C. V. Franco, P. Dally, B. Vishal, S. Kosar, D. Rosas Villalva, V. Hnapovskyi, E. Ugur, S. Shah, F. Peña Camargo, O. Karalis, H. Hempel, I. Levine, R. R. Pradhan, S. Kralj, N. Kalasariya, M. Babics, B. K. Yildirim, A. A. Said, E. Aydin, H. Bristow, S. Mannar, W. Raja, A. R. Pininti, A. Prasetio, A. Razzaq, H. Al Nasser, T. G. Allen, F. H. Isikgor, D. Baran, T. D. Anthopoulos, M. M. Masis, U. Schwingenschlögl, T. Unold, M. Stolterfoht, F. Laquai and S. De Wolf, *Joule*, 2024, **8**, 2585-2606.
82. A. R. Pininti, A. S. Subbiah, C. Deger, I. Yavuz, A. Prasetio, P. Dally, V. Hnapovskyi, A. A. Said, L. V. Torres Merino, S. Mannar, S. Zhumagali, B. Vishal, M. Marengo, A. Razzaq, M. Babics, T. G. Allen, E. Aydin, R. Azmi and S. De Wolf, *Advanced Energy Materials*, 2025, **15**, 2403530.
83. F. Di Giacomo, L. A. Castriotta, F. Matteocci and A. Di Carlo, *Advanced Energy Materials*, 2024, **14**, 2400115.
84. Z.-R. Lan, J.-Y. Shao and Y.-W. Zhong, *Molecular Systems Design & Engineering*, 2023, **8**, 1440-1455.
85. K. Choi, H. Choi, J. Min, T. Kim, D. Kim, S. Y. Son, G.-W. Kim, J. Choi and T. Park, *Solar RRL*, 2020, **4**, 1900251.
86. C. C. Boyd, R. Cheacharoen, T. Leijtens and M. D. McGehee, *Chemical Reviews*, 2019, **119**, 3418-3451.
87. S. Thampy, W. Xu and J. W. P. Hsu, *The Journal of Physical Chemistry Letters*, 2021, **12**, 8495-8506.
88. D. Di Girolamo, F. Matteocci, F. U. Kosasih, G. Chistiakova, W. Zuo, G. Divitini, L. Korte, C. Ducati, A. Di Carlo, D. Dini and A. Abate, *Advanced Energy Materials*, 2019, **9**, 1901642.

89. Y.-H. Lin, N. Sakai, P. Da, J. Wu, H. C. Sansom, A. J. Ramadan, S. Mahesh, J. Liu, R. D. J. Oliver, J. Lim, L. Aspitarte, K. Sharma, P. K. Madhu, A. B. Morales-Vilches, P. K. Nayak, S. Bai, F. Gao, C. R. M. Grovenor, M. B. Johnston, J. G. Labram, J. R. Durrant, J. M. Ball, B. Wenger, B. Stannowski and H. J. Snaith, *Science*, 2020, **369**, 96-102.
View Article Online
DOI: 10.1039/D5EE07642K
90. Y. Shao, Z. Xiao, C. Bi, Y. Yuan and J. Huang, *Nature Communications*, 2014, **5**, 5784.
91. P.-W. Liang, C.-C. Chueh, S. T. Williams and A. K.-Y. Jen, *Advanced Energy Materials*, 2015, **5**, 1402321.
92. R. Azmi, E. Ugur, A. Seitkhan, F. Aljamaan, A. S. Subbiah, J. Liu, G. T. Harrison, M. I. Nugraha, M. K. Eswaran, M. Babics, Y. Chen, F. Xu, T. G. Allen, A. u. Rehman, C.-L. Wang, T. D. Anthopoulos, U. Schwingenschlögl, M. De Bastiani, E. Aydin and S. De Wolf, *Science*, 2022, **376**, 73-77.
93. S. Chambon, A. Rivaton, J.-L. Gardette and M. Firon, *Solar Energy Materials and Solar Cells*, 2007, **91**, 394-398.
94. X. Ren, J. Wang, Y. Lin, Y. Wang, H. Xie, H. Huang, B. Yang, Y. Yan, Y. Gao, J. He, J. Huang and Y. Yuan, *Nature Materials*, 2024, **23**, 810-817.
95. A. M. Rao, P. Zhou, K.-A. Wang, G. T. Hager, J. M. Holden, Y. Wang, W.-T. Lee, X.-X. Bi, P. C. Eklund, D. S. Cornett, M. A. Duncan and I. J. Amster, *Science*, 1993, **259**, 955-957.
96. J. Liu, M. De Bastiani, E. Aydin, G. T. Harrison, Y. Gao, R. R. Pradhan, M. K. Eswaran, M. Mandal, W. Yan, A. Seitkhan, M. Babics, A. S. Subbiah, E. Ugur, F. Xu, L. Xu, M. Wang, A. u. Rehman, A. Razzaq, J. Kang, R. Azmi, A. A. Said, F. H. Isikgor, T. G. Allen, D. Andrienko, U. Schwingenschlögl, F. Laquai and S. De Wolf, *Science*, 2022, **377**, 302-306.
97. K. Schutt, M. Davis, M. Li, S. A. Johnson, D. Martinez, J. Titus, T. Leijtens, B. Martin, M. D. McGehee, S. R. Marder, N. Rolston and J. M. Luther, *ACS Energy Letters*, 2025, **10**, 6307-6317.
98. M. Li, S. Johnson, L. Gil-Escrig, M. Sohmer, C. A. Figueroa Morales, H. Kim, S. Sidhik, A. Mohite, X. Gong, L. Etgar, H. J. Bolink, A. Palmstrom, M. D. McGehee and N. Rolston, *Energy Advances*, 2024, **3**, 273-280.
99. K. Schutt, M. Davis, M. Li, S. A. Johnson, D. Martinez, J. Titus, T. Leijtens, B. Martin, M. D. McGehee, S. R. Marder, N. Rolston and J. M. Luther, *ACS Energy Letters*, 2025, **12**, 6307-6317.
100. Z. Xing, F. Liu, S.-H. Li, X. Huang, A. Fan, Q. Huang and S. Yang, *Angewandte Chemie International Edition*, 2023, **62**, e202305357.
101. N. Li, J. D. Perea, T. Kassar, M. Richter, T. Heumueller, G. J. Matt, Y. Hou, N. S. Güldal, H. Chen, S. Chen, S. Langner, M. Berlinghof, T. Unruh and C. J. Brabec, *Nature Communications*, 2017, **8**, 14541.
102. S. Pont, J. R. Durrant and J. T. Cabral, *Advanced Energy Materials*, 2019, **9**, 1803948.
103. A. Distler, T. Sauermann, H.-J. Egelhaaf, S. Rodman, D. Waller, K.-S. Cheon, M. Lee and D. M. Guldi, *Advanced Energy Materials*, 2014, **4**, 1300693.
104. Z. Liang, H. Xu, Z. Huang, X. Lei, J. Ye, Y. Zhang, P. Zhu, B. Liu, W. Chen, X. Wang, Y. Li, Y. Liao, S. Weng, Y. Tao, Y. Zhang, H. Zhang, F. Chen, J. Zeng, X. Cai, S.-U. Lee, J. Dong, W. Liu, H. Zhou, H. Lin, L. Yang, G. Xu, Y. Ding, J. Sheng, J. Li, S. Yang, B. Xu, Z. Xiao, T. Kirchartz, X. Pan and N.-G. Park, *Nature Materials*, 2026, **25**, 267-274.
105. Q. Jiang, R. Tirawat, R. A. Kerner, E. A. Gaulding, Y. Xian, X. Wang, J. M. Newkirk, Y. Yan, J. J. Berry and K. Zhu, *Nature*, 2023, **623**, 313-318.
106. X. Zheng, Y. Hou, C. Bao, J. Yin, F. Yuan, Z. Huang, K. Song, J. Liu, J. Troughton, N. Gasparini, C. Zhou, Y. Lin, D.-J. Xue, B. Chen, A. K. Johnston, N. Wei, M. N. Hedhili, M. Wei, A. Y. Alsalloum, P. Maity, B. Turedi, C. Yang, D. Baran, T. D. Anthopoulos, Y. Han, Z.-H. Lu, O. F. Mohammed, F. Gao, E. H. Sargent and O. M. Bakr, *Nature Energy*, 2020, **5**, 131-140.
107. J. Xu, C. C. Boyd, Z. J. Yu, A. F. Palmstrom, D. J. Witter, B. W. Larson, R. M. France, J. Werner, S. P. Harvey, E. J. Wolf, W. Weigand, S. Manzoor, M. F. A. M. van Hest, J. J. Berry, J. M. Luther, Z. C. Holman and M. D. McGehee, *Science*, 2020, **367**, 1097-1104.
108. J. Wang, J. Li, Y. Zhou, C. Yu, Y. Hua, Y. Yu, R. Li, X. Lin, R. Chen, H. Wu, H. Xia and H.-L. Wang, *Journal of the American Chemical Society*, 2021, **143**, 7759-7768.
109. J. Xiong, T. Ma, L. Shi, J. Zhang, Y. Xu, Q. Wang, W. Zhu, R. Xuan, Z. Yang, C. Wang, X. Li, L. Huang, X. Liu, Y. Zhu and D. Zhao, *Advanced Materials*, 2026, **n/a**, e72755.
110. X. Yang, T. Ma, H. Hu, W. Ye, X. Li, M. Li, A. Zhang, C. Ge, X. Sun, Y. Zhu, S. Yan, J. Yan, Y. Zhou, Z. a. Li, C. Chen, H. Song and J. Tang, *Nature Photonics*, 2025, **19**, 426-433.
111. X. Liao, X. Jia, W. Li, X. Lang, J. Zhang, X. Zhao, Y. Ji, Q. Du, C.-H. Kuan, Z. Ren, W. Huang, Y. Bai, K. Zhang, C. Xiao, Q. Lin, Y.-B. Cheng and J. Tong, *Nature Communications*, 2025, **16**, 1164.

112. S. Hu, J. Wang, P. Zhao, J. Pascual, J. Wang, F. Rombach, A. Dasgupta, W. Liu, M. A. Truong, H. Zhu, M. Kober-Czerny, J. N. Drysdale, J. A. Smith, Z. Yuan, G. J. W. Aalbers, N. R. M. Schipper, J. Yao, K. Nakano, S.-H. Turren-Cruz, A. Dallmann, M. G. Christoforo, J. M. Ball, D. P. McMeekin, K.-A. Zaininger, Z. Liu, N. K. Noel, K. Tajima, W. Chen, M. Ehara, R. A. J. Janssen, A. Wakamiya and H. J. Snaith, *Nature*, 2025, **639**, 93-101.

113. C. Li, L. Chen, F. Jiang, Z. Song, X. Wang, A. Balvanz, E. Ugur, Y. Liu, C. Liu, A. Maxwell, H. Chen, Y. Liu, Z. Wang, P. Xia, Y. Li, S. Fu, N. Sun, C. R. Grice, X. Wu, Z. Fink, Q. Hu, L. Zeng, E. Jung, J. Wang, S. M. Park, D. Luo, C. Chen, J. Shen, Y. Han, C. A. R. Perini, J.-P. Correa-Baena, Z.-H. Lu, T. P. Russell, S. De Wolf, M. G. Kanatzidis, D. S. Ginger, B. Chen, Y. Yan and E. H. Sargent, *Nature Energy*, 2024, **9**, 1388-1396.

114. W. H. K. Perera, T. Webb, Y. Xu, J. Zhu, Y. Zhou, G. F. Trindade, M. G. Masteghin, S. P. Harvey, S. Jenatsch, L. Dai, S. Sathasivam, T. J. Macdonald, S. J. Hinder, Y. Zhao, S. D. Stranks, D. Zhao, W. Zhang, K. D. G. I. Jayawardena, S. A. Haque and S. R. P. Silva, *Energy & Environmental Science*, 2025, **18**, 439-453.

115. A. Alsulami, L. Lanzetta, L. Huerta Hernandez, D. Rosas Villalva, A. Sharma, S. P. Gonzalez Lopez, A.-H. Emwas, A. Yazmaciyan, F. Laquai, I. Yavuz and D. Baran, *Journal of the American Chemical Society*, 2024, **146**, 22970-22981.

116. L. E. Mundt, J. Tong, A. F. Palmstrom, S. P. Dunfield, K. Zhu, J. J. Berry, L. T. Schelhas and E. L. Ratcliff, *ACS Energy Letters*, 2020, **5**, 3344-3351.

117. L. Lanzetta, T. Webb, N. Zibouche, X. Liang, D. Ding, G. Min, R. J. E. Westbrook, B. Gaggio, T. J. Macdonald, M. S. Islam and S. A. Haque, *Nature Communications*, 2021, **12**, 2853.

118. S. Fu, N. Sun, Y. Xian, L. Chen, Y. Li, C. Li, A. Abudulimu, P. N. Kaluarachchi, Z. Huang, X. Wang, K. Dolia, D. S. Ginger, M. J. Heben, R. J. Ellingson, B. Chen, E. H. Sargent, Z. Song and Y. Yan, *Joule*, 2024, **8**, 2220-2237.

119. D. Barboni and R. A. De Souza, *Energy & Environmental Science*, 2018, **11**, 3266-3274.

120. G. Y. Kim, A. Senocrate, T.-Y. Yang, G. Gregori, M. Grätzel and J. Maier, *Nature Materials*, 2018, **17**, 445-449.

121. A. A. Petrov, S. A. Fateev, Y. V. Zubavichus, P. V. Dorovatovskii, V. N. Khrustalev, I. A. Zvereva, A. V. Petrov, E. A. Goodilin and A. B. Tarasov, *The Journal of Physical Chemistry Letters*, 2019, **10**, 5776-5780.

122. J. Hu, Z. Xu, T. L. Murrey, I. Pelczer, A. Kahn, J. Schwartz and B. P. Rand, *Advanced Materials*, 2023, **35**, 2303373.

123. G. Tumen-Ulzii, C. Qin, D. Klotz, M. R. Leyden, P. Wang, M. Auffray, T. Fujihara, T. Matsushima, J.-W. Lee, S.-J. Lee, Y. Yang and C. Adachi, *Advanced Materials*, 2020, **32**, 1905035.

124. Y. Zhou, E. L. Wong, G. Folpini, M. Zanolini, J. Jiménez-López, A. Treglia and A. Petrozza, *Advanced Functional Materials*, 2024, **34**, 2406317.

125. S. Tan, I. Yavuz, M. H. Weber, T. Huang, C.-H. Chen, R. Wang, H.-C. Wang, J. H. Ko, S. Nuryyeva, J. Xue, Y. Zhao, K.-H. Wei, J.-W. Lee and Y. Yang, *Joule*, 2020, **4**, 2426-2442.

126. S. G. Motti, D. Meggiolaro, A. J. Barker, E. Mosconi, C. A. R. Perini, J. M. Ball, M. Gandini, M. Kim, F. De Angelis and A. Petrozza, *Nature Photonics*, 2019, **13**, 532-539.

127. J. Chen, X. Wang, T. Wang, J. Li, H. Y. Chia, H. Liang, S. Xi, S. Liu, X. Guo, R. Guo, Z. Jia, X. Yin, Q. Zhou, Y. Wang, Z. Shi, H. Zhou, D. Lai, M. Zhang, Z. Xing, W. R. Leow, W. Yan and Y. Hou, *Nature Energy*, 2025, **10**, 181-190.

128. S. Akin, B. Dong, L. Pfeifer, Y. Liu, M. Graetzel and A. Hagfeldt, *Advanced Science*, 2021, **8**, 2004593.

129. C. Liu, Y. Yang, K. Rakstys, A. Mahata, M. Franckevicius, E. Mosconi, R. Skackauskaite, B. Ding, K. G. Brooks, O. J. Usiobo, J.-N. Audinot, H. Kanda, S. Driukas, G. Kavaliauskaite, V. Gulbinas, M. Dessimoz, V. Getautis, F. De Angelis, Y. Ding, S. Dai, P. J. Dyson and M. K. Nazeeruddin, *Nature Communications*, 2021, **12**, 6394.

130. C. Liu, Y. Yang, H. Chen, I. Spanopoulos, A. S. R. Bati, I. W. Gilley, J. Chen, A. Maxwell, B. Vishal, R. P. Reynolds, T. E. Wiggins, Z. Wang, C. Huang, J. Fletcher, Y. Liu, L. X. Chen, S. De Wolf, B. Chen, D. Zheng, T. J. Marks, A. Facchetti, E. H. Sargent and M. G. Kanatzidis, *Nature*, 2024, **633**, 359-364.

131. R. Lin, J. Xu, M. Wei, Y. Wang, Z. Qin, Z. Liu, J. Wu, K. Xiao, B. Chen, S. M. Park, G. Chen, H. R. Atapattu, K. R. Graham, J. Xu, J. Zhu, L. Li, C. Zhang, E. H. Sargent and H. Tan, *Nature*, 2022, **603**, 73-78.

132. S. Cacovich, G. Vidon, M. Degani, M. Legrand, L. Gouda, J.-B. Puel, Y. Vaynzof, J.-F. Guillemoles, D. Ory and G. Grancini, *Nature Communications*, 2022, **13**, 2868.

133. O. Er-raji, C. Messmer, R. R. Pradhan, O. Fischer, V. Hnapovskyi, S. Kosar, M. Marengo, M. List, J. Faisst, J. P. Jurado, O. Matiash, H. P. Pasanen, A. Prasetio, B. Vishal, S. Zhumagali, A. R. Pininti, Y. Gupta, C. Baretzky, E. Ugur, C. E. Petoukhoff, M. Bivour, E.

Aydin, R. Azmi, J. Schön, F. Schindler, M. C. Schubert, U. Schwingenschlögl, F. Laquai, A. A. Said, J. Borchert, P. S. C. Schulze, S. De Wolf and S. W. Glunz, *Science*, 2025, **390**, eadx1745.

134. X. Jiang, S. Qin, L. Meng, G. He, J. Zhang, Y. Wang, Y. Zhu, T. Zou, Y. Gong, Z. Chen, G. Sun, M. Liu, X. Li, F. Lang and Y. Li, *Nature*, 2024, **635**, 860-866.

135. S. Mariotti, E. Köhnen, F. Scheler, K. Sveinbjörnsson, L. Zimmermann, M. Piot, F. Yang, B. Li, J. Warby, A. Musiienko, D. Menzel, F. Lang, S. Keßler, I. Levine, D. Mantione, A. Al-Ashouri, M. S. Härtel, K. Xu, A. Cruz, J. Kurpiers, P. Wagner, H. Köbler, J. Li, A. Magomedov, D. Mecerreyes, E. Unger, A. Abate, M. Stolterfoht, B. Stannowski, R. Schlatmann, L. Korte and S. Albrecht, *Science*, 2023, **381**, 63-69.

136. M. Li, H. Li, Q. Zhuang, D. He, B. Liu, C. Chen, B. Zhang, T. Pauporté, Z. Zang and J. Chen, *Angewandte Chemie International Edition*, 2022, **61**, e202206914.

137. H. Meng, K. Mao, F. Cai, K. Zhang, S. Yuan, T. Li, F. Cao, Z. Su, Z. Zhu, X. Feng, W. Peng, J. Xu, Y. Gao, W. Chen, C. Xiao, X. Wu, M. D. McGehee and J. Xu, *Nature Energy*, 2024, **9**, 536-547.

138. M. Wang, Z. Shi, C. Fei, Z. J. D. Deng, G. Yang, S. P. Dunfield, D. P. Fenning and J. Huang, *Nature Energy*, 2023, **8**, 1229-1239.

139. Z. Li, X. Wang, Z. Wang, Z. Shao, L. Hao, Y. Rao, C. Chen, D. Liu, Q. Zhao, X. Sun, C. Gao, B. Zhang, X. Wang, L. Wang, G. Cui and S. Pang, *Nature Communications*, 2022, **13**, 4417.

140. A. A. Sutanto, N. Drigo, V. I. E. Queloz, I. Garcia-Benito, A. R. Kirmani, L. J. Richter, P. A. Schouwink, K. T. Cho, S. Paek, M. K. Nazeeruddin and G. Grancini, *Journal of Materials Chemistry A*, 2020, **8**, 2343-2348.

141. X. Sun, L. Y. Ji, W. W. Chen, X. Guo, H. H. Wang, M. Lei, Q. Wang and Y. F. Li, *Journal of Materials Chemistry A*, 2017, **5**, 20720-20728.

142. J. Xu, A. Buin, A. H. Ip, W. Li, O. Voznyy, R. Comin, M. Yuan, S. Jeon, Z. Ning, J. J. McDowell, P. Kanjanaboos, J.-P. Sun, X. Lan, L. N. Quan, D. H. Kim, I. G. Hill, P. Maksymovych and E. H. Sargent, *Nature Communications*, 2015, **6**, 7081.

143. Y. Kato, L. K. Ono, M. V. Lee, S. Wang, S. R. Raga and Y. Qi, *Advanced Materials Interfaces*, 2015, **2**, 1500195.

144. Natalia N. Shlenskaya, N. A. Belich, M. Grätzel, E. A. Goodilin and A. B. Tarasov, *Journal of Materials Chemistry A*, 2018, **6**, 1780-1786.

145. Y. Zhou, S. C. W. van Laar, D. Meggiolaro, L. Gregori, S. Martani, J.-Y. Heng, K. Datta, J. Jiménez-López, F. Wang, E. L. Wong, I. Poli, A. Treglia, D. Cortecchia, M. Prato, L. Kobera, F. Gao, N. Zhao, R. A. J. Janssen, F. De Angelis and A. Petrozza, *Advanced Materials*, 2024, **36**, 2305567.

146. C. C. Boyd, R. C. Shallcross, T. Moot, R. Kerner, L. Bertoluzzi, A. Onno, S. Kavadiya, C. Chosy, E. J. Wolf, J. Werner, J. A. Raiford, C. de Paula, A. F. Palmstrom, Z. J. Yu, J. J. Berry, S. F. Bent, Z. C. Holman, J. M. Luther, E. L. Ratcliff, N. R. Armstrong and M. D. McGehee, *Joule*, 2020, **4**, 1759-1775.

147. D. Wang, Z. Liu, Y. Qiao, Z. Jiang, P. Zhu, J. Zeng, W. Peng, Q. Lian, G. Qu, Y. Xu, Y. Zhang, F. Li, L. Yan, X. Wang, Y.-G. Wang, A. K. Y. Jen and B. Xu, *Joule*, 2025, **9**, 101815.

148. Y. Xiao, X. Yang, R. Zhu and H. J. Snaith, *Science*, 2024, **384**, 846-848.

149. M. Vasilopoulou, A. Fakharuddin, A. G. Coutsolelos, P. Falaras, P. Argitis, A. R. b. M. Yusoff and M. K. Nazeeruddin, *Chemical Society Reviews*, 2020, **49**, 4496-4526.

150. D. Luo, X. Li, A. Dumont, H. Yu and Z.-H. Lu, *Advanced Materials*, 2021, **33**, 2006004.

151. H. Lu, A. Krishna, S. M. Zakeeruddin, M. Grätzel and A. Hagfeldt, *iScience*, 2020, **23**, 101359.

152. Z. Ni, C. Bao, Y. Liu, Q. Jiang, W.-Q. Wu, S. Chen, X. Dai, B. Chen, B. Hartweg, Z. Yu, Z. Holman and J. Huang, *Science*, 2020, **367**, 1352-1358.

153. J. Xue, R. Wang and Y. Yang, *Nature Reviews Materials*, 2020, **5**, 809-827.

154. S. G. Motti, D. Meggiolaro, S. Martani, R. Sorrentino, A. J. Barker, F. De Angelis and A. Petrozza, *Advanced Materials*, 2019, **31**, 1901183.

155. Y. Zhou, I. Poli, D. Meggiolaro, F. De Angelis and A. Petrozza, *Nature Reviews Materials*, 2021, **6**, 986-1002.

156. Z. Ni, H. Jiao, C. Fei, H. Gu, S. Xu, Z. Yu, G. Yang, Y. Deng, Q. Jiang, Y. Liu, Y. Yan and J. Huang, *Nature Energy*, 2022, **7**, 65-73.

157. C. Fei, A. Kuvayskaya, X. Shi, M. Wang, Z. Shi, H. Jiao, T. J. Silverman, M. Owen-Bellini, Y. Dong, Y. Xian, R. Scheidt, X. Wang, G. Yang, H. Gu, N. Li, C. J. Dolan, Z. J. D. Deng, D. N. Cakan, D. P. Fenning, Y. Yan, M. C. Beard, L. T. Schelhas, A. Sellinger and J. Huang, *Science*, 2024, **384**, 1126-1134.

158. F. M. Rombach, A. Dasgupta, M. Kober-Czerny, H. Jin, J. M. Ball, J. A. Smith, M. D. Farrar and H. J. Snaith, *Nature Communications*, 2025, **16**, 5450.
159. S. Chen, X. Xiao, B. Chen, L. L. Kelly, J. Zhao, Y. Lin, M. F. Toney and J. Huang, *Science Advances*, 2021, **7**, eabb2412.
160. M. Wang, C. Fei, M. A. Uddin and J. Huang, *Science Advances*, 2022, **8**, eabo5977.
161. X. Yang, D. Luo, Y. Xiang, L. Zhao, M. Anaya, Y. Shen, J. Wu, W. Yang, Y.-H. Chiang, Y. Tu, R. Su, Q. Hu, H. Yu, G. Shao, W. Huang, T. P. Russell, Q. Gong, S. D. Stranks, W. Zhang and R. Zhu, *Advanced Materials*, 2021, **33**, 2006435.
162. T. Xiao, M. Hao, T. Duan, Y. Li, Y. Zhang, P. Guo and Y. Zhou, *Nature Energy*, 2024, **9**, 999-1010.
163. R. Fan, Q. Song, Z. Huang, Y. Ma, M. Xiao, X. Huang, H. Zai, J. Kang, H. Xie, Y. Gao, L. Wang, Y. Zhang, L. Wang, F. Wang, X. Zhang, W. Zhou, N. Li, X. Wang, Y. Bai, G. Liu, Q. Chen, L. Wang and H. Zhou, *Angewandte Chemie International Edition*, 2023, **62**, e202303176.
164. M. Hao, T. Duan, Z. Ma, M.-G. Ju, J. A. Bennett, T. Liu, P. Guo and Y. Zhou, *Advanced Materials*, 2023, **35**, 2211155.
165. Y. Lin, Y. Liu, S. Chen, S. Wang, Z. Ni, C. H. Van Brackle, S. Yang, J. Zhao, Z. Yu, X. Dai, Q. Wang, Y. Deng and J. Huang, *Energy & Environmental Science*, 2021, **14**, 1563-1572.
166. J. Warby, F. Zu, S. Zeiske, E. Gutierrez-Partida, L. Frohloff, S. Kahmann, K. Frohna, E. Mosconi, E. Radicchi, F. Lang, S. Shah, F. Peña-Camargo, H. Hempel, T. Unold, N. Koch, A. Armin, F. De Angelis, S. D. Stranks, D. Neher and M. Stolterfoht, *Advanced Energy Materials*, 2022, **12**, 2103567.
167. Z. Wang, Q. Tian, H. Zhang, H. Xie, Y. Du, L. Liu, X. Feng, A. Najar, X. Ren and S. Liu, *Angewandte Chemie International Edition*, 2023, **62**, e202305815.
168. I. Levine, P. K. Nayak, J. T.-W. Wang, N. Sakai, S. Van Reenen, T. M. Brenner, S. Mukhopadhyay, H. J. Snaith, G. Hodes and D. Cahen, *The Journal of Physical Chemistry C*, 2016, **120**, 16399-16411.
169. Y. Zhou, E. L. Wong, W. Mróz, G. Folpini, S. Martani, J. Jiménez-López, A. Treglia and A. Petrozza, *ACS Energy Letters*, 2024, **9**, 1666-1673.
170. J. Wen, Y. Zhao, P. Wu, Y. Liu, X. Zheng, R. Lin, S. Wan, K. Li, H. Luo, Y. Tian, L. Li and H. Tan, *Nature Communications*, 2023, **14**, 7118.
171. I. Metcalf, S. Sidhik, H. Zhang, A. Agrawal, J. Persaud, J. Hou, J. Even and A. D. Mohite, *Chemical Reviews*, 2023, **123**, 9565-9652.
172. G. Wu, R. Liang, M. Ge, G. Sun, Y. Zhang and G. Xing, *Advanced Materials*, 2022, **34**, 2105635.
173. G. Szabó and P. V. Kamat, *ACS Energy Letters*, 2024, **9**, 193-200.
174. L. Luo, H. Zeng, Z. Wang, M. Li, S. You, B. Chen, A. Maxwell, Q. An, L. Cui, D. Luo, J. Hu, S. Li, X. Cai, W. Li, L. Li, R. Guo, R. Huang, W. Liang, Z.-H. Lu, L. Mai, Y. Rong, E. H. Sargent and X. Li, *Nature Energy*, 2023, **8**, 294-303.
175. S. Sidhik, Y. Wang, M. De Siena, R. Asadpour, A. J. Torma, T. Terlier, K. Ho, W. Li, A. B. Puthirath, X. Shuai, A. Agrawal, B. Traore, M. Jones, R. Giridharagopal, P. M. Ajayan, J. Strzalka, D. S. Ginger, C. Katan, M. A. Alam, J. Even, M. G. Kanatzidis and A. D. Mohite, *Science*, 2022, **377**, 1425-1430.
176. C. A. R. Perini, E. Rojas-Gatjens, M. Ravello, A.-F. Castro-Mendez, J. Hidalgo, Y. An, S. Kim, B. Lai, R. Li, C. Silva-Acuña and J.-P. Correa-Baena, *Advanced Materials*, 2022, **34**, 2204726.
177. D.-J. Xue, Y. Hou, S.-C. Liu, M. Wei, B. Chen, Z. Huang, Z. Li, B. Sun, A. H. Proppe, Y. Dong, M. I. Saidaminov, S. O. Kelley, J.-S. Hu and E. H. Sargent, *Nature Communications*, 2020, **11**, 1514.
178. X. Zheng, C. Wu, S. K. Jha, Z. Li, K. Zhu and S. Priya, *ACS Energy Letters*, 2016, **1**, 1014-1020.
179. D. Liu, D. Luo, A. N. Iqbal, K. W. P. Orr, T. A. S. Doherty, Z.-H. Lu, S. D. Stranks and W. Zhang, *Nature Materials*, 2021, **20**, 1337-1346.
180. B. Fan, J. Xiong, Y. Zhang, C. Gong, F. Li, X. Meng, X. Hu, Z. Yuan, F. Wang and Y. Chen, *Advanced Materials*, 2022, **34**, 2201840.
181. H. Bristow, X. Li, M. Babics, S. Kosar, A. R. Pininti, S. Zhang, B. Vishal, S. Sarwade, A. Razzaq, A. A. Said, G. Lubineau and S. De Wolf, *Solar RRL*, 2024, **8**, 2400289.
182. M. De Bastiani, G. Armaroli, R. Jalmood, L. Ferlauto, X. Li, R. Tao, G. T. Harrison, M. K. Eswaran, R. Azmi, M. Babics, A. S. Subbiah, E. Aydin, T. G. Allen, C. Combe, T. Cramer, D. Baran, U. Schwingenschlögl, G. Lubineau, D. Cavalcoli and S. De Wolf, *ACS Energy Letters*, 2022, **7**, 827-833.
183. W.-Q. Wu, P. N. Rudd, Z. Ni, C. H. Van Brackle, H. Wei, Q. Wang, B. R. Ecker, Y. Gao and J. Huang, *Journal of the American Chemical Society*, 2020, **142**, 3989-3996.

184. S. Wu, Y. Yan, J. Yin, K. Jiang, F. Li, Z. Zeng, S.-W. Tsang and A. K. Y. Jen, *Nature Energy*, 2024, **9**, 411-421.
185. X. Lu, S. Zhou, K. Sun, Y. Meng, M. Yang, J. Zhang, R. Tian, J. Wang, H. Pan, Y. Bai, Y. Wang, Z. Song, B. Han, X. Liu, C. Xiao, C. Liu, J. Zhang and Z. Ge, *ACS Nano*, 2025, **19**, 20892-20904.
186. J. Liang, X. Hu, C. Wang, C. Liang, C. Chen, M. Xiao, J. Li, C. Tao, G. Xing, R. Yu, W. Ke and G. Fang, *Joule*, 2022, **6**, 816-833.
187. X. Chen, Q. Wang, H. Wei, J. Yang, Y. Yao, W. Tang, W. Qiu, X. Xu, L. Song, Y. Wu and Q. Peng, *Energy & Environmental Science*, 2024, **17**, 7342-7354.
188. M. Cheng, Y. Duan, D. Zhang, Z. Xie, H. Li, Q. Cao, Z. Qiu, Y. Chen and Q. Peng, *Advanced Materials*, 2025, **37**, 2419413.
189. H. Huang, Y. Guo, W. Wang, Y. Wang, Z. Feng, J. Xu, H. Zhang, Y. Ji, L. Li, X. Wu, Y. Liu, Y. Peng, X. Li, Y. Fang, Y. Zhang, C. Huang, S. Chen, W. Zhou, D. Tang, J. Sun, Y. Li, B. Ding, J. Z. Liu, K. Weber, X. He, Y. Cui, N. Hu, H. Zhan, X. Zhang and J. Peng, *Advanced Materials*, 2025, **37**, 2507918.
190. H. Zhang, L. Pfeifer, S. M. Zakeeruddin, J. Chu and M. Grätzel, *Nature Reviews Chemistry*, 2023, **7**, 632-652.
191. H. Chen, J. Yang, Q. Cao, T. Wang, X. Pu, X. He, X. Chen and X. Li, *Nano Energy*, 2023, **117**, 108883.
192. T.-S. Su, A. Krishna, C. Zhao, J. Chu and H. Zhang, *Chemical Society Reviews*, 2025, **54**, 6448-6481.
193. G. Yang, X. Liu, L. Wang, K. Dong, B. Zhang, X. Jiang, Y. Yin, M. Wang, W. Niu, L. Zheng, S. Yu, S. Liu, S. M. Zakeeruddin, X. Guo, S. Pang, L. Sun, M. Grätzel and M. Wei, *Angewandte Chemie International Edition*, 2024, **63**, e202410454.
194. N. Liu, J. Duan, H. Li, L. Ma, B. Wang, J. Li, X. Duan, Q. Guo, J. Dou, S. Geng, Y. Liu, C. Zhang, Y. Liu, B. He, X. Yang and Q. Tang, *Advanced Energy Materials*, 2024, **14**, 2402443.
195. J. Yu, G. Xie, S. Zheng, J. Chen, C. Feng, H. Li, R. Zhou, Z. Wang, L. Liu, J. Zhao, A. Liang and Y. Chen, *ACS Nano*, 2024, **18**, 22533-22547.
196. T.-S. Su, F. T. Eickemeyer, M. A. Hope, F. Jahanbakhshi, M. Mladenović, J. Li, Z. Zhou, A. Mishra, J.-H. Yum, D. Ren, A. Krishna, O. Ouellette, T.-C. Wei, H. Zhou, H.-H. Huang, M. D. Mensi, K. Sivula, S. M. Zakeeruddin, J. V. Milić, A. Hagfeldt, U. Rothlisberger, L. Emsley, H. Zhang and M. Grätzel, *Journal of the American Chemical Society*, 2020, **142**, 19980-19991.
197. H. Zhang, F. T. Eickemeyer, Z. Zhou, M. Mladenović, F. Jahanbakhshi, L. Merten, A. Hinderhofer, M. A. Hope, O. Ouellette, A. Mishra, P. Ahlawat, D. Ren, T.-S. Su, A. Krishna, Z. Wang, Z. Dong, J. Guo, S. M. Zakeeruddin, F. Schreiber, A. Hagfeldt, L. Emsley, U. Rothlisberger, J. V. Milić and M. Grätzel, *Nature Communications*, 2021, **12**, 3383.
198. G. Liu, G. Yang, W. Feng, H. Li, M. Yang, Y. Zhong, X. Jiang and W.-Q. Wu, *Advanced Materials*, 2024, **36**, 2405860.
199. Z. Fang, L. Wang, X. Mu, B. Chen, Q. Xiong, W. D. Wang, J. Ding, P. Gao, Y. Wu and J. Cao, *Journal of the American Chemical Society*, 2021, **143**, 18989-18996.
200. X. Mu, Y. Liu, G.-B. Xiao, C. Xu, X. Gao and J. Cao, *Angewandte Chemie International Edition*, 2023, **62**, e202307152.
201. D. Li, J. He, G. Zhu, Z. Zhang, J. He, M. Li, F. Zhang and Y. Geng, *ACS Applied Materials & Interfaces*, 2024, **16**, 50990-50999.
202. X. Jiang., L. Zhu, B. Zhang, G. Yang, L. Zheng, K. Dong, Y. Yin, M. Wang, S. Liu, S. Pang and X. Guo, *Angewandte Chemie International Edition*, 2025, **64**, e202420369.
203. X. Zhu, W. Xiong, C. Hu, K. Mo, M. Yang, Y. Li, R. Li, C. Shen, Y. Liu, X. Liu, S. Wang, Q. Lin, S. Yuan, Z. Liu and Z. Wang, *Advanced Materials*, 2024, **36**, 2309487.
204. S. Fu, J. Le, X. Guo, N. Sun, W. Zhang, W. Song and J. Fang, *Advanced Materials*, 2022, **34**, 2205066.
205. Z. Peng, J. Tian, K. Zhang, A. These, Z. Xie, Y. Zhao, A. Osvet, F. Guo, L. Lüer, N. Li and C. J. Brabec, *ACS Energy Letters*, 2023, **8**, 2077-2085.
206. S. Chen, Y. Liu, X. Xiao, Z. Yu, Y. Deng, X. Dai, Z. Ni and J. Huang, *Joule*, 2020, **4**, 2661-2674.
207. Z. Fang, B. Deng, Y. Jin, L. Yang, L. Chen, Y. Zhong, H. Feng, Y. Yin, K. Liu, Y. Li, J. Zhang, J. Huang, Q. Zeng, H. Wang, X. Yang, J. Yang, C. Tian, L. Xie, Z. Wei and X. Xu, *Nature Communications*, 2024, **15**, 10554.
208. J. Zhou, M. Hao, Y. Zhang, X. Ma, J. Dong, F. Lu, J. Wang, N. Wang and Y. Zhou, *Matter*, 2022, **5**, 683-693.
209. H. Li, B. Chang, L. Wang, Z. Wang, L. Pan, Y. Wu, Z. Liu and L. Yin, *ACS Energy Letters*, 2022, **7**, 3889-3899.
210. Y. Pan, J. Wang, Z. Sun, J. Zhang, Z. Zhou, C. Shi, S. Liu, F. Ren, R. Chen, Y. Cai, H. Sun, B. Liu, Z. Zhang, Z. Zhao, Z. Cai, X. Qin, Z. Zhao, Y. Ji, N. Li, W. Huang, Z. Liu and W. Chen, *Nature Communications*, 2024, **15**, 7335.
211. X. Li, W. Zhang, X. Guo, C. Lu, J. Wei and J. Fang, *Science*, 2022, **375**, 434-437.
212. S. Yang, S. Chen, E. Mosconi, Y. Fang, X. Xiao, C. Wang, Y. Zhou, Z. Yu, J. Zhao, Y. Gao, F. De Angelis and J. Huang, *Science*, 2019, **365**, 473-478.

213. Z. Zhu, K. Mao, K. Zhang, W. Peng, J. Zhang, H. Meng, S. Cheng, T. Li, H. Lin, Q. Chen, X. Wu and J. Xu, *Joule*, 2022, **6**, 2849-2868.
214. J. Chen, S. Yang, L. Jiang, K. Fan, Z. Liu, W. Liu, W. Li, H. Huang, H. Zhang and K. Yao, *Angewandte Chemie International Edition*, 2024, **63**, e202407151.
215. X. Li, Z. Ying, L. Liu, J. Wu, H. Ma, Z. He, Y. Yu, Y. Sun, M. Zhang, X. Guo, Y. Zeng, X. Yang and J. Ye, *Nature Communications*, 2025, **16**, 8692.
216. Z. Li, B. Li, X. Wu, S. A. Sheppard, S. Zhang, D. Gao, N. J. Long and Z. Zhu, *Science*, 2022, **376**, 416-420.
217. F. Wang, T. Wang, C. Ge, Y. Sun, X. Sun, X. Liang, D. Duan, Q. Li, Y. Li, F. Zhang, G. Yang, X. Zhou, Q. Zhu, H. Lin, H. Chen, T. Wu and H. Hu, *ACS Energy Letters*, 2024, **9**, 4283-4292.
218. L. Canil, T. Cramer, B. Fraboni, D. Ricciarelli, D. Meggiolaro, A. Singh, M. Liu, M. Rusu, C. M. Wolff, N. Phung, Q. Wang, D. Neher, T. Unold, P. Vivo, A. Gagliardi, F. De Angelis and A. Abate, *Energy & Environmental Science*, 2021, **14**, 1429-1438.
219. H. Chen, A. Maxwell, C. Li, S. Teale, B. Chen, T. Zhu, E. Ugur, G. Harrison, L. Grater, J. Wang, Z. Wang, L. Zeng, S. M. Park, L. Chen, P. Serles, R. A. Awni, B. Subedi, X. Zheng, C. Xiao, N. J. Podraza, T. Filleter, C. Liu, Y. Yang, J. M. Luther, S. De Wolf, M. G. Kanatzidis, Y. Yan and E. H. Sargent, *Nature*, 2023, **613**, 676-681.
220. Z. Liang, H. Xu, Y. Zhang, G. Liu, S. Chu, Y. Tao, X. Xu, S. Xu, L. Zhang, X. Chen, B. Xu, Z. Xiao, X. Pan and J. Ye, *Advanced Materials*, 2022, **34**, 2110241.
221. J. Liu, Y. He, L. Ding, H. Zhang, Q. Li, L. Jia, J. Yu, T. W. Lau, M. Li, Y. Qin, X. Gu, F. Zhang, Q. Li, Y. Yang, S. Zhao, X. Wu, J. Liu, T. Liu, Y. Gao, Y. Wang, X. Dong, H. Chen, P. Li, T. Zhou, M. Yang, X. Ru, F. Peng, S. Yin, M. Qu, D. Zhao, Z. Zhao, M. Li, P. Guo, H. Yan, C. Xiao, P. Xiao, J. Yin, X. Zhang, Z. Li, B. He and X. Xu, *Nature*, 2024, **635**, 596-603.
222. S. Hu, K. Otsuka, R. Murdey, T. Nakamura, M. A. Truong, T. Yamada, T. Handa, K. Matsuda, K. Nakano, A. Sato, K. Marumoto, K. Tajima, Y. Kanemitsu and A. Wakamiya, *Energy & Environmental Science*, 2022, **15**, 2096-2107.
223. T. Tian, J.-X. Zhong, M. Yang, W. Feng, C. Zhang, W. Zhang, Y. Abdi, L. Wang, B.-X. Lei and W.-Q. Wu, *Angewandte Chemie International Edition*, 2021, **60**, 23735-23742.
224. Q. Li, Y. Zheng, H. Wang, X. Liu, M. Lin, X. Sui, X. Leng, D. Liu, Z. Wei, M. Song, D. Li, H. G. Yang, S. Yang and Y. Hou, *Science*, 2025, **387**, 1069-1077.
225. Y. Yang, S. Cheng, X. Zhu, S. Li, Z. Zheng, K. Zhao, L. Ji, R. Li, Y. Liu, C. Liu, Q. Lin, N. Yan and Z. Wang, *Nature Energy*, 2024, **9**, 37-46.
226. B. Li, X. Wang, T. Zhang, W. Ning, D. Zhao, Y. Wang, X. Yu and D. Yang, *Nature Photonics*, 2026, **20**, 280-286.
227. C. Li, X. Wang, E. Bi, F. Jiang, S. M. Park, Y. Li, L. Chen, Z. Wang, L. Zeng, H. Chen, Y. Liu, C. R. Grice, A. Abudulimu, J. Chung, Y. Xian, T. Zhu, H. Lai, B. Chen, R. J. Ellingson, F. Fu, D. S. Ginger, Z. Song, E. H. Sargent and Y. Yan, *Science*, 2023, **379**, 690-694.
228. X. Leng, Y. Zheng, J. He, B. Shen, H. Wang, Q. Li, X. Liu, M. Lin, Y. Shi, Z. Wei, Y. Peng, H. G. Yang, Q. Niu, S. Yang and Y. Hou, *Energy & Environmental Science*, 2024, **17**, 4295-4303.
229. X. Zhao, R. Luo, C. Yu, X. Xu, W. Zhu, Y. Min and N. Cai, *Advanced Functional Materials*, 2024, **34**, 2307568.
230. G. Zhou, C. Ding, X. Luo, L. Zhang, Z. Wang, B. Xu and C.-Q. Ma, *Advanced Energy and Sustainability Research*, 2025, **6**, 2500027.
231. Z. Huang, A. H. Proppe, H. Tan, M. I. Saidaminov, F. Tan, A. Mei, C.-S. Tan, M. Wei, Y. Hou, H. Han, S. O. Kelley and E. H. Sargent, *ACS Energy Letters*, 2019, **4**, 1521-1527.
232. H. Gu, J. Xia, C. Liang, Y. Chen, W. Huang and G. Xing, *Nature Reviews Materials*, 2023, **8**, 533-551.
233. B. Li, Q. Liu, J. Gong, S. Li, C. Zhang, D. Gao, Z. Chen, Z. Li, X. Wu, D. Zhao, Z. Yu, X. Li, Y. Wang, H. Lu, X. C. Zeng and Z. Zhu, *Nature Communications*, 2024, **15**, 2753.
234. A. Zhang, M. Li, C. Dong, W. Ye, X. Yang, A. Shaker, M. S. Salem, Z. Li, J. Yang, X. Li, L. Xu, H. Song, C. Chen and J. Tang, *Small*, 2024, **20**, 2401197.
235. T. Wang, L. Bi, L. Yang, Z. Zeng, X. Ji, Z. Hu, S.-W. Tsang, H.-L. Yip, Q. Fu, A. K. Y. Jen and Y. Liu, *Journal of the American Chemical Society*, 2024, **146**, 7555-7564.
236. D. Yu, Q. Wei, H. Li, J. Xie, X. Jiang, T. Pan, H. Wang, M. Pan, W. Zhou, W. Liu, P. C. Y. Chow and Z. Ning, *Angewandte Chemie International Edition*, 2022, **61**, e202202346.
237. Z. Shi, S. Liu, R. Luo, J. Ma, H. Tian, X. Wang, Z. Dong, X. Guo, J. Chen, J. Feng, C. Xiao, Y. Wu, W. Hu and Y. Hou, *Journal of the American Chemical Society*, 2025, **147**, 1055-1062.

238. Y. Tian, X. Zhang, K. Zhao, X. Miao, T. Deng, W. Fan, D. Jin, X. Jiang, S. Zhong, X. Wang, S. Wang, P. Shi, L. Tian, L. Yao, S. Gong, X. Yu, X. Gao, Z. Chen, X. Chen, Y. Lu, V. Shrote, Y. Yang, D. Yang, R. Wang and J. Xue, *Nature Photonics*, 2024, **18**, 960-966.

239. S. Ramakrishnan, D. Song, Y. Xu, X. Zhang, G. Aksoy, M. Cotlet, M. Li, Y. Zhang and Q. Yu, *Advanced Energy Materials*, 2023, **13**, 2302240.

240. X. Chang, R. Azmi, T. Yang, N. Wu, S. Y. Jeong, H. Xi, D. Satrio Utomo, B. Vishal, F. H. Isikgor, H. Faber, Z. Ling, M. He, M. Marengo, P. Dally, A. Prasetio, Y.-Y. Yang, C. Xiao, H. Y. Woo, K. Zhao, M. Heeney, S. De Wolf, L. Tsetseris and T. D. Anthopoulos, *Nature Communications*, 2025, **16**, 1042.

241. G. Lv, L. Li, D. Lu, Z. Xu, Y. Dong, Q. Li, Z. Chang, W.-J. Yin and Y. Liu, *Nano Letters*, 2021, **21**, 5788-5797.

242. H. Ren, S. Yu, L. Chao, Y. Xia, Y. Sun, S. Zuo, F. Li, T. Niu, Y. Yang, H. Ju, B. Li, H. Du, X. Gao, J. Zhang, J. Wang, L. Zhang, Y. Chen and W. Huang, *Nature Photonics*, 2020, **14**, 154-163.

243. Z. Li, P. Guo, Y. Zhang, W. Wang, S. Cai and Y. Zhou, *Nature Synthesis*, 2025, **4**, 1078-1087.

244. Z. Liu, B. Chang, S. Ma, C. Li, Y. Wu, X. Tong, C. Yu, Y. Chen and L. Yin, *Advanced Materials*, 2026, **38**, e12874.

245. L. Zhao, J. Zhang, Y. Hua, X. Song, C. Wu, R. Chen, Y. Feng, H. Deng, J. Su, L. Gu, W. Hui, W. Chen, C. Yang and L. Song, *Energy & Environmental Science*, 2026, **19**, 1365-1373.

246. X. Zang, S. Xiong, S. Jiang, D. Li, H. Wu, H. Ren, A. Cao, B. Li, Z. Ma, J. Chen, L. Ding, J. Tang, Z. Sun, J. Chu and Q. Bao, *Advanced Materials*, 2024, **36**, 2309991.

247. E. Choi, J.-W. Lee, M. Anaya, A. Mirabelli, H. Shim, J. Strzalka, J. Lim, S. Yun, M. Dubajic, J. Lim, J. Seidel, R. E. Agbenyeke, C. G. Kim, N. J. Jeon, A. M. Soufiani, H. H. Park and J. S. Yun, *Advanced Energy Materials*, 2023, **13**, 2301717.

248. Y. Ma, F. Li, J. Gong, L. Wang, X. Tang, P. Zeng, P. F. Chan, W. Zhu, C. Zhang and M. Liu, *Energy & Environmental Science*, 2024, **17**, 1570-1579.

249. L. Shen, P. Song, L. Zheng, L. Wang, X. Zhang, K. Liu, Y. Liang, W. Tian, Y. Luo, J. Qiu, C. Tian, L. Xie and Z. Wei, *Advanced Materials*, 2023, **35**, 2301624.

250. Y. Luo, K. Liu, L. Yang, W. Feng, L. Zheng, L. Shen, Y. Jin, Z. Fang, P. Song, W. Tian, P. Xu, Y. Li, C. Tian, L. Xie and Z. Wei, *Nature Communications*, 2023, **14**, 3738.

251. Z. Shi, R. Guo, R. Luo, X. Wang, J. Ma, J. Feng, X. Niu, E. Alvianto, Z. Jia, X. Guo, H. Liang, J. Chen, Z. Li, K. Sun, X. Jiang, Y. Wu, P. Müller-Buschbaum, W. Hu and Y. Hou, *ACS Energy Letters*, 2024, **9**, 419-427.

252. T. Huang, F. Xu, J. Hu, J. Wu, S. Li, P. Chen, X. Jia, Q. Li, H. Yan, Y. Ji, D. Luo, D. Wang, J. Hu, H.-H. Chen, Z. Lu, H. Xu, L. Li, R. Sha, Q. Zhong, X. Bai, M. I. Dar, T. Song, Z. Li, X. Yang, L. Zhao, Z.-H. Lu, Q. Gong and R. Zhu, *Energy & Environmental Science*, 2024, **17**, 5984-5992.

253. J. Li, L. Zuo, H. Wu, B. Niu, S. Shan, G. Wu and H. Chen, *Advanced Functional Materials*, 2021, **31**, 2104036.

254. H. Li, C. Zhang, C. Gong, D. Zhang, H. Zhang, Q. Zhuang, X. Yu, S. Gong, X. Chen, J. Yang, X. Li, R. Li, J. Li, J. Zhou, H. Yang, Q. Lin, J. Chu, M. Grätzel, J. Chen and Z. Zang, *Nature Energy*, 2023, **8**, 946-955.

255. F. Zhang, B. Tu, S. Yang, K. Fan, Z. Liu, Z. Xiong, J. Zhang, W. Li, H. Huang, C. Yu, A. K.-Y. Jen and K. Yao, *Advanced Materials*, 2023, **35**, 2303139.

256. S. Wang, W. Tian, Z. Cheng, X. Shi, W. Fan, J. Zhou, D. Gu, J. Xue and R. Wang, *Nature Energy*, 2025, **10**, 1074-1083.

257. G. Li, Z. Zhang, B. Agyei-Tuffour, L. Wu, T. W. Gries, K. Prashanthan, A. Musiienko, J. Li, R. Zhu, L. J. F. Hart, L. Wang, Z. Li, B. Hou, M. Saba, P. R. F. Barnes, J. Nelson, P. J. Dyson, M. K. Nazeeruddin, M. Li and A. Abate, *Nature Photonics*, 2026, **20**, 55-62.

258. M. Li, Y. Yang, S. Li, X. Yang, Y. Zheng, S. Cheng, J. Feng, H. Li, Q. Yu, Z. Xu, H. Fei, Y. Liu, C. Guo, S. Yuan, Q. Lin and Z. Wang, *Nature Energy*, 2026, 10.1038/s41560-026-02025-6.

259. A. S. Subbiah, S. Mannar, V. Hnapovskyi, A. R. Pininti, B. Vishal, L. V. Torres Merino, O. Matiash, O. Karalis, H. Hempel, A. Prasetio, B. Yildirim, P. Dally, D. Rosas Villalva, M. Babics, L. Xu, A. Razzaq, R. Azmi, F. Xu, H. L. Bristow, E. Ugur, A. Ur Rehman, H. Pasanen, E. Aydin, T. Allen, D. Baran, T. Unold, F. Laquai and S. De Wolf, *Joule*, 2025, **9**, 101767.

260. R. Li, D. Zhang, J. Wei, B. Li, H. Xin, H. Pengjie, Z. Ni, D. Yang and X. Yu, *Joule*, 2025, **10**, 102141.

261. R. Liu, C. Lan, M. Zeng, Z. Zheng, X. Zheng, R. Guo, J. Guo, S. Yang, Z. Wang and X. Li, *Advanced Materials*, 2025, **37**, 2504321.

262. Y. Zhao, T. Ma, X. Yin, L. Zhou, Y. Zhang, Z. Wu, C. Chen, Y. Liu, Z. Yang, L. Hu, Z. Li, C. Chen, H. Tian, C. Xiao, Z. Chen, B. Zou, L. Jiang, D. Zhao, X. Li and C. Wang, *Energy & Environmental Science*, 2025, **18**, 8527-8536.

263. R. Lin, H. Gao, J. Lou, J. Xu, M. Yin, P. Wu, C. Liu, Y. Guo, E. Wang, S. Yang, R. Liu, D. Zhou, C. Ding, A. Bui, N. Yin, D. H. Macdonald, C. Ma, Q. Chen, K. Xiao, X. Luo, Y. Liu, L. Li, Y. Li, C. Chang and H. Tan, *Nature*, 2025, **648**, 600-606.
264. X. Yu, X. Sun, Z. Zhu and Z. a. Li, *Angewandte Chemie*, 2025, **137**, e202419608.
265. J. Wang, H. Shi, N. Xu, J. Zhang, Y. Yuan, M. Lei, L. Wang and P. Wang, *Advanced Functional Materials*, 2020, **30**, 2002114.
266. W. Jiang, F. Li, M. Li, F. Qi, F. R. Lin and A. K.-Y. Jen, *Angewandte Chemie International Edition*, 2022, **61**, e202213560.
267. R. He, W. Wang, Z. Yi, F. Lang, C. Chen, J. Luo, J. Zhu, J. Thiesbrummel, S. Shah, K. Wei, Y. Luo, C. Wang, H. Lai, H. Huang, J. Zhou, B. Zou, X. Yin, S. Ren, X. Hao, L. Wu, J. Zhang, J. Zhang, M. Stolterfoht, F. Fu, W. Tang and D. Zhao, *Nature*, 2023, **618**, 80-86.
268. S. Zhang, R. Wu, C. Mu, Y. Wang, L. Han, Y. Wu and W.-H. Zhu, *ACS Materials Letters*, 2022, **4**, 1976-1983.
269. G. Qu, S. Cai, Y. Qiao, D. Wang, S. Gong, D. Khan, Y. Wang, K. Jiang, Q. Chen, L. Zhang, Y.-G. Wang, X. Chen, A. K. Y. Jen and Z.-X. Xu, *Joule*, 2024, **8**, 2123-2134.
270. S. Zhang, X. Wang, Y. Wu, X. Li, T. Hou, D. Li, W. Chen, J. Li, R. Lv, Y. Zhang, Z. Xiao, T. Chen, S. Chen, Z. Fang, S. Liu and S. Yang, *Angewandte Chemie International Edition*, 2025, **64**, e202508782.
271. Z. X. Chen, Y. Li and F. Huang, *Chem*, 2021, **7**, 288-332.
272. Z. Chen, W. Li, M. A. Sabuj, Y. Li, W. Zhu, M. Zeng, C. S. Sarap, M. M. Huda, X. Qiao, X. Peng, D. Ma, Y. Ma, N. Rai and F. Huang, *Nature Communications*, 2021, **12**, 5889.
273. W. Wu, H. Gao, L. Jia, Y. Li, D. Zhang, H. Zhan, J. Xu, B. Li, Z. Geng, Y. Cheng, H. Tong, Y. Pan, J. Liu, Y. He, X. Xu, Z. Li, B. He, M. Zhou, L. Wang and C. Qin, *Science*, 2025, **389**, 195-199.
274. M. Liu, M. Li, Y. Li, Y. An, Z. Yao, B. Fan, F. Qi, K. Liu, H.-L. Yip, F. R. Lin and A. K.-Y. Jen, *Advanced Energy Materials*, 2024, **14**, 2303742.
275. S. Yao, Q. Su, S. Sui, F. Du, W. Yan, P. Cao, C. Liang, Z. Pan, C. Yin, J. Dong, J. Cao, W. Huang and T. Qin, *Angewandte Chemie International Edition*, 2026, **n/a**, e5319815.
276. in *Physics of Semiconductor Devices*, 2006, pp. 5-75.
277. S. M. Park, M. Wei, N. Lempesis, W. Yu, T. Hossain, L. Agosta, V. Carnevali, H. R. Atapattu, P. Serles, F. T. Eickemeyer, H. Shin, M. Vafaie, D. Choi, K. Darabi, E. D. Jung, Y. Yang, D. B. Kim, S. M. Zakeeruddin, B. Chen, A. Amassian, T. Filleter, M. G. Kanatzidis, K. R. Graham, L. Xiao, U. Rothlisberger, M. Grätzel and E. H. Sargent, *Nature*, 2023, **624**, 289-294.
278. S. Yuan, C. Ge, T. Zhang, G. Su, Q. Qiu, G. Ren, L. Ke, G. Du, G. Zou, N. Zhang, H. Liu, Q. Li, T. Jia, Y.-P. Cai, S. Liu and H.-L. Yip, *Journal of the American Chemical Society*, 2025, **147**, 24662-24671.
279. D. Wang, Z. Liu, Y. Qiao, Z. Jiang, P. Zhu, J. Zeng, W. Peng, Q. Lian, G. Qu, Y. Xu, Y. Zhang, F. Li, L. Yan, X. Wang, Y.-G. Wang, A. K. Y. Jen and B. Xu, *Joule*, 2025, **9**, 101815.
280. M. A. Truong, T. Funasaki, L. Ueberricke, W. Nojo, R. Murdey, T. Yamada, S. Hu, A. Akatsuka, N. Sekiguchi, S. Hira, L. Xie, T. Nakamura, N. Shioya, D. Kan, Y. Tsuji, S. Iikubo, H. Yoshida, Y. Shimakawa, T. Hasegawa, Y. Kanemitsu, T. Suzuki and A. Wakamiya, *Journal of the American Chemical Society*, 2023, **145**, 7528-7539.
281. L. Jia, S. Xia, J. Li, Y. Qin, B. Pei, L. Ding, J. Yin, T. Du, Z. Fang, Y. Yin, J. Liu, Y. Yang, F. Zhang, X. Wu, Q. Li, S. Zhao, H. Zhang, Q. Li, Q. Jia, C. Liu, X. Gu, B. Liu, X. Dong, J. Liu, T. Liu, Y. Gao, M. Yang, S. Yin, X. Ru, H. Chen, B. Yang, Z. Zheng, W. Zhou, M. Dou, S. Wang, S. Gao, L. Chen, M. Qu, J. Lu, L. Fang, Y. Wang, H. Deng, J. Yu, X. Zhang, M. Li, X. Lang, C. Xiao, Q. Hu, C. Xue, L. Ning, Y. He, Z. Li, X. Xu and B. He, *Nature*, 2025, **644**, 912-919.
282. C. Luo, Q. Zhou, K. Wang, X. Wang, J. He, P. Gao, C. Zhan, Z. Bi, W. Li, Y. Ma, W. Chen, Y. Hou, Z. Liu and Q. Zhao, *Nature Materials*, 2025, **24**, 1265-1272.
283. H. Tang, Z. Shen, Y. Shen, G. Yan, Y. Wang, Q. Han and L. Han, *Science*, 2024, **383**, 1236-1240.
284. Z. Lv, G. Liu, Z. Wang, Y. Gao, M. Xu, L. Yang, Z. Tian, Y. Zhang, G. Zhou, B. Xu, Z. Liu, G. Dai, W. Lu, P. Wang, J. Wei, Q. Dong, J. Bian and Y. Shi, *Energy & Environmental Science*, 2026, 10.1039/D6EE00740F.
285. A. Al-Ashouri, M. Marčinskas, E. Kasparavičius, T. Malinauskas, A. Palmstrom, V. Getautis, S. Albrecht, M. D. McGehee and A. Magomedov, *ACS Energy Letters*, 2023, **8**, 898-900.
286. S. Zhang, F. Ye, X. Wang, R. Chen, H. Zhang, L. Zhan, X. Jiang, Y. Li, X. Ji, S. Liu, M. Yu, F. Yu, Y. Zhang, R. Wu, Z. Liu, Z. Ning, D. Neher, L. Han, Y. Lin, H. Tian, W. Chen, M. Stolterfoht, L. Zhang, W.-H. Zhu and Y. Wu, *Science*, 2023, **380**, 404-409.

287. G. Qu, L. Zhang, Y. Qiao, S. Gong, Y. Ding, Y. Tao, S. Cai, X.-Y. Chang, Q. Chen, P. Xie, J. Feng, C. Gao, G. Li, H. Xiao, F. Wang, H. Hu, J. Yang, S. Chen, A. K. Y. Jen, X. Chen and Z.-X. Xu, *Nature Communications*, 2025, **16**, 86.

288. R. Guo, X. Wang, X. Jia, X. Guo, J. Li, Z. Li, K. Sun, X. Jiang, E. Alvianto, Z. Shi, M. Schwartzkopf, P. Müller-Buschbaum and Y. Hou, *Advanced Energy Materials*, 2023, **13**, 2302280.

289. A. Kulkarni, R. Sarkar, S. Akel, M. Häser, B. Klingebiel, M. Wuttig, S. Wiegand, S. Chakraborty, M. Saliba and T. Kirchartz, *Advanced Functional Materials*, 2023, **33**, 2305812.

290. B. Li, C. Zhang, D. Gao, X. Sun, S. Zhang, Z. Li, J. Gong, S. Li and Z. Zhu, *Advanced Materials*, 2024, **36**, 2309768.

291. A. Ullah, K. H. Park, H. D. Nguyen, Y. Siddique, S. F. A. Shah, H. Tran, S. Park, S. I. Lee, K.-K. Lee, C.-H. Han, K. Kim, S. Ahn, I. Jeong, Y. S. Park and S. Hong, *Advanced Energy Materials*, 2022, **12**, 2103175.

292. A. Ullah, K. H. Park, Y. Lee, S. Park, A. B. Faheem, H. D. Nguyen, Y. Siddique, K.-K. Lee, Y. Jo, C.-H. Han, S. Ahn, I. Jeong, S. Cho, B. Kim, Y. S. Park and S. Hong, *Advanced Functional Materials*, 2022, **32**, 2208793.

293. T. Liu, C. Luo, R. He, Z. Zhang, X. Lin, Y. Chen and T. Wu, *Advanced Materials*, 2026, **n/a**, 2502032.

294. S. Qu, F. Yang, H. Huang, Y. Li, C. Sun, Q. Zhang, S. Du, L. Yan, Z. Lan, Z. Wang, T. Jiang, P. Cui, X. Ai and M. Li, *Energy & Environmental Science*, 2025, **18**, 3186-3195.

295. W. Jiang, G. Qu, X. Huang, X. Chen, L. Chi, T. Wang, C.-T. Wong, F. R. Lin, C. Yang, Q. Jiang, S. Wu, J. Zhang and A. K. Y. Jen, *Nature*, 2025, **646**, 95-101.

296. B. Li, C. Zhang, D. Gao, X. Sun, S. Zhang, Z. Li, J. Gong, S. Li and Z. Zhu, *Advanced Materials*, 2024, **36**, 2309768.

297. B. Dong, M. Wei, Y. Li, Y. Yang, W. Ma, Y. Zhang, Y. Ran, M. Cui, Z. Su, Q. Fan, Z. Bi, T. Edvinsson, Z. Ding, H. Ju, S. You, S. M. Zakeeruddin, X. Li, A. Hagfeldt, M. Grätzel and Y. Liu, *Nature Energy*, 2025, **10**, 342-353.

298. S. Yin, X. Luo, F. Tang, Z. Xiong, Y. Lin, W. Yang, Y. Shu, Y. Wang and L. Ying, *Energy & Environmental Science*, 2025, **18**, 4153-4161.

299. D. Zhang, B. Yan, R. Xia, B. Li, R. Li, P. Hang, H. Xin, J. Wei, M. Lei, Y. Chen, J. Gao, H. Zhang, Z. Ni, D. Yang and X. Yu, *Nature Photonics*, 2026, **20**, 40-48.

300. B. Zhang, J. Luo, H. Yin, Q. Li, S. Sun, N. Zhang, N. Gan, M. Azam, T. W. Park, Z. Wan, C. Jia, M. Wei and S. M. Park, *Science*, 2025, **390**, 837-842.

301. J. Huang, L. Zhang, C. Yilmaz, G. Qu, I. Zemer, R. Hooijer, S. Cai, A. Buyruk, H. Zhu, M. Bouraoui, A. Hartschuh, R. Mishima, K. Yamamoto, C. Deger, I. Yavuz, A. K. Y. Jen, E. Ugur, S. De Wolf, I. Levine, Z.-X. Xu and E. Aydin, *Joule*, 2026, **10**, 102227.

302. R. Tao, G. Wang, Z. Li, N. Sun, J. Bing, T. L. Leung, F. J. Angus, J. Tang, C. Liao, J. Yi, C. Bailey, L. Liu, Y. Wang, G. Huang, A. Lambertz, S. Yin, B. Gong, A.-A. Cavallaro, D. Evans, M. Griffith, K. Kalantar-Zadeh, J. Zheng, P. Docampo, D. R. McKenzie, M. A. Mahmud, K. Ding and A. W. Y. Ho-Baillie, *Joule,* 2026, 102314.

303. Z. Wei, Q. Zhou, X. Niu, S. Liu, Z. Dong, H. Liang, J. Chen, Z. Shi, X. Wang, Z. Jia, X. Guo, R. Guo, X. Meng, Y.-D. Wang, N. Li, Z. Xu, Z. Li, A. G. Aberle, X. Yin and Y. Hou, *Energy & Environmental Science*, 2025, **18**, 1847-1855.

304. Z. Lin, J. Chen, K. Fan, J. Yi, H. Chen, S. Zou, H. Min, Y. Xu, M. Yu Lam, S. A. Aleksandr, K. S. Wong, H. Yan and K. Yan, *Angewandte Chemie International Edition*, 2025, **64**, e202424825.

305. J. Wang, B. Jiao, R. Tian, K. Sun, Y. Meng, Y. Bai, X. Lu, B. Han, M. Yang, Y. Wang, S. Zhou, H. Pan, Z. Song, C. Xiao, C. Liu and Z. Ge, *Nature Communications*, 2025, **16**, 4148.

306. S. Fu, N. Sun, S. Hu, H. Chen, X. Jiang, Y. Li, X. Zhu, X. Guo, W. Zhang, X. Li, A. S. Vasenko and J. Fang, *Energy & Environmental Science*, 2025, **18**, 5503-5510.

307. C. Shi, J. Wang, X. Lei, Q. Zhou, W. Wang, Z. Yang, S. Liu, J. Zhang, H. Zhu, R. Chen, Y. Pan, Z. Tan, W. Liu, Z. Zhao, Z. Cai, X. Qin, Z. Zhao, J. Li, Z. Liu and W. Chen, *Nature Communications*, 2025, **16**, 3029.

308. S. You, H. Zhu, Z. Shen, X. Wang, B. Shao, Q. Wang, J. Lu, Y. Yuan, B. D. Dou, E. M. Sanehira, T. Russell, A. Lorenz, Y. Dong, L. Chen, M. Casareto, N. Rolston, M. C. Beard, J. J. Berry, M. Freitag, Y. Yan, O. M. Bakr and K. Zhu, *Science*, **0**, eadv4701.

309. Y. Jiang, J. Wang, H. Zai, D. Ni, J. Wang, P. Xue, N. Li, B. Jia, H. Lu, Y. Zhang, F. Wang, Z. Guo, Z. Bi, H. Xie, Q. Wang, W. Ma, Y. Tu, H. Zhou and X. Zhan, *Journal of the American Chemical Society*, 2022, **144**, 5400-5410.

310. X. Sun, C. Zhang, D. Gao, X. Yu, B. Li, X. Wu, S. Zhang, Y. He, Z. Yu, L. Qian, J. Gong, S. Li, N. Li, Z. Zhu and Z. a. Li, *Angewandte Chemie International Edition*, 2025, **64**, e202412819.

311. Z. Xing, S. Ma, B.-W. Chen, M. An, A. Fan, X. Hu, Y. Wang, L.-L. Deng, Q. Huang, H. Kanda, F. G. Al-Amri, G. Pozzi, Y. Zhang, J. Xia, J. Wu, X. Guo and M. K. Nazeeruddin, *Joule*, 2025, **9**, 101817.

312. Y. Lin, Z. Lin, S. Lv, Y. Shui, W. Zhu, Z. Zhang, W. Yang, J. Zhao, H. Gu, J. Xia, D. Wang, F. Du, A. Zhu, J. Liu, H. Cai, B. Wang, N. Zhang, H. Wang, X. Liu, T. Liu, C. Kong, D. Zhou, S. Chen, Z. Yang, T. Li, W. Ma, G. Fang, L. Echegoyen, G. Xing, S. Yang, T. Yang, W. Cai, M. Li, W. Huang and C. Liang, *Nature*, 2025, **642**, 78-84.

313. A. Dzwilewski, T. Wågberg and L. Edman, *Journal of the American Chemical Society*, 2009, **131**, 4006-4011.

314. S. Pont, F. Foglia, A. M. Higgins, J. R. Durrant and J. T. Cabral, *Advanced Functional Materials*, 2018, **28**, 1802520.

315. Z. Liang, H. Xu, Z. Huang, X. Lei, J. Ye, Y. Zhang, P. Zhu, B. Liu, W. Chen, X. Wang, Y. Li, Y. Liao, S. Weng, Y. Tao, Y. Zhang, H. Zhang, F. Chen, J. Zeng, X. Cai, S.-U. Lee, J. Dong, W. Liu, H. Zhou, H. Lin, L. Yang, G. Xu, Y. Ding, J. Sheng, J. Li, S. Yang, B. Xu, Z. Xiao, T. Kirchartz, X. Pan and N.-G. Park, *Nature Materials*, 2026, **25**, 267-274.

316. X. Huang, D. Xia, Q. Xie, D. Wang, Q. Li, C. Zhao, J. Yin, F. Cao, Z. Su, Z. Zeng, W. Jiang, W. Kaminsky, K. Liu, F. R. Lin, Q. Feng, B. Wu, S.-W. Tsang, D. Lei, W. Li and A. K. Y. Jen, *Nature Communications*, 2025, **16**, 1626.

317. R. Sun, X. Yuan, X. Yang, Y. Wu, Y. Shao, X. Wu, C. J. Brabec and J. Min, *Joule*, 2024, **8**, 2523-2538.

318. Q. Wei, J. Yuan, Y. Yi, C. Zhang and Y. Zou, *National Science Review*, 2021, **8**, nwab121.

319. S. V. Bhosale, M. Al Kobaisi, R. W. Jadhav, P. P. Morajkar, L. A. Jones and S. George, *Chemical Society Reviews*, 2021, **50**, 9845-9998.

320. Y. Shi, W. Chen, Z. Wu, Y. Wang, W. Sun, K. Yang, Y. Tang, H. Y. Woo, M. Zhou, A. B. Djurišić, Z. He and X. Guo, *Journal of Materials Chemistry A*, 2020, **8**, 13754-13762.

321. J. Lawton, J. S. Wagner, X. Xiao, S. Kim, A. M. Österholm, D. E. Shen, S. Sabury, C. A. R. Perini, K. Datta, D. K. LaFollette, R. Li, J. R. Reynolds and J.-P. Correa-Baena, *Chemistry of Materials*, 2025, **37**, 6655-6666.

322. P. Chen, Y. Xiao, S. Li, X. Jia, D. Luo, W. Zhang, H. J. Snaith, Q. Gong and R. Zhu, *Chemical Reviews*, 2024, **124**, 10623-10700.

323. S. Wu, R. Chen, S. Zhang, B. H. Babu, Y. Yue, H. Zhu, Z. Yang, C. Chen, W. Chen, Y. Huang, S. Fang, T. Liu, L. Han and W. Chen, *Nature Communications*, 2019, **10**, 1161.

324. M. Xiao, G. Yuan, Z. Lu, J. Xia, D. Li, Y. Chen, Y. Zhang, F. Pei, C. Chen, Y. Bai, T. Song, J. Dou, Y. Li, Y. Chen, Z. Xu, X. Yang, Z. Liu, X. Liu, C. Zhu and Q. Chen, *Advanced Materials*, 2023, **35**, 2301684.

325. E. Bi, W. Tang, H. Chen, Y. Wang, J. Barbaud, T. Wu, W. Kong, P. Tu, H. Zhu, X. Zeng, J. He, S.-i. Kan, X. Yang, M. Grätzel and L. Han, *Joule*, 2019, **3**, 2748-2760.

326. N.-G. Park and K. Zhu, *Nature Reviews Materials*, 2020, **5**, 333-350.

327. K. Xiao, Y.-H. Lin, M. Zhang, R. D. J. Oliver, X. Wang, Z. Liu, X. Luo, J. Li, D. Lai, H. Luo, R. Lin, J. Xu, Y. Hou, H. J. Snaith and H. Tan, *Science*, 2022, **376**, 762-767.

328. Q. Weng, Y. Li, S. Fu, N. Sun, B. Feng, X. Zhu, T. You, W. Zhang, X. Li and J. Fang, *Advanced Materials*, 2026, **38**, e20308.

329. Z. Shen, Q. Han, X. Luo, Y. Shen, Y. Wang, Y. Yuan, Y. Zhang, Y. Yang and L. Han, *Nature Photonics*, 2024, **18**, 450-457.

330. S. Xiong, Z. Hou, S. Zou, X. Lu, J. Yang, T. Hao, Z. Zhou, J. Xu, Y. Zeng, W. Xiao, W. Dong, D. Li, X. Wang, Z. Hu, L. Sun, Y. Wu, X. Liu, L. Ding, Z. Sun, M. Fahlman and Q. Bao, *Joule*, 2021, **5**, 467-480.

331. T. J. Silverman, M. G. Deceglie, I. Repins, M. Owen-Bellini, J. J. Berry, J. S. Stein and L. T. Schelhas, *Nature Energy*, 2025, **10**, 934-940.

332. L. A. Castriotta, M. Wang, X. Shi, B. D. Dou, L. T. Schelhas and J. Huang, *Nature Energy*, 2026, 10.1038/s41560-026-01969-z.

333. Z. Liu, K. Meng, X. Wang, Z. Qiao, Q. Xu, S. Li, L. Cheng, Z. Li and G. Chen, *Nano Letters*, 2020, **20**, 1296-1304.

334. D. Lin, T. Zhang, J. Wang, M. Long, F. Xie, J. Chen, B. Wu, T. Shi, K. Yan, W. Xie, P. Liu and J. Xu, *Nano Energy*, 2019, **59**, 619-625.

335. X. Sun, W. Shi, T. Liu, J. Cheng, X. Wang, P. Xu, W. Zhang, X. Zhao and W. Guo, *Science*, 2025, **388**, 957-963.

336. K. Datta, S. Kim, R. Li, D. K. LaFollette, J. Yang, C. A. R. Perini and J.-P. Correa-Baena, *Advanced Materials*, 2024, **36**, 2404795.

337. W. Gao, J. Ding, Q. Ma, H. Zhang, J. Zhang, Z. Zhang, M. Li, Y. Wang, B. Zhang, T. Pauporté, J.-X. Tang, J. Chen and C. Chen, *Advanced Materials*, 2025, **37**, 2413304.

338. Z. Zhu, B. Ke, K. Sun, C. Jin, Z. Song, R. Jiang, J. Li, S. Kong, C. Liu, S. Bai, S. He, Z. Ge, F. Huang, Y.-B. Cheng and T. Bu, *Energy & Environmental Science*, 2025, **18**, 4120-4129.

339. J. Hu, Q. Cai, Y. Lin, Y. Xiao, L. Yang, K. Wei, C. Zhang, X. Li, Z. Liao, Q. Huang, Y. Li, Y. Yang, C. Liang and J. Zhang, *Science*, 2026, **391**, 164-170.

340. C. Luo, G. Zheng, X. Wang, F. Gao, C. Zhan, X. Gao and Q. Zhao, *Energy & Environmental Science*, 2023, **16**, 178-189.

341. X. Shen, W. T. Hui, S. Hu, F. Yang, J. Wang, J. Yao, A. Louwen, B. S. T. Tam, L. Rong, D. P. McMeekin, K. Lohmann, Q. Yuan, M. C. Naylor, M. Kober-Czerny, S. Seo, P. Holzhey, K.-A. Zaininger, M. G. Christoforo, P. Carroy, V. Barth, F. S. Y. Yeung, N. K. Noel, M. Johnston, Y.-H. Lin and H. J. Snaith, *Nature Materials*, 2026, 10.1038/s41563-026-02494-w.

342. F. U. Kosasih, E. Erdenebileg, N. Mathews, S. G. Mhaisalkar and A. Bruno, *Joule*, 2022, **6**, 2692-2734.

343. H. Li, J. Zhou, L. Tan, M. Li, C. Jiang, S. Wang, X. Zhao, Y. Liu, Y. Zhang, Y. Ye, W. Tress and C. Yi, *Science Advances*, 2022, **8**, eabo7422.

344. A. Diercks, J. Petry, T. Feeney, R. Singh, T. Zhao, H. Hu, Y. Li, U. W. Paetzold and P. Fassl, *ACS Energy Letters*, 2025, **10**, 1165-1173.

345. N. Li, X. Niu, Z. Dong, J. Hu, R. Luo, S. Yang, Q. Zhou, Z. Shi, J. Chen, X. Du, L. K. Lee, Y. Wang, X. Guo, X. Wang, C.-W. Qiu, M. Lin, R. He, X. Zhang, Y. Chen, M. Wu and Y. Hou, *Science*, 2025, **390**, eadz3698.

346. A. Paliwal, K. P. S. Zanoni, C. Roldán-Carmona, M. A. Hernández-Fenollosa and H. J. Bolink, *Matter*, 2023, **6**, 3499-3508.

View Article Online
DOI: 10.1039/D5EE07642K

Data Availability Statement

No new data was generated or analyzed in this study. All data supporting the content of this review are available in the cited literature.